

Vibration and Aeroelastic Analysis of Highly Flexible HALE Aircraft

A Thesis
Presented to
The Academic Faculty

by

Chong-Seok Chang

In Partial Fulfillment
of the Requirements for the Degree
Doctor of Philosophy

School of Aerospace Engineering
Georgia Institute of Technology
December 2006

Vibration and Aeroelastic Analysis of Highly Flexible HALE Aircraft

Approved by:

Professor Dewey H. Hodges
Daniel Guggenheim School of Aerospace
Engineering,
Georgia Institute of Technology
Committee Chair

Professor Olivier A. Bauchau
Daniel Guggenheim School of Aerospace
Engineering,
Georgia Institute of Technology

Professor Massimo Ruzzene
Daniel Guggenheim School of Aerospace
Engineering,
Georgia Institute of Technology

Professor Carlo L. Bottasso
Dipartimento di Ingegneria Aerospaziale,
Politecnico di Milano

Professor Mayuresh Patil
Aerospace and Ocean Engineering,
Virginia Tech

Date Approved: 13 November 2006

To my parents,

Youngkyu Chang and Heungja Nam,

*who have been sacrificed their every moment
to support my education and guide me to a bright future.*

“Sarang hap ni da.” (I love you.)

ACKNOWLEDGEMENTS

“At the right time ... with the right person ... ” I should say that I am really lucky because wherever I go, I meet right people who help and support me. Korean often says that I have lots of luck with people.

Let me think back on the first day that I decided to pursue Ph.D. in aerospace engineering and I would like to remember all the people who helped me and assisted me from the first day to today.

I appreciate ...

... Kilsoo Kim who helped me preparing the procedures for applying graduate schools and willingly shared the precious information with me. Finally, I could give him back what he had given to me. I was so happy to help him when he also became a new graduate student from spring 2004 at Georgia Institute of Technology.

... Prof. Keeyoung Choi who always gives me a good advice for next steps and had reminded me of one sentence through my Ph.D. “Be diligent.” I have tried to be diligent as best as I could for past four and a half years.

... Seongsik Ahn who has answered all my questions for the fundamentals through his thoughtful concepts.

... Hungsun Son who has been always willing to discuss difficulties and obstacles of my research and has led me new directions.

... Prof. Olivier A. Bauchau who has opened good courses. In his clear lectures, I could assess the fundamentals and I could have been exposed to new topics. He had also given me a joy of hard works. The answers were there, in his lecture notes and his exercises.

... Prof. Carlo L. Bottasso who firstly had given me a chance to involve a research, believing my potentials. With all his new ideas, I could have been exposed and have learned new different approaches.

... Prof. Mayuresh Patil who initiated the first version of NATASHA. His original works became a bridge between literatures and numerical implementations. So, I could have learned many new things from his works in a short time.

Finally, I really appreciate my advisor Prof. Dewey H. Hodges, who has motivated me and has guided me through my Ph.D. He always has reminded me the future difficulty about the new milestones in order for me to figure out solutions when I face it. I could have been grown in him as a Ph.D. student.

I also thank ...

my thesis committee, Profs. Dewey H. Hodges, Olivier A. Bauchau, Massimo Ruzzene, Carlo L. Bottasso, and Mayuresh Patil for their good suggestions and advices so that I could include better analysis and meaningful parametric studies in my doctoral thesis.

... my old officemates, Luca Riviello, Yalcin Faik Sumer, Julide Topsakal, and Nazmiye Acikgoz for the cheering, warming and unforgettable times that I had with them.

... my good old friends, Iksang Cho, Jonghoon Seong, Seongho Lee, Sangsoon Im, Yonghwan Park, Jeonghwan Paeng, Hyeongjin Lee for their support and encouragement from a distance.

... my seniors, Seungmin Oh, Bongjun Yang, Jouyoung Choi, and Jincheol Ha at Georgia Institute of Technology who were willing to share their knowledge with me.

... my officemate Jimmy Ho who helped me learning RCAS and had productive discussions with me. I think he saved one semester for completing my thesis.

... my family, Youngkyu Chang, Heungga Nam, Chongwook Chang and Minjeong Chang who has always supported me.

I would like to remember the memory of my old friend Wonseok Choi. I am sure that he has been my guiding angel since October, 1999 because I would have not been so lucky without his guiding.

TABLE OF CONTENTS

ACKNOWLEDGEMENTS	iv
LIST OF TABLES	viii
LIST OF FIGURES	ix
NOMENCLATURES	xii
SUMMARY	xv
I INTRODUCTION	1
1.1 Nonlinear Aeroelastic Analysis	2
1.2 Bungee System	3
1.3 Ground Vibration Test	5
1.4 Whirl Flutter Instability	6
II FOUNDATIONAL WORK	8
2.1 Structural Model	8
2.1.1 Intrinsic Beam Formulation	8
2.1.2 Finite-element Discretization	9
2.1.3 Gravity loads	11
2.1.4 Final Structural equations	12
2.2 Aerodynamic Model	13
2.3 Post-processing	16
III ANALYSIS	18
3.1 Multiple Beam Formulation	18
3.1.1 Structural Analysis	18
3.1.2 Fuselage Aerodynamics	19
3.2 Modeling of Ground Vibration Testing	20
3.2.1 Bungee Formulation	21
3.2.2 Coupling of Bungee and Intrinsic Beam Formulations	29
3.2.3 GVT in Multiple Beam Configuration	35
3.3 Engine/Propeller Modeling	36
3.3.1 Structural Modeling	37

3.3.2	Propeller Aerodynamics	41
IV	PARAMETRIC STUDY	44
4.1	Payload Distribution	45
4.2	Horizontal Tail's Contribution	50
4.3	Modal Characteristics of Stiff and Flexible Beams	53
4.4	Modal Characteristics of a Highly Flexible Beam for Different Bungee Cord Locations	68
4.5	Modal Characteristics of Flying Wing and Conventional Configurations . .	73
4.6	Time Simulation of NATASHA _{WF}	83
4.7	Periodic Inertia Effect	88
4.8	Periodic Propeller Airloads	92
4.9	Validations	98
4.9.1	Validations 1: Euler-Bernoulli Beam Theory	98
4.9.2	Validations 2: RCAS	98
V	CONCLUSION	103
APPENDIX A	— IDEAL MODELS	107
APPENDIX B	— PRELIMINARY ENG/PROP MODELING	109
REFERENCES	114
VITA	119

LIST OF TABLES

Table 1	Parameters in “Payload Distribution”	46
Table 2	Three lowest eigenvalues of each case in “Payload Distribution”	46
Table 3	Eigenvalues of “Contribution of Horizontal Tail’s Aerodynamics: size” . .	52
Table 4	Eigenvalues of “Contribution of Horizontal Tail’s Aerodynamics: location”	52
Table 5	Stiff and flexible beams beam properties: GJ (torsional stiffness: Nm^2), EI_2 , EI_3 (bending stiffness: Nm^2), N (number of elements), ℓ (length of the beam: m), and m (mass per unit length: kg/m)	53
Table 6	Static equilibrium solution of stiff and flexible beam (upper and lower tables for stiff and flexible beams respectively)	53
Table 7	Six GVT rigid-body and four lowest GVT structural modes and corresponding eigenvalues of stiff beam	56
Table 8	Ten lowest GVT modes and corresponding eigenvalues of flexible beam .	56
Table 9	Four lowest GVT structural modes of the free-free flexible beam simulated by NATASHA	67
Table 10	Beam and bungee cord properties for “Different Bungee Cord Locations”	69
Table 11	Eigenvalues of Cases 1 – 5 with four lowest eigenvalues of flexible and stiff beams	69
Table 12	Eigenvalues of cases 1, 3, and 5 with linear spring, and of the free-free flexible beam simulated by NATASHA	72
Table 13	Beam and bungee cord properties	82
Table 14	Ten lowest GVT modes and corresponding eigenvalues of flying wing configuration	82
Table 15	Ten lowest GVT modes and corresponding eigenvalues of conventional aircraft configuration	82
Table 16	Parameters for the reference configuration	84
Table 17	Parameters in “Periodic Inertia Effect”	89
Table 18	Parameters in “Periodic Propeller Airloads”	93

LIST OF FIGURES

Figure 1	Schematic of two beam configuration	18
Figure 2	Schematic of bungee connection to a node	21
Figure 3	Schematic of incorporation bungee formulation to intrinsic beam formulation	29
Figure 4	Schematic of simple Engine/Propeller system	37
Figure 5	Trim configuration of Case I of “Payload Distribution”	47
Figure 6	Trim configuration of Case II of “Payload Distribution”	47
Figure 7	Root locus of three lowest eigenvalues of “Payload Distribution” (lower figure is zoomed in for 1 st and 2 nd eigenvalues)	48
Figure 8	Root locus of seven lowest eigenvalues depending on beam flexibility . . .	49
Figure 9	Root locus of three lowest eigenvalues of “Contribution of Horizontal Tail’s Aerodynamics: size”	51
Figure 10	Root locus of three lowest eigenvalues of “Contribution of Horizontal Tail’s Aerodynamics: location”	51
Figure 11	3D plot of the GVT static equilibria of stiff and flexible beams	54
Figure 12	2D plot of the static equilibria of stiff and flexible beams	55
Figure 13	1 st and 2 nd GVT rigid-body modeshapes of stiff beam	57
Figure 14	3 rd and 4 th GVT rigid-body modeshapes of stiff beam	58
Figure 15	5 th and 6 th GVT rigid-body modeshapes of stiff beam	59
Figure 16	1 st and 2 nd GVT structural modeshapes of stiff beam	60
Figure 17	3 rd and 4 th GVT structural modeshapes of stiff beam	61
Figure 18	1 st and 2 nd GVT rigid-body modeshapes of flexible beam	62
Figure 19	3 rd and 4 th GVT rigid-body modeshapes of flexible beam	63
Figure 20	5 th and 6 th GVT rigid-body modeshapes of flexible beam	64
Figure 21	1 st and 2 nd GVT structural modeshapes of flexible beam	65
Figure 22	3 rd and 4 th GVT structural modeshapes of flexible beam	66
Figure 23	Static equilibria of Cases 1 – 5 (from top to bottom, from left to right, the case number increases as the bungee cord location moves to the mid-span)	70
Figure 24	Relative difference of 4 lowest elastic modes of Cases 1 – 5 with respect to those of the free-free beam simulated by NATASHA. (x axis corresponds to the case number)	71

Figure 25	Relative difference of 4 lowest elastic modes for Cases 1 – 5 with respect to those of the free-free beam simulated by NATASHA. (x axis corresponds to the case number)	71
Figure 26	3D plot of GVT static equilibria of flying wing and conventional configuration	74
Figure 27	1 st and 2 nd GVT structural modeshapes of flying wing configuration . . .	75
Figure 28	3 rd and 4 th GVT structural modeshapes of flying wing configuration . . .	76
Figure 29	1 st and 2 nd GVT rigid-body modeshapes of conventional configuration . .	77
Figure 30	3 rd and 4 th GVT rigid-body modeshapes of conventional configuration . .	78
Figure 31	5 th and 6 th GVT rigid-body modeshapes of conventional configuration . .	79
Figure 32	1 st and 2 nd GVT structural modeshapes of conventional configuration . .	80
Figure 33	3 rd and 4 th GVT structural modeshapes of conventional configuration . .	81
Figure 34	Trim configuration of highly flexible flying wing aircraft with two Engine/Propeller systems	83
Figure 35	Time history of decaying tip transverse position and angle of attack . . .	85
Figure 36	Time history of decaying pitch (α) and yaw angles (β)	85
Figure 37	Time history of divergent tip transverse position and angle of attack . . .	86
Figure 38	Time history of divergent pitch and yaw angles	86
Figure 39	Time history of tip transverse position and angle of attack in periodic oscillation	87
Figure 40	Time history of pitch and yaw angles in periodic oscillation	87
Figure 41	α vs $\dot{\alpha}$ and β vs $\dot{\beta}$ in phase plane in divergent case	90
Figure 42	α vs $\dot{\alpha}$ and β vs $\dot{\beta}$ in phase plane in periodic oscillation	90
Figure 43	Boundary for whether two-bladed Engine/Propeller system can be approximated as equivalent three-bladed Engine/Propeller system	91
Figure 44	Propeller side forces (Y, H) per number of blades	94
Figure 45	Propeller hub moments (M_x, M_z) per number of blades	95
Figure 46	Time history of tip transverse position and angle of attack	96
Figure 47	α vs $\dot{\alpha}$ and β vs $\dot{\beta}$ in phase plane	96
Figure 48	Time history of tip transverse position and angle of attack with less payload at mid-span	97
Figure 49	α vs $\dot{\alpha}$ and β vs $\dot{\beta}$ in phase plane with less payload at mid-span	97
Figure 50	Bending moment distribution along the span from NATASHA _{GVT} and Euler-Bernoulli Beam Theory	99

Figure 51	$\ \mathbf{r}\ _2$ with respect to the number of element on a log scale	99
Figure 52	Angle of attack in trim condition by NATASHA and RCAS	100
Figure 53	Nodal force and moment resultants from NATASHA and RCAS	101
Figure 54	Comparison of the propeller airload evaluation between NATASHA and RCAS	102
Figure 55	Schematic of GVT rigid-body modes and its ideal models	108
Figure 56	Schematic of simple engine/propeller system	110

NOMENCLATURE

Bungee Formulation

\mathbf{n}_i	unit basis vector of inertial frame
\mathbf{B}_i	unit basis vector of body fixed reference frame
P	potential energy
K	kinetic energy
g	acceleration of gravity
Δ	identity matrix
O	origin of the inertial frame
B^*	center of mass of rigid body
B	reference point of rigid body
Q_k	point in an inertial frame attached to the k^{th} bungee cord
P_k	point in a rigid body attached to the k^{th} bungee cord
\mathbf{P}_{OB^*}	position vector from O to B^*
ξ	position vector from B^* to an arbitrary point in the body
C	rotation matrix from the inertial frame to the body reference frame
m	mass of rigid body
K_k	stiffness of the k^{th} bungee cord
ℓ_k	natural length of the k^{th} bungee cord
σ_k	stretch of the k^{th} bungee cord
τ_k	unit vector along the k^{th} bungee cord
ϵ_k	slack variable for the k^{th} bungee cord
F_k	Lagrange multiplier interpreted as tension of the k^{th} bungee cord
μ_k	Lagrange multiplier to enforce the unit vector condition for each τ_k
δ	variational operator
$\overline{\delta A}$	virtual action
$\overline{\delta W}$	virtual work

$\overline{\delta q}$	virtual displacement
$\overline{\delta \psi}$	virtual rotation
x_n	$\mathbf{x} \cdot \mathbf{n}_i$ matrix components in inertial basis
x_B	$\mathbf{x} \cdot \mathbf{B}_i$ matrix components in body fixed reference frame basis

Beam Formulation

B	deformed beam reference frame (B frame)
i	inertial frame
F	internal force measures in the B frame
M	internal moment measures in the B frame
V	velocity measures in the B -frame
Ω	angular velocity measures in the B frame
g	the measure numbers of the gravity vector in the B frame
C^{iB}	rotation matrix from B frame to i
γ	internal strain measures
κ	internal curvature measures
P	linear momentum measures
H	angular momentum measures
\hat{x}	nodal variables
\bar{x}	elemental variables

Engine/Propeller Modeling

m_1	pylon mass
m_2	total blade mass
h	pylon length
d	blade diameter
\mathbf{V}_E	velocity vector of pylon center of mass

\mathbf{V}_P	velocity vector of total propeller center of mass
$\mathbf{\Omega}_E$	angular velocity vector of pylon
$\mathbf{\Omega}_P$	angular velocity vector of propeller
ξ_E	position vector from beam reference line to pylon center of mass
ξ_P	position vector from beam reference line to propeller center of mass
\mathbf{V}	velocity vector of wing reference line where an Eng/Prop system is attached
$\mathbf{\Omega}$	angular velocity vector of wing reference frame where an Eng/Prop system is attached
$\mathbf{\Omega}_{\alpha\beta}$	relative angular velocity vector of pylon to the wing reference frame
α	pylon pitch angle defined from the wing reference frame
β	pylon yaw angle defined from the wing reference frame
Ψ	azimuth angle
$\hat{\mathbf{g}}$	gravity vector
i_P	inertia matrix in hub fixed reference frame
\mathbf{V}_B	velocity vector of arbitrary point on a blade
Θ	twist angle of blade
Y	side force along pitch direction
T	thrust
H	side force along yaw direction
M_x	hub moment along pitch direction
Q_o	toque in propeller aerodynamics
M_z	hub moment along yaw direction
\mathbf{F}_{prop}	propeller force vector
\mathbf{M}_{prop}	propeller hub moment vector

SUMMARY

The highly flexible HALE (High Altitude Long Endurance) aircraft analysis methodology is of interest because early studies indicated that HALE aircraft might have different vibration and aeroelastic characteristics from those of conventional aircraft.

Recently the computer code Nonlinear Aeroelastic Trim And Stability of HALE Aircraft (NATASHA) was developed under NASA sponsorship. NATASHA can predict the flight dynamics and aeroelastic behavior for HALE aircraft with a flying wing configuration. Further analysis improvements for NATASHA were required to extend its capability to the ground vibration test (GVT) environment and to both GVT and aeroelastic behavior of HALE aircraft with other configurations.

First, the analysis methodology, based on geometrically exact fully intrinsic beam theory, was extended to treat other aircraft configurations. Conventional aircraft with flexible fuselage and tail can now be modeled by treating the aircraft as an assembly of beam elements. NATASHA is now applicable to any aircraft configuration that can be modeled this way. The intrinsic beam formulation, which is a fundamental structural modeling approach, is now capable of being applying to a structure consisting of multiple beams by relating the virtual displacements and rotations at points where two or more beam elements are connected to each other. Additional aspects are also considered in the analysis such as auxiliary elevator input in the horizontal tail and fuselage aerodynamics.

Second, the modeling approach was extended to treat the GVT environment for HALE aircraft, which have highly flexible wings. GVT has its main purpose to provide modal characteristics for model validation. A bungee formulation was developed by the augmented Lagrangian method and coupled to the intrinsic beam formulation for the GVT modeling. After the coupling procedure, the whole formulation cannot be fully intrinsic because the geometric constraint by bungee cords makes the system statically indeterminate. Displacement and rotation variables need to be introduced, but only at points to which bungee cords

are attached.

Third, because many HALE aircraft are propeller driven, the structural modeling was extended to include an engine/nacelle/propeller system using a two-degree-of-freedom model with pitch and yaw angles. This step was undertaken to predict a dynamic instability called “whirl flutter,” which can be exhibited in such HALE aircraft. It can investigate how the nacelle whirling and wing motions affect each other. For simplicity, two fundamental assumptions are made regarding the propeller aerodynamics and inertia matrix of two-bladed propeller system. The propeller airloads are evaluated by the constant approximation which uses the averaged values for one revolution per blade. Periodic side forces and hub moments are evaluated based on how they affect the trim condition determined by the constant approximation. The next assumption is for certain HALE aircraft which can use a two-bladed propeller system. The inertia matrix appears as periodic in time in the governing equations. If the periodic inertia effect is negligible, then the inertia matrix can be replaced by that of equivalent three-bladed propeller system so that the stability analysis can obviate the need for Floquet theory.

These new development have been fully integrated into the current version of NATASHA. Finally, a parametric study for representative HALE aircraft is presented to show how the current methodology can be utilized as a unified preliminary analysis tool for the vibration and aeroelastic analysis of highly flexible HALE aircraft.

CHAPTER I

INTRODUCTION

HALE (High-Altitude Long-Endurance) aircraft are typically highly flexible and are being developed for environmental science research, telecommunication relay service and military reconnaissance missions. Among such aircraft, the solar-powered “Helios” (manufactured by Aerovironment, Inc.) flew at an altitude of 98,000 feet, thus achieving the world’s altitude record for propeller-driven aircraft. Such aircraft are envisioned to become “atmospheric satellites” engaging in missions with duration of several months or even years.

One big difference between such aircraft and conventional ones is that they operate with large wing deflections. Therefore, structural nonlinearities must be taken into consideration, because linear theory cannot correctly explain the aeroelastic behavior. It is known that rigid-body modes couple with low elastic modes as the wing flexibility increases for highly flexible aircraft [61, 64]. Aeroelastic analyses for flexible aircraft show that the phugoid mode can be mildly unstable [61] and the flight dynamic modes can be affected by lowest elastic modes [42].

This demands that further analysis should address possible improvements in the modeling and design of highly flexible HALE aircraft to predict its aeroelastic behavior accurately. Besides, the configuration of such aircraft in a trimmed flight condition might be different from the one of Ground Vibration Testing (GVT). Therefore, the GVT processes and results should be newly understood as to how the results apply to the aeroelastic behavior of such aircraft.

For long-term missions, some highly flexible HALE type aircraft use electric fuel cells as a source of power to run propellers, and solar panels are charged during daylight. As a propeller driven aircraft, it may exhibit another type of dynamic instability called “whirl flutter.” A rotating propeller motion can be affected by large deformation of the wing (and vice versa).

To relate previous works to the current work and to give a vision for future work, which can provide unified preliminary analysis for highly flexible HALE aircraft, the literature survey is given in several parts: nonlinear aeroelastic analysis, bungee system, ground vibration test, and whirl-flutter instability.

1.1 Nonlinear Aeroelastic Analysis

While testing a human-powered aircraft with a high aspect ratio (≈ 40), Zerweckh et al. [68] developed a fully flexible aeroelastic model using an assumed mode approach [61] to analyze its aeroelastic behavior and to compare the test data to pre-test analysis. Their results concluded that the phugoid mode was mildly unstable and further studies should consider the structural flexibility and unsteady aerodynamics to analyze the aeroelastic behavior accurately and correctly. The study also indicated that many elastic modes are recommended to be included in a modal model of a HALE aircraft.

Prior to this work, the effects of structural nonlinearity on modal characteristics were investigated by Waszak and Schmidt [64]. The nonlinear equations of motion for an elastic airplane were formulated by the Lagrangian method using strip theory aerodynamics. The frequency responses of residualized models of different orders were compared (eliminating higher-order aeroelastic effects). It also showed that the frequency separation between rigid-body modes and elastic modes becomes less obvious as flexibility increases because of the aeroelastic effect. Then this work was extended to high-fidelity simulation of flexible aircraft using a modal based model [50].

Various numerical simulations of HALE aircraft were developed to investigate the aeroelastic analysis. Hodges and co-workers investigated the nonlinear aeroelasticity and flight dynamics taking into account the structural geometric nonlinearity and unsteady flow. Their results indicated that the elastic modes in low frequencies affected the phugoid mode as well as the short-period mode [42]. They expanded it to the nonlinear aeroelastic stability analysis [43] and the design of the output feedback controller to suppress flutter and alleviate gust loads [41]. Recently, Patil and Hodges developed the computer code Nonlinear Aeroelastic Trim and Stability of HALE Aircraft (NATASHA) [44], based on previous theoretical work

in which governing equations are the geometrically-exact equations of motion [22] written in their intrinsic form augmented with intrinsic kinematical equations [23]. NATASHA predicts correctly the unusual flight dynamics behavior of certain HALE configurations [44].

Meirovitch and Tuzcu developed a unified theory of maneuvering flexible aircraft [38] and associated time simulation [37] focusing on dynamics and control. Their formulation was extended from a previous development of hybrid equations of motion [36], which combines rigid-body and flexible sub-systems for modeling a satellite with elastic appendages.

Moreover, a high-fidelity nonlinear fluid dynamic model was taken to investigate the nonlinear aeroelastic analysis. Ref. [16] applied a CFD solver for Euler/Navier-Stokes computational fluid dynamic analysis to a beam finite element model. Numerical results for both unswept and swept wing cases, with linear and nonlinear structural representation, are compared and discussed for the tip stall characteristics. Ref. [56] studied the HALE joined-wing aircraft as a NASTRAN Finite Element Model coupled with an Euler/Navier-Stokes CFD solver.

1.2 *Bungee System*

The fundamental dynamic model for simulation of GVT with a bungee system is quite similar to those of other areas such as modeling of cable-suspended robots (RoboCrane) [1, 2], marine cable [62], mooring systems [14], and cable dorns [11]. Depending on its research purpose, a dynamic model may be formulated differently. A point mass was taken to focus on optimal force distribution for a given trajectory of the RoboCrane [51, 52]. Roberts et al. [48] examined inverse kinematics and statics of a rigid-body model only for the fully constrained configurations, for which no cable is in the slack condition. In ocean engineering, a rigid cylinder was taken to represent simple model for moored breakwaters with six rigid-body degrees of freedom [35]. A more detailed nonlinear dynamic analysis of the cable itself also was developed as a lumped parameter system [28] and as a finite element model [17]; analytical and experimental studies are found in Ref. [18]. However, the main focus of the current GVT simulation is not the nonlinear dynamic analysis of cables or ropes themselves but of the dynamical systems to which they are attached. However, for

future work more detailed modeling of these parts might be considered as means to obtain an improved simulation.

For GVT, stiffnesses of the bungee cords should be chosen sufficiently low to minimize coupling between GVT rigid-body modes and the lowest frequency elastic modes. (GVT rigid-body modes are the modes in which the beam behaves like a rigid body, such as pitching, rolling, plunging, twisting and two swing modes. See the details about GVT rigid-body modes in Appendix A.) However, low stiffness can lead to quite large elongations. Even though the main modeling interest is not the GVT bungee system, the nonlinear dynamic behavior needs to be described properly. Different strain-energy functions have been modeled to describe the elastic behavior in large elongation by mathematical descriptions to match its experiment data [31, 60] and infinite sum of strain invariants [4, 25, 39]. Ref. [31] characterizes the stress-strain curve mathematically in three particular types depending on material characteristics. Ref. [60] uses piecewise linear approximation on stress-strain curve for application to mooring systems with a total stretch in the range from 2% to 250%. It is known that the strain energy function can be expressed in terms of infinite series of strain invariants by Mooney and Rivlin [25, 39]. Ref. [4] also expressed the final form of strain energy function in terms of strain invariants with additional parameters such as chain density, Boltzmann's constant, and temperature. Instead of expressing strain energy function directly in terms of strain invariants, Ogden [39] proposed that a strain energy function is a linear combination of strain invariants defined by three principal stretches and some parameters to match to experimental data. The current analysis is based on the Hencky strain energy analysis [3, 10], which showed good accuracy for moderate deformation of several real materials [3] and good agreements with experimental data for large axial elongation [10].

When it is not possible to provide a sufficiently low bungee stiffness, especially for large structures, a zero-spring-suspension system [30, 59, 65] is often used to allow relatively stiff cable for GVT by providing negative stiffness. However, the estimated prestressed load in the zero-spring-suspension might be sensitive to imperfections caused in actual GVT. It might not provide exactly zero stiffness.

The proposed bungee is modeled as an extensible cord. Due to the slack condition of bungee cords, compression is not allowed. This means that unilateral behavior of the cable in both taut and slack conditions should be considered properly. Modeling has been explored for the unilateral behavior of a cable in both taut and slack conditions by several means such as zero tension [6, 12], zero stiffness [63], and by use of two possible relations between the acceleration of wire distance variable and zero tension [40]. This suggests a mathematically rigorous way to model the slack condition by introducing an additional slack variable and applying it as a constraint to the system.

1.3 Ground Vibration Test

With the advent of highly flexible HALE type aircraft, the results of GVT should be understood afresh in light of how those results apply to the aeroelastic behavior of such aircraft, because the shape of the vehicle in a trimmed flight condition might be very different than the one of GVT which is suspended from bungee cords on the ground. Ref. [61] tried to match the deformed shape of highly flexible aircraft in GVT as close as possible to the in-flight shape by modifying the beam bending stiffness (EI). To determine the mode shapes, the GVT setup was done so that each wing tip was attached to wires, and the beam was loaded with steady aerodynamic loads. (In a usual GVT, a bungee cord or other supporting system is attached close to center of mass. For highly flexible aircraft, this choice might lead to the opposite wing deflection of the in-flight shape configuration.)

One of possible improvements in GVT is to consider the structural nonlinearity at an early stage of GVT. This will reduce significantly the duration of a given GVT. (GVT flow diagram and duration for large aircraft are described in Ref. [34].) Ref. [20] summarized several ways of detecting, identifying and characterizing nonlinearities, such as Hilbert transform [53], homogeneity check, inverse frequency response function approach (IFRF), and Modified Restoring Force Surface (MRFS) approach [29]. Goge et al. [21] suggested its application to aerospace structures, which were referred to as INTL (Identification of Nonlinearities by Time-series based Linearity plots) test strategy.

From experimental GVT analysis, the analytical model can be updated by forming a

residual in eigenvalues and mode shapes or eigenvalues and frequency responses by computational model updating (CMU) method [19]. Blakely checked the correlation between modeshapes from pre-test analysis and the one from GVT by calculating cross-orthogonality [8]. Ref. [9] described a model refinement technique to match both frequency responses. Yang and Brown developed a perturbed boundary condition (PBC) model updating technique [67] and another technique which adds damping in the finite element model [66].

1.4 Whirl Flutter Instability

Whirl-flutter is another type of dynamic instability for propeller-driven aircraft. The instability was recognized as “undamped propeller whirl mode” [58] and “unstable low-frequency reverse-rotating precession” [49]. A simple analysis model in Ref. [32] demonstrates the characteristics of whirl-flutter stability. However, such a phenomenon was not likely to happen in that era. Ref. [24] attempted to understand whirl flutter by isolating related parameters such as pitch and yaw stiffness of the nacelle, structural damping, and propeller angular speed after turbopropeller aircraft and unusual VTOL configurations were of interests.

Bennett and Bland [5] first attempted to understand whirl-flutter instability of rigid engine-propeller system with the effect of wing. The analytical model was based on four modes: two relative degrees of freedom (pitch and yaw) of power plant to the wing and two elastic beam bending and torsion modes. In the results, certain configurations showed that the wing stabilized whirl flutter, and wing flutter was also stabilized by the large concentrated mass of propeller which was located ahead of the elastic axis. The study indicated that the wing aerodynamics is quite important to investigate the whirl-flutter stability due to a significant coupling of wing and propeller motion. This four-mode analysis showed improved agreement to experimental results than previous two mode analysis without elastic modes [47].

In the 60’s, a new concept of tiltrotor systems, originating from the developement of the Bell XV-3 convertiplane, was proposed to take advantages of both fixed-wing aircraft and helicopters. The tilt-rotor mechanism has angular degrees of freedom for pitch and yaw, which can make it prone to whirl-flutter instability. Edenborough [15] demonstrated that

some configuration of tilt-rotor VTOL aircraft could fly avoiding “rotor-pylon instability” at high speed after investigating major parameters such as swashplate-pylon coupling, pylon mounting stiffness, rotor pitch-flap coupling, and wing effect.

Johnson contributed to the development of analytical models to study tilting proprotors. In Ref. [26], a nine-degree-of-freedom model including three flapping, three lead-lag and three elastic wing motions was developed to deal with classical whirl flutter in high inflow axial flight. In Ref. [27] several requirements for analytical modeling of tilting proprotors were pointed out and discussed, such as the influence of coupled flap and lag blade bending motions, autorotation vs. powered rotation cases, rotor aerodynamics in high inflow, and the effect of nonaxial flow which leads periodic effect to dynamic analysis.

A comprehensive analysis model was also formulated. The original University of Maryland Advanced Rotorcraft Code (UMARC) formulation, for a helicopter configuration, was modified to incorporate a tiltrotor configuration with full wingspan and twin rotors [57]. Its predictions correlate well with the flight test data and with Bell Helicopter Textron’s C81 analysis. The continued work in Ref. [54] focused on whirl-flutter stability of two-bladed proprotor/pylon systems, which equation of motion is different from that for systems with three or more blades because of periodic coefficients. The analytical model predicted that the two-bladed system experienced a new type of instability at 1/rev frequency similar to the wing torsional divergence after comparing frequency and damping characteristics of system with two and three blades at different speeds.

Some research has also focused on lowering the whirl-flutter speed. Ref. [46] presented a possible structural coupling in the wing to see the influence on whirl-flutter instability. The wing coupling introduced by the proposed wing tilt angle showed that a wing coupling can improve the stability characteristics. Ref. [33] developed a generalized predictive control for tiltrotor aircraft. Their works resulted in a predictive toolbox in MATLAB. Several types of controllers were addressed to improve the whirl-flutter stability by means of a wing trailing-edge flap (wing flaperon) and rotor swashplate [55].

CHAPTER II

FOUNDATIONAL WORK

Aeroelastic modeling of a highly flexible aircraft undergoing large deformation requires a geometrically nonlinear structural model coupled with a consistent large motion aerodynamic model. The previous work builds on the development of the computer code NATASHA [44]. NATASHA takes into account the structural nonlinearities in a novel manner and predicts correctly the unusual flight dynamics behavior of certain HALE configurations. The governing equations are geometrically exact, but they are also quite simple. Structurally the aircraft lifting surfaces are modeled as beams undergoing large displacement and rotation. The governing equations are the geometrically-exact equations of motion from Ref. [22] written in their intrinsic form. However, instead of being augmented by kinematical relations therein, they are augmented by intrinsic kinematical equations, derived in Ref. [23] by eliminating the displacement and rotational variables from the kinematical equations of Ref. [22]. The 2-D aerodynamics is taken to evaluate the aerodynamic forces and moments on the high-aspect-ratio wing. The unsteady effect is also included in the analysis by using the inflow theory of Peters et al. [45].

2.1 Structural Model

2.1.1 Intrinsic Beam Formulation

The geometrically exact, intrinsic governing equations for the dynamics of a general, non-uniform, twisted, curved, anisotropic beam, are

$$\begin{aligned}
 F'_B + \widetilde{K}_B F_B + f_B &= \dot{P}_B + \widetilde{\Omega}_B P_B \\
 M'_B + \widetilde{K}_B M_B + (\tilde{e}_1 + \tilde{\gamma}) F_B + m_B &= \dot{H}_B + \widetilde{\Omega}_B H_B + \widetilde{V}_B P_B \\
 V'_B + \widetilde{K}_B V_B + (\tilde{e}_1 + \tilde{\gamma}) \Omega_B &= \dot{\gamma} \\
 \Omega'_B + \widetilde{K}_B \Omega_B &= \dot{\kappa}
 \end{aligned} \tag{1}$$

where F_B and M_B are the internal force and moment measures, P_B and H_B are the sectional linear and angular momenta, V_B and Ω_B are the velocity and angular velocity measures, γ and κ are the force and moment strain measures, $K_B = k_b + \kappa$ is the curvature vector and k_b is the initial twist and curvature of the beam. f_B and m_B include all the external forces and moments such as gravity, aerodynamic forces and moments, and control forces and moments.

The variables in Eq. (1) such as the generalized momenta (P_B and H_B) and strains (γ and κ) are secondary variables. The constitutive equation and generalized momentum-velocity relation are needed to relate them to the primary variables. For small strain, the constitutive equations are

$$\begin{Bmatrix} \gamma \\ \kappa \end{Bmatrix} = \begin{bmatrix} R & S \\ S^T & T \end{bmatrix} \begin{Bmatrix} F_B \\ M_B \end{Bmatrix} \quad (2)$$

where R , S , and T are 3×3 submatrices of the cross-sectional flexibility matrix. The generalized momentum-velocity relations are

$$\begin{Bmatrix} P_B \\ H_B \end{Bmatrix} = \begin{bmatrix} \mu\Delta & -\mu\tilde{\xi} \\ \mu\tilde{\xi} & I \end{bmatrix} \begin{Bmatrix} V_B \\ \Omega_B \end{Bmatrix} \quad (3)$$

where μ is the mass per unit length, Δ is the identity matrix, ξ is the cross-sectional mass centroid offset, and I is the inertia matrix per unit length. Moreover, the tilde operation ($\tilde{\cdot}$) is defined for a column matrix ($a = [a_1 \ a_2 \ a_3]^T$)

$$\tilde{a} = \begin{bmatrix} 0 & -a_3 & a_2 \\ a_3 & 0 & -a_1 \\ -a_2 & a_1 & 0 \end{bmatrix} \quad (4)$$

2.1.2 Finite-element Discretization

A space-time discretization scheme given in Ref. [23] satisfying both space-time conservation laws is applied to the governing equation. For arbitrary variable X in the equation, \hat{X}_ℓ^n and \hat{X}_r^n are the n^{th} nodal variables defined at left and right of the node so that the discretization can express the discontinuity such as nodal mass, nodal inertia, nodal kink, etc. The first

derivative in space is discretized as

$$X' = \frac{\widehat{X}_\ell^{n+1} - \widehat{X}_r^n}{d\ell} \quad (5)$$

Any variable X defined in an element interior corresponds to the n^{th} element variable (\overline{X}^n) is expressed in terms of adjacent nodal variables:

$$\overline{X}^n = \frac{\widehat{X}_\ell^{n+1} + \widehat{X}_r^n}{2} \quad (6)$$

The n^{th} element equations which are discretized from the Eq. (1) are

$$\begin{aligned} \frac{\widehat{F}_l^{n+1} - \widehat{F}_r^n}{dl} + (\widetilde{\kappa}^n + \widetilde{k}^n)\overline{F}^n + \overline{f}^n - \dot{\overline{P}}^n - \widetilde{\Omega}^n\overline{P}^n &= 0 \\ \frac{\widehat{M}_l^{n+1} - \widehat{M}_r^n}{dl} + (\widetilde{\kappa}^n + \widetilde{k}^n)\overline{M}^n + (\widetilde{e}_1 + \widetilde{\gamma}^n)\overline{F}^n + \overline{m}^n - \dot{\overline{H}}^n - \widetilde{\Omega}^n\overline{H}^n - \widetilde{V}^n\overline{P}^n &= 0 \\ \frac{\widehat{V}_l^{n+1} - \widehat{V}_r^n}{dl} + (\widetilde{\kappa}^n + \widetilde{k}^n)\overline{V}^n + (\widetilde{e}_1 + \widetilde{\gamma}^n)\overline{\Omega}^n - \dot{\overline{\gamma}}^n &= 0 \\ \frac{\widehat{\Omega}_l^{n+1} - \widehat{\Omega}_r^n}{dl} + (\widetilde{\kappa}^n + \widetilde{k}^n)\overline{\Omega}^n - \dot{\overline{\kappa}}^n &= 0 \end{aligned} \quad (7)$$

where \overline{f}^n and \overline{m}^n include any external forces and moments applied at n^{th} element. The element variables (\overline{X}^n) are secondary variables. So they are related to the primary nodal variables as follows:

$$\begin{aligned} \overline{F}^n &= \frac{\widehat{F}_l^{n+1} + \widehat{F}_r^n}{2} \\ \overline{M}^n &= \frac{\widehat{M}_l^{n+1} + \widehat{M}_r^n}{2} \\ \overline{V}^n &= \frac{\widehat{V}_l^{n+1} + \widehat{V}_r^n}{2} \\ \overline{\Omega}^n &= \frac{\widehat{\Omega}_l^{n+1} + \widehat{\Omega}_r^n}{2} \end{aligned} \quad (8)$$

If the beam has any discontinuity such as nodal mass, nodal force, and slope, the nodal variables (\widehat{X}_ℓ^n and \widehat{X}_r^n) are not simply equal to each other ($\widehat{X}_\ell^n = \widehat{X}_r^n$). The nodal equations need to include all the discontinuity, so that

$$\widehat{F}_r^n - \widehat{C}_{lr}^{nT} \widehat{F}_l^n + \widehat{f}^n - \dot{\widehat{P}}_r^n - \widetilde{\Omega}_r^n \widehat{P}_r^n = 0 \quad (9)$$

$$\widehat{M}_r^n - \widehat{C}_{lr}^{nT} \widehat{M}_l^n + \widehat{m}^n - \dot{\widehat{H}}_r^n - \widetilde{\Omega}_r^n \widehat{H}_r^n - \widetilde{V}_r^n \widehat{P}_r^n = 0 \quad (10)$$

where \hat{C}_{lr} reflects the slope discontinuity, \hat{f}^n and \hat{m}^n are external forces and moments applied at n^{th} node, and

$$\begin{aligned}\hat{V}_l^n &= \hat{C}_{lr}^n \hat{V}_r^n \\ \hat{\Omega}_l^n &= \hat{C}_{lr}^n \hat{\Omega}_r^n \\ \hat{g}_l^n &= \hat{C}_{lr}^n \hat{g}_r^n\end{aligned}\tag{11}$$

2.1.3 Gravity loads

The external force and moments in Eq. (1) include any external loads applied to the beam, which can include aerodynamic loads, gravity, control forces, etc.

$$\begin{aligned}f_B &= f_{\text{aero}} + f_{\text{control}} + f_g + \dots \\ m_B &= m_{\text{aero}} + m_{\text{control}} + m_g + \dots\end{aligned}\tag{12}$$

where $f_g = \mu g$ and $m_g = \mu \tilde{\xi} g$. If the gravitational force is added, the formulation needs additional equations. A unit gravity vector \mathbf{g} is known in the inertial frame and has column matrix $[0 \ 0 \ -1]^T$ when expressed in inertial basis. However, the governing equations are described in the deformed beam cross-sectional reference frame. The column matrix of the gravity vector measures expressed in this reference frame is in time and space,

$$\begin{aligned}g' + (\tilde{\kappa} + \tilde{k})g &= 0 \\ \dot{g} + \tilde{\Omega}g &= 0\end{aligned}\tag{13}$$

The corresponding discretized forms are

$$\begin{aligned}\frac{\hat{g}_l^{n+1} - \hat{g}_r^n}{dl} + (\tilde{\kappa}^n + \tilde{k}^n)\bar{g}_r^n &= 0 \\ \dot{\hat{g}}_r^n + \tilde{\Omega}_r^n \hat{g}_r^n &= 0\end{aligned}\tag{14}$$

If the column matrix for the gravity vector measures in the cross-sectional reference frame is known at one node, then the column matrix at other nodes and in time can be obtained from these relations. In addition, the unit gravity vector \mathbf{g} also should satisfy the condition

$$|\mathbf{g}| = 1\tag{15}$$

This unit vector condition replaces one of Eqs. (14) at the reference node providing a boundary condition to determine a trim condition; see Eqs. (23) below.

2.1.4 Final Structural equations

The final structural equation expressed in finite element discretization are now presented.

The n^{th} nodal equations are

$$\begin{aligned}\widehat{F}_r^n - \widehat{C}_{lr}^{nT} \widehat{F}_l^n + \widehat{f}_T^n + \widehat{\mu}^n \widehat{g}_r^n + \widehat{f}_{\text{aero}}^n - \dot{\widehat{P}}_r^n - \widetilde{\widehat{\Omega}}_r^n \widehat{P}_r^n &= 0 \\ \widehat{M}_r^n - \widehat{C}_{lr}^{nT} \widehat{M}_l^n + \widehat{m}_T^n + \widehat{\mu}^n \widetilde{\widehat{\xi}}^n \widehat{g}_r^n + \widehat{m}_{\text{aero}}^n - \dot{\widehat{H}}_r^n - \widetilde{\widehat{\Omega}}_r^n \widehat{H}_r^n - \widetilde{\widehat{V}}_r^n \widehat{P}_r^n &= 0\end{aligned}\quad (16)$$

The n^{th} element equations are

$$\begin{aligned}\frac{\widehat{F}_l^{n+1} - \widehat{F}_r^n}{dl} + (\widetilde{\kappa}^n + \widetilde{k}^n) \overline{F}^n + \overline{f}_{\text{aero}}^n + \mu^n \overline{g}^n - \dot{\overline{P}}^n - \widetilde{\overline{\Omega}}^n \overline{P}^n &= 0 \\ \frac{\widehat{M}_l^{n+1} - \widehat{M}_r^n}{dl} + (\widetilde{\kappa}^n + \widetilde{k}^n) \overline{M}^n + (\widetilde{e}_1 + \widetilde{\gamma}^n) \overline{F}^n + \overline{m}_{\text{aero}}^n + \mu^n \widetilde{\xi}^n \overline{g}^n - \dot{\overline{H}}^n - \widetilde{\overline{\Omega}}^n \overline{H}^n - \widetilde{\overline{V}}^n \overline{P}^n &= 0\end{aligned}\quad (17)$$

The intrinsic kinematical equations for the n^{th} element are now

$$\begin{aligned}\frac{\widehat{C}_{lr}^{n+1} \widehat{V}_r^{n+1} - \widehat{V}_r^n}{dl} + (\widetilde{\kappa}^n + \widetilde{k}^n) \overline{V}^n + (\widetilde{e}_1 + \widetilde{\gamma}^n) \overline{\Omega}^n - \dot{\widetilde{\gamma}}^n &= 0 \\ \frac{\widehat{C}_{lr}^{n+1} \widehat{\Omega}_r^{n+1} - \widehat{\Omega}_r^n}{dl} + (\widetilde{\kappa}^n + \widetilde{k}^n) \overline{\Omega}^n - \dot{\widetilde{\kappa}}^n &= 0\end{aligned}\quad (18)$$

The equation for the gravity column matrix for the n^{th} element is

$$\frac{\widehat{C}_{lr}^{n+1} \widehat{g}_r^{n+1} - \widehat{g}_r^n}{dl} + (\widetilde{\kappa}^n + \widetilde{k}^n) \overline{g}^n = 0 \quad (19)$$

The following equations are the secondary equations needed to complete the formulation.

The constitutive equations in the n^{th} element are

$$\begin{Bmatrix} \overline{\gamma}^n \\ \overline{\kappa}^n \end{Bmatrix} = \begin{bmatrix} R^n & S^n \\ S^{nT} & T^n \end{bmatrix} \begin{Bmatrix} \overline{F}^n \\ \overline{M}^n \end{Bmatrix} \quad (20)$$

The generalized momentum-velocity relations for both elements and nodes are

$$\begin{aligned}\begin{Bmatrix} \overline{P}^n \\ \overline{H}^n \end{Bmatrix} &= \begin{bmatrix} \mu^n \Delta & -\mu^n \widetilde{\xi}^n \\ \mu^n \widetilde{\xi}^n & I^n \end{bmatrix} \begin{Bmatrix} \overline{V}^n \\ \overline{\Omega}^n \end{Bmatrix} \\ \begin{Bmatrix} \widehat{P}_r^n \\ \widehat{H}_r^n \end{Bmatrix} &= \begin{bmatrix} \widehat{\mu}^n \Delta & -\widehat{\mu}^n \widetilde{\xi}^n \\ \widehat{\mu}^n \widetilde{\xi}^n & \widehat{I}^n \end{bmatrix} \begin{Bmatrix} \widehat{V}_r^n \\ \widehat{\Omega}_r^n \end{Bmatrix} + \begin{Bmatrix} 0 \\ \widehat{H}_{\text{engine}}^n \end{Bmatrix}\end{aligned}\quad (21)$$

The relations between nodal variables and element variable are

$$\begin{aligned}
\bar{F}^n &= \frac{\hat{F}_l^{n+1} + \hat{F}_r^n}{2} \\
\bar{M}^n &= \frac{\hat{M}_l^{n+1} + \hat{M}_r^n}{2} \\
\bar{V}^n &= \frac{\hat{C}_{lr}^{n+1}\hat{V}_r^{n+1} + \hat{V}_r^n}{2} \\
\bar{\Omega}^n &= \frac{\hat{C}_{lr}^{n+1}\hat{\Omega}_r^{n+1} + \hat{\Omega}_r^n}{2} \\
\bar{g}^n &= \frac{\hat{C}_{lr}^{n+1}\hat{g}_r^{n+1} + \hat{g}_r^n}{2}
\end{aligned} \tag{22}$$

The following boundary conditions complete the problem.

$$\begin{aligned}
\hat{F}_l^1 &= 0 \\
\hat{M}_l^1 &= 0 \\
\hat{F}_r^{N+1} &= 0 \\
\hat{M}_r^{N+1} &= 0 \\
(e_1 e_1^T + e_2 e_2^T) \dot{\hat{g}}_r^n + (e_1 e_1^T + e_2 e_2^T) \widetilde{\hat{\Omega}}_r^n \hat{g}_r^n + (e_3 e_3^T) |\hat{g}_r^n| &= 0
\end{aligned} \tag{23}$$

where $|\hat{g}_r^n| = \sqrt{g_1^{n^2} + g_2^{n^2} + g_3^{n^2}}$. (g_i^n is the i^{th} component in the n^{th} gravity vector measures.)

2.2 Aerodynamic Model

A 2-D aerodynamic model is used to evaluate airloads generated by lifting or control surfaces, such as wings, flaps, and elevators. The column matrix of velocity vector measures in the aerodynamic frame at the mid-chord can be expressed in terms of element variables as

$$\begin{aligned}
\bar{V}_a^n &= C_a^{n^T} \bar{V}^n - \hat{y}_{\text{mc}}^n C_a^{n^T} \bar{\Omega}^n \\
\bar{\Omega}_a^n &= C_a^{n^T} \bar{\Omega}^n
\end{aligned} \tag{24}$$

where y_{mc}^n is the column matrix of position vector measures from the beam reference axis to the control point and can be written in terms of the aerodynamic center (at the quarter chord) location as $y_{\text{mc}}^n = [0 \quad \bar{y}_{\text{ac}}^n - \frac{b^n}{2} \quad 0]^T$.

The lift, drag and pitching moment at the quarter-chord are given by:

$$\begin{aligned}
L_{\text{aero}}^n &= \rho b^n V_T^{n^2} \left(C_{l_0}^n + C_{l_\alpha}^n \alpha^n + C_{l_\beta}^n \beta^n \right) + \rho b^n V_T^n V_{a_2}^n C_{l_\alpha}^n \alpha_{\text{rot}}^n \cos \alpha^n \\
D_{\text{aero}}^n &= \rho b^n V_T^{n^2} \left(C_{d_0}^n + C_{d_{\alpha^2}}^n \alpha^{n^2} + C_{d_{\beta^2}}^n \beta^{n^2} \right) + \rho b^n V_T^n V_{a_2}^n C_{l_\alpha}^n \alpha_{\text{rot}}^n \sin \alpha^n \\
M_{\text{aero}}^n &= 2\rho b^{n^2} V_T^{n^2} \left(C_{m_0}^n + C_{m_\alpha}^n \alpha^n + C_{m_\beta}^n \beta^n \right) - \rho b^{n^2} V_T^n V_{a_2}^n C_{l_\alpha}^n \alpha_{\text{rot}}^n / 2 - \rho b^{n^3} V_{a_2}^n \Omega_{a_1}^n C_{\text{pitch}}^n
\end{aligned} \tag{25}$$

where

$$V_T^n = \sqrt{V_{a_2}^{n^2} + V_{a_3}^{n^2}} \tag{26}$$

$$\alpha^n \approx \sin \alpha^n = \frac{-V_{a_3}^n}{V_T^n} \tag{27}$$

$$\alpha_{\text{rot}}^n = \frac{\Omega_{a_1}^n b^n / 2}{V_T^n} \tag{28}$$

and $V_{a_2}^n$ and $V_{a_3}^n$ are the corresponding column matrix component of \bar{V}_a^n in the aerodynamic frame. β^n is the flap deflection of the n^{th} element of the wing. For the horizontal tail, the terms associated with β^n are replaced by γ^n which is the elevator deflection of the n^{th} element of the horizontal tail.

The lift, drag and pitching moment of Eqs. (25) are now resolved into aerodynamic frame into,

$$\begin{aligned}
f_a^n &= \begin{pmatrix} 0 \\ -L_{\text{aero}}^n \frac{V_{a_3}^n}{V_T^n} - D_{\text{aero}}^n \frac{V_{a_2}^n}{V_T^n} \\ L_{\text{aero}}^n \frac{V_{a_2}^n}{V_T^n} - D_{\text{aero}}^n \frac{V_{a_3}^n}{V_T^n} \end{pmatrix} \\
&= \rho b^n \begin{pmatrix} 0 \\ -(C_{l_0}^n + C_{l_\beta}^n \beta^n) V_T^n V_{a_3}^n + C_{l_\alpha}^n V_{a_3}^{n^2} - (C_{d_0}^n + C_{d_{\beta^2}}^n \beta^{n^2}) V_T^n V_{a_2}^n - C_{d_{\alpha^2}}^n \frac{V_{a_3}^{n^2} V_{a_2}^n}{V_T^n} \\ ((C_{l_0}^n + C_{l_\beta}^n \beta^n) V_T^n V_{a_2}^n - C_{l_\alpha}^n V_{a_2}^n (V_{a_3}^n - \Omega_{a_1}^n b^n / 2) - (C_{d_0}^n + C_{d_{\beta^2}}^n \beta^{n^2}) V_T^n V_{a_3}^n - C_{d_{\alpha^2}}^n \frac{V_{a_3}^{n^3}}{V_T^n}) \end{pmatrix}
\end{aligned} \tag{29}$$

$$\begin{aligned}
m_a^n &= \begin{Bmatrix} M_{\text{aero}}^n \\ 0 \\ 0 \end{Bmatrix} \\
&= 2\rho b^{n^2} \begin{Bmatrix} (C_{m_0}^n + C_{m_\beta}^n \beta^n) V_T^{n^2} - C_{m_\alpha}^n V_T^n V_{a_3}^n - b(C_{l_\alpha}^n/8 + C_{\text{pitch}}^n/2) V_{a_2}^n \Omega_{a_1}^n \\ 0 \\ 0 \end{Bmatrix} \quad (30)
\end{aligned}$$

The column matrices of force and moment measures in the aerodynamic frame are transformed into the beam reference frame to be added as aerodynamic loads in the element equation, Eqs. (17). Thus,

$$\bar{f}_{\text{aero}}^n = C_a^n f_a^n \quad (31)$$

$$\bar{m}_{\text{aero}}^n = C_a^n m_a^n + C_a^n \hat{y}_{\text{ac}}^n f_a^n \quad (32)$$

For unsteady effects, the inflow and acceleration terms are also included in the previous quasi-steady 2-D aerodynamics. The aerodynamic force and moment can be written as:

$$f_a^n = \rho b^n \begin{Bmatrix} 0 \\ -(C_{l_0}^n + C_{l_\beta}^n \beta^n) V_T^n V_{a_3}^n + C_{l_\alpha}^n (V_{a_3}^n + \lambda_0^n)^2 - C_{d_0}^n V_T^n V_{a_2}^n \\ (C_{l_0}^n + C_{l_\beta}^n \beta^n) V_T^n V_{a_2}^n - C_{l_\alpha}^n \dot{V}_{a_3} b/2 - C_{l_\alpha}^n V_{a_2}^n (V_{a_3}^n + \lambda_0^n - \Omega_{a_1}^n b^n/2) - C_{d_0}^n V_T^n V_{a_3}^n \end{Bmatrix} \quad (33)$$

$$m_a^n = 2\rho b^{n^2} \begin{Bmatrix} (C_{m_0}^n + C_{m_\beta}^n \beta^n) V_T^{n^2} - C_{m_\alpha}^n V_T^n V_{a_3}^n - b^n \left(\frac{C_{l_\alpha}^n}{8} + \frac{C_{\text{pitch}}^n}{2} \right) V_{a_2}^n \Omega_{a_1}^n - C_{l_\alpha}^n \left(\frac{b^{n^2}}{32} \dot{\Omega}_{a_1}^n - \frac{b^n}{8} \dot{V}_{a_3}^n \right) \\ 0 \\ 0 \end{Bmatrix} \quad (34)$$

The inflow model of Peters et al. from Ref. [45] are

$$\begin{aligned} [A_{\text{inflow}}]\{\dot{\lambda}^n\} + \left(\frac{V_T^n}{b^n}\right)\{\lambda^n\} &= \left(-\dot{V}_{a_3}^n + \frac{b^n}{2}\dot{\Omega}_{a_1}^n\right)\{c_{\text{inflow}}\} \\ \lambda_0^n &= \frac{1}{2}\{b_{\text{inflow}}\}^T\{\lambda^n\} \end{aligned} \quad (35)$$

where λ^n is a column matrix of inflow states for the n^{th} element and $[A_{\text{inflow}}]$, $\{b_{\text{inflow}}\}$, and $\{c_{\text{inflow}}\}$ are constant matrices given as

$$\begin{aligned} [A_{\text{inflow}}] &= [D_{\text{inflow}} + d_{\text{inflow}}b_{\text{inflow}}^T + c_{\text{inflow}}d_{\text{inflow}}^T + \frac{1}{2}c_{\text{inflow}}b_{\text{inflow}}^T] \\ b_{\text{inflow}_n} &= (-1)^{n-1} \frac{(N+n)!}{(N-n)!} \frac{1}{(n!)^2} \\ c_{\text{inflow}_n} &= \frac{2}{n} \\ d_{\text{inflow}_n} &= \frac{1}{2} \quad (n \neq 1) \\ d_{\text{inflow}_n} &= 0 \quad (n = 1) \\ D_{\text{inflow}_{nm}} &= \frac{1}{2}n \quad (n = m+1) \\ D_{\text{inflow}_{nm}} &= -\frac{1}{2}n \quad (n = m-1) \\ D_{\text{inflow}_{nm}} &= 0 \quad (n \neq m \pm 1) \end{aligned} \quad (36)$$

2.3 Post-processing

The governing equations are free of displacement and rotational variables. The following equations relate the strains and curvature, and displacement and rotation matrix between the undeformed and deformed configuration to recover the deformed configuration:

$$\begin{aligned} r_i' &= C^{ib}e_1 \\ C^{bi'} &= -\tilde{k}C^{bi} \\ (r_i + u_i)' &= C^{iB}(\gamma + e_1) \\ C^{Bi'} &= -(\tilde{\kappa} + \tilde{k})C^{Bi} \end{aligned} \quad (37)$$

where r_i is the column matrix of position vector measures to the beam reference line from origin, C^{bi} is the rotation matrix of beam reference frame in undeformed configuration, u_i is the column matrix of displacement vector, and C^{Bi} is the rotation matrix of the beam cross-sectional reference frame in the deformed configuration.

The 1st equation in Eqs. (37) is used to recover the beam reference line in the undeformed configuration. The 2nd equation relates the orientation of beam reference frame along the beam reference line in the undeformed configuration. If the force and moment strain measures (γ and κ) are known from the solution with given initial twist and curvature (k), then the 3rd equation shows how the beam reference line is deformed and 4th equation provides the beam reference frame in deformed configuration.

The discretized equations of Eqs. (37) are

$$\begin{aligned}
r_i^{n+1} &= r_i^n + \overline{C}^{ib^n} e_1 dl \\
\widehat{C}^{bi^{n+1}} &= \left(\frac{\Delta}{dl} + \frac{\widetilde{k}^n}{2} \right)^{-1} \left(\frac{\Delta}{dl} - \frac{\widetilde{k}^n}{2} \right) \widehat{C}^{bi^n} \\
r_i^{n+1} + u_i^{n+1} &= r_i^n + u_i^n + \overline{C}^{iB^n} (\widetilde{\gamma}^n + e_1) dl \\
\widehat{C}^{Bi^{n+1}} &= \left(\frac{\Delta}{dl} + \frac{\widetilde{\kappa}^n + \widetilde{k}^n}{2} \right)^{-1} \left(\frac{\Delta}{dl} - \frac{\widetilde{\kappa}^n + \widetilde{k}^n}{2} \right) \widehat{C}^{Bi^n}
\end{aligned} \tag{38}$$

CHAPTER III

ANALYSIS

3.1 Multiple Beam Formulation

3.1.1 Structural Analysis

Conventional aircraft can be modeled as a multiple beam structure. For a multiple beam configuration, the intrinsic beam formulation needs to be extended to model fuselage, horizontal and vertical tails, and other structures as additional beam elements of conventional aircraft.

Here's a brief description on how it extends to multiple beam configurations. If two beams are connected to each other as shown in Figure 1, they will share a node. This yields following relation on the the virtual displacement and rotational variables in both beams:

$$\begin{aligned}\overline{\delta u}_{\text{beam } 1} &= C^{B_1 B_2} \overline{\delta u}_{\text{beam } 2} \\ \overline{\delta \psi}_{\text{beam } 1} &= C^{B_1 B_2} \overline{\delta \psi}_{\text{beam } 2}\end{aligned}\tag{39}$$

where $C^{B_1 B_2}$ is the rotation matrix from B_2 (reference frame of beam 2) to B_1 (reference frame of beam 1).

The nodal equations associated with the virtual displacement and rotations at the common node will be summed up as one set of nodal equations. As separate beams, the nodal

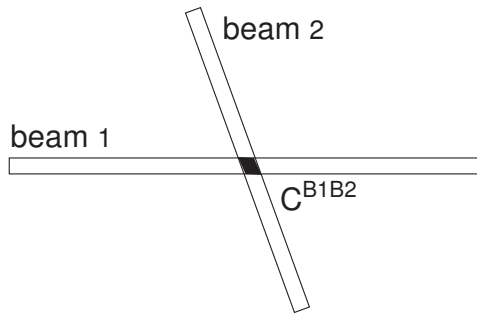


Figure 1: Schematic of two beam configuration

equations in beam 1 are

$$\begin{aligned}\widehat{F}_r^n - \widehat{C}_{lr}^{nT} \widehat{F}_l^n + \widehat{\mu}^n \widehat{g}_r^n + \widehat{f}_{\text{aero}}^n - \dot{\widehat{P}}_r^n - \widetilde{\widehat{\Omega}}_r^n \widehat{P}_r^n &= 0 \\ \widehat{M}_r^n - \widehat{C}_{lr}^{mT} \widehat{M}_l^n + \widehat{m}_T^n + \widehat{\mu}^n \widetilde{\widehat{\xi}}^n \widehat{g}_r^n + \widehat{m}_{\text{aero}}^n - \dot{\widehat{H}}_r^n - \widetilde{\widehat{\Omega}}_r^n \widehat{H}_r^n - \widetilde{\widehat{V}}_r^n \widehat{P}_r^n &= 0\end{aligned}\quad (40)$$

For beam 2, they are

$$\begin{aligned}\widehat{F}_b^m - \widehat{C}_{fb}^{mT} \widehat{F}_f^m + \widehat{\mu}^m \widehat{g}_b^m + \widehat{f}_{\text{aero}}^m - \dot{\widehat{P}}_b^m - \widetilde{\widehat{\Omega}}_b^m \widehat{P}_b^m &= 0 \\ \widehat{M}_b^m - \widehat{C}_{fb}^{mT} \widehat{M}_f^m + \widehat{m}_T^m + \widehat{\mu}^m \widetilde{\widehat{\xi}}^m \widehat{g}_b^m + \widehat{m}_{\text{aero}}^m - \dot{\widehat{H}}_b^m - \widetilde{\widehat{\Omega}}_b^m \widehat{H}_b^m - \widetilde{\widehat{V}}_b^m \widehat{P}_b^m &= 0\end{aligned}\quad (41)$$

If two beams are connected to each other, this will reduce the separate nodal equation as follows

$$\begin{aligned}\widehat{F}_r^n - \widehat{C}_{lr}^{nT} \widehat{F}_l^n + \widehat{\mu}^n \widehat{g}_r^n + \widehat{f}_{\text{aero}}^n - \dot{\widehat{P}}_r^n - \widetilde{\widehat{\Omega}}_r^n \widehat{P}_r^n + C^{B_1 B_2} (\widehat{F}_b^m - \widehat{C}_{fb}^{mT} \widehat{F}_f^m) &= 0 \\ \widehat{M}_r^n - \widehat{C}_{lr}^{mT} \widehat{M}_l^n + \widehat{\mu}^n \widetilde{\widehat{\xi}}^n \widehat{g}_r^n + \widehat{m}_{\text{aero}}^n - \dot{\widehat{H}}_r^n - \widetilde{\widehat{\Omega}}_r^n \widehat{H}_r^n - \widetilde{\widehat{V}}_r^n \widehat{P}_r^n + C^{B_1 B_2} (\widehat{M}_b^m - \widehat{C}_{fb}^{mT} \widehat{M}_f^m) &= 0\end{aligned}\quad (42)$$

Several terms such as $\widehat{\mu}^m \widehat{g}_b^m$, $\widehat{f}_{\text{aero}}^m$, \widehat{P}_b^m , \widehat{m}_T^m , $\widehat{\mu}^m \widetilde{\widehat{\xi}}^m \widehat{g}_b^m$, $\widehat{m}_{\text{aero}}^m$, \widehat{H}_b^m in beam 2 are dropped from the separate nodal equation because those are redundantly evaluated at the common node by taking the beam 1 as main one. (The beam 2 is a subordinate beam.) So it counts as only one set of governing equations (losing six nodal equations). But the lost six equations are compensated by the continuity conditions

$$\begin{aligned}\widehat{V}_{\text{beam } 1} &= C^{B_1 B_2} \widehat{V}_{\text{beam } 2} \\ \widehat{\Omega}_{\text{beam } 1} &= C^{B_1 B_2} \widehat{\Omega}_{\text{beam } 2}\end{aligned}\quad (43)$$

Additionally, the boundary condition for the gravity vector in the previous beam formulation at the reference node for beam₂ is substituted by

$$\widehat{g}_{\text{beam } 1} = C^{B_1 B_2} \widehat{g}_{\text{beam } 2} \quad (44)$$

3.1.2 Fuselage Aerodynamics

If the multiple beam formulation is applied to the analysis of conventional aircraft, it needs an additional aerodynamic model for the fuselage. The aerodynamic models follows the

evaluation of Ref. [13], so that

$$\begin{aligned} f_{\text{lift}}^n &= \rho \bar{V}_{\perp}^n |\bar{V}_{//}^n| 2\pi R \frac{dR}{ds} \\ f_{\text{drag}}^n &= \frac{1}{2} \rho |\bar{V}^n| \bar{V}^n 2R c_{\text{df}} + \frac{1}{2} \rho |\bar{V}_{\perp}^n| \bar{V}_{\perp}^n 2R c_{\text{dp}} \end{aligned} \quad (45)$$

where s is the unit vector along the fuselage reference line, $\bar{V}_{//}^n = (\bar{V}^{n^T} s)s$ is the column matrix of velocity vector along s , $\bar{V}_{\perp}^n = \bar{V}^n - (\bar{V}_{//}^n s)$ is the column matrix of velocity vector perpendicular to s , and R is the fuselage radius. The c_{df} is comparable to the skin friction coefficient c_f and c_{dp} is the drag coefficient of a circular cylinder. Eqs. (17) for an element of the fuselage will now include the fuselage aerodynamic loads instead of wing aerodynamic loads.

3.2 Modeling of Ground Vibration Testing

A GVT modeling procedure for highly flexible aircraft is developed to study the vibration characteristics. The modeling procedure uses the intrinsic beam formulation [22, 23] because such a flexible aircraft undergoing large deflection requires a geometrically-nonlinear structural model. A newly developed bungee formulation for modeling of GVT is incorporated into the analysis and ultimately into NATASHA.

The GVT analysis provides a variety of helpful information before performing any experimental GVT. First, it indicates how GVT rigid-body modes are coupled to the lowest elastic modes. Second, it can help in choosing GVT parameters (such as the stiffness and location of bungees, shaker location, and boundary conditions due to bungees) so that the GVT rigid-body modes are separated enough not to affect the lowest elastic mode, so that GVT leads to a better estimate of modal characteristics (eigenmode, natural frequency and structural damping). Otherwise, the GVT rigid-body modes will affect and disturb the modal frequencies dominated by structural deformation for free-free boundary conditions. Finally, the analysis will enable tailoring of the shape of the aircraft in the GVT configuration so that it closely mimics that of the actual flying aircraft.

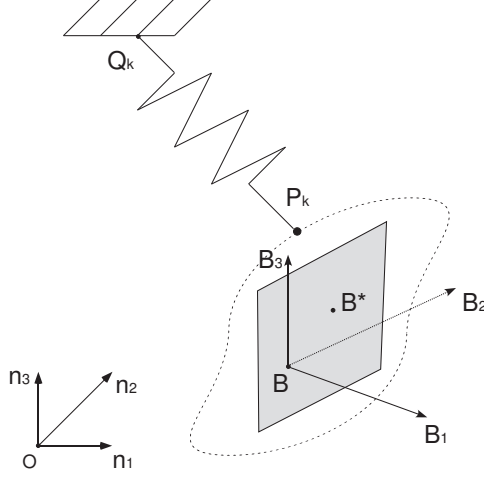


Figure 2: Schematic of bungee connection to a node

3.2.1 Bungee Formulation

The bungee formulation is developed as a separate procedure from the intrinsic beam formulation. For a simple model, a rigid body restrained by bungee cords is taken for the formulation. Consider a node attached to a support Q_k by a bungee cord modeled here as a light, either nonlinear spring modeled from Hencky (i.e. logarithmic) strain energy analysis [3, 10] or linear spring; compression is not allowed, so only the condition of a taut cord is modeled. Figure 2 shows the schematic of a bungee cord connected to a node. The point O is the origin of the inertial frame and \mathbf{n}_i is an inertial frame basis unit vector. The point B^* is the center of mass of the rigid body, and the point B is the origin of the reference frame with the unit basis vector \mathbf{B}_i .

The point P_k is taken to be the k^{th} point in a rigid body attached to a bungee cord, and the position vector from Q_k to P_k is written as

$$\mathbf{P}_{Q_k P_k} = (\ell_k + \sigma_k - \epsilon_k^2) \boldsymbol{\tau}_k \quad (46)$$

where ℓ_k is the natural length of the bungee cord and $\boldsymbol{\tau}_k$ is a unit vector along the taut cord. The deflection in the k^{th} spring is σ_k and k is the index for each bungee support; ϵ_k is the slack variable.

3.2.1.1 Static Formulation

The governing equations to determine the static equilibrium of a rigid body attached by N number of bungee cords will be derived by the augmented Lagrangian method. In a static formulation, a total potential energy is composed of three parts: elastic deformation in the bungee cords, gravity, and the geometric constraints:

$$P = \sum_{k=1}^N \frac{1}{2} K_k \left[\ln\left(1 + \frac{\sigma_k}{\ell_k}\right) \right]^2 + m g \mathbf{n}_3 \cdot \mathbf{P}_{OB^*} - \sum_{k=1}^N F_k C_{k1} + \sum_{k=1}^N \mu_k C_{k2} \quad (47)$$

where the logarithmic term is the Hencky strain energy analysis [3, 10].

$$\begin{aligned} C_{k1} &= \ell_k + \sigma_k - \epsilon_k^2 + \boldsymbol{\tau}_k \cdot (\mathbf{P}_{OQ_k} - \mathbf{P}_{OB} - \mathbf{P}_{BP_k}) \\ C_{k2} &= \boldsymbol{\tau}_k \cdot \boldsymbol{\tau}_k - 1 \end{aligned} \quad (48)$$

where K_k is a stiffness of each bungee cord, m is the mass of the rigid body, and g is the universal constant of gravity. F_k and μ_k are Lagrange multipliers. C_{k1} is the geometric constraint and C_{k2} is the constraint to enforce a unit vector. The $+/-$ sign for the augmented potential is chosen arbitrarily. For a linear spring, the potential energy can be modeled as $\sum_{k=1}^N \frac{1}{2} K_k \sigma_k^2$ instead of $\sum_{k=1}^N \frac{1}{2} K_k \left[\ln\left(1 + \frac{\sigma_k}{\ell_k}\right) \right]^2$ in the logarithmic description of Hencky strain energy analysis.

In matrix notation, it can be written as

$$\begin{aligned} P &= \sum_{k=1}^N \frac{1}{2} K_k \left[\ln\left(1 + \frac{\sigma_k}{\ell_k}\right) \right]^2 + m g n_3^T p_{OB^*} - \sum_{k=1}^N F_k C_{k1} + \sum_{k=1}^N \mu_k C_{k2} \\ &= \sum_{k=1}^N \frac{1}{2} K_k \left[\ln\left(1 + \frac{\sigma_k}{\ell_k}\right) \right]^2 + m g n_3^T (p_{OB} - C^T \xi_B) - \sum_{k=1}^N F_k C_{k1} + \sum_{k=1}^N \mu_k C_{k2} \end{aligned} \quad (49)$$

where $p_{OB^*i} = \mathbf{P}_{OB^*} \cdot \mathbf{n}_i$, $\tau_{kn_i} = \boldsymbol{\tau}_k \cdot \mathbf{n}_i$, $p_{OQ_ki} = \mathbf{P}_{OQ_k} \cdot \mathbf{n}_i$, $p_{B^*P_{ki}} = \mathbf{P}_{B^*P_k} \cdot \mathbf{B}_i$, $p_{OB_i} = \mathbf{P}_{OB} \cdot \mathbf{n}_i$, $p_{BP_{ki}} = \mathbf{P}_{BP_k} \cdot \mathbf{B}_i$, $\xi_{B_i} = \mathbf{P}_{B^*B} \cdot \mathbf{B}_i$, and $n_3 = [0 \ 0 \ 1]^T$.

Taking variations of the total potential P with respect to each variable (p_{OB} , C , σ_k ,

$\tau_{k_n}, \epsilon_k, F_k, \mu_k$), one obtains

$$\begin{aligned}
\delta P &= \sum_{k=1}^N K_k \frac{\ln(1 + \frac{\sigma_k}{\ell_k})}{1 + \frac{\sigma_k}{\ell_k}} \delta \sigma_k + m g n_3^T [\delta p_{OB} - \delta(C^T) \xi_B] \\
&\quad - \sum_{k=1}^N \delta F_k [\ell_k + \sigma_k - \epsilon_k^2 + \tau_{k_n}^T (p_{OQ_k} - p_{OB} - C^T p_{BP_k})] \\
&\quad - \sum_{k=1}^N F_k [\delta \sigma_k - 2\epsilon_k \delta \epsilon_k + \delta \tau_{k_n}^T (p_{OQ_k} - p_{OB} - C^T p_{BP_k}) + \tau_{k_n}^T (-\delta p_{OB} - \delta(C^T) p_{BP_k})] \\
&\quad + \sum_{k=1}^N \delta \mu_k (\tau_{k_n}^T \tau_{k_n} - 1) + \sum_{k=1}^N \mu_k (2\tau_{k_n}^T \delta \tau_{k_n}) \\
&= \overline{\delta q_B}^T (\sum_{k=1}^N F_k \tau_{k_B} + m g C n_3) + \overline{\delta \psi_B}^T [-\widetilde{p_{BP_k}}(F_k \tau_{k_B}) + \widetilde{\xi_B} m g C n_3] + \sum_{k=1}^N \delta \sigma_k \left[K_k \frac{\ln(1 + \frac{\sigma_k}{\ell_k})}{1 + \frac{\sigma_k}{\ell_k}} - F_k \right] \\
&\quad + \sum_{k=1}^N \delta \tau_{k_n}^T [-F_k (p_{OQ_k} - p_{OB} - C^T p_{BP_k}) + 2\mu_k \tau_{k_n}] + \delta \epsilon_k (F_k \epsilon_k) \\
&\quad + \sum_{k=1}^N \delta F_k [\ell_k + \sigma_k - \epsilon_k^2 + \tau_{k_n}^T (p_{OQ_k} - p_{OB} - C^T p_{BP_k})] + \sum_{k=1}^N \delta \mu_k (\tau_{k_n}^T \tau_{k_n} - 1)
\end{aligned} \tag{50}$$

where $\tau_{k_B i} = \boldsymbol{\tau}_k \cdot \mathbf{B}_i$, $\tau_{k_n i} = \boldsymbol{\tau}_k \cdot \mathbf{n}_i$, and $n_3 = [0 \ 0 \ 1]^T$. The detailed manipulations of virtual displacement and rotation are as follows:

$$\begin{aligned}
\tau_{k_n}^T (\delta p_{OB}) &= \tau_{k_n}^T (C^T \overline{\delta q_B}) = (C \tau_{k_n})^T \overline{\delta q_B} = \tau_{k_B}^T \overline{\delta q_B} \\
\tau_{k_n}^T \delta(C^T) p_{BP_k} &= \tau_{k_n}^T C^T C (\delta C)^T p_{BP_k} = \tau_{k_n}^T (\delta C C^T)^T p_{BP_k} = \tau_{k_B}^T (-\widetilde{\delta \psi_B})^T p_{BP_k} \\
&= \tau_{k_B}^T \widetilde{\delta \psi_B} p_{BP_k} = -\overline{\delta \psi_B}^T (\widetilde{p_{BP_k}} \tau_{k_B})
\end{aligned} \tag{51}$$

In Eq. (50), the terms in parenthesis which are associated with each virtual variation should be zero. So one obtains the following for the force and moment equilibrium:

$$\begin{aligned}
\sum_{k=1}^N F_k \tau_{k_B} + m g C n_3 &= 0 \\
\sum_{k=1}^N \widetilde{p_{BP_k}} (F_k \tau_{k_B}) - \widetilde{\xi_B} m g C n_3 &= 0
\end{aligned} \tag{52}$$

where $p_{BP_k i} = \mathbf{P}_{BP_k} \cdot \mathbf{B}_i$, $\tau_{k_B} = \boldsymbol{\tau}_k \cdot \mathbf{B}_i$. Additionally, six conditions from $C^T C = \Delta$ are required to determine the orientation of the rigid body because no parametrization of rotation is introduced and C has three degree-of-freedom.

The bungee formulation is, for $k = 1, 2, \dots, N$

$$\begin{aligned}
K_k \frac{\ln(1 + \frac{\sigma_k}{\ell_k})}{1 + \frac{\sigma_k}{\ell_k}} - F_k &= 0 \\
-F_k(p_{OQ_k} - p_{OB^*} - C^T p_{B^*P_k}) + 2\mu_k \tau_{k_n} &= 0 \\
\epsilon_k F_k &= 0 \\
\ell_k + \sigma_k - \epsilon_k^2 + \tau_{k_n}^T (p_{OQ_k} - p_{OB^*} - C^T p_{B^*P_k}) &= 0 \\
\tau_{k_n}^T \tau_{k_n} - 1 &= 0 \\
\sigma_k - \zeta_k^2 &= 0
\end{aligned} \tag{53}$$

In Eq. (53), the 3rd, 4th and 6th equations are related to the slack conditions. The 6th equation is additional equation for the slack condition of bungee cords. When a simple spring model is needed, the 3rd and 6th equations and slack variable (ϵ_k) can be eliminated from the bungee formulation. Comparing with the resulting governing equations in previous works [35, 51], the one derived in the present analysis section has a much simpler compact matrix form to avoid unnecessarily long algebraic geometric relations and thereby easing numerical computations.

The static equilibrium is determined by Newton-Raphson method. The Jacobian matrix in Newton-Raphson method becomes singular if given parameters make any of the bungee cords slack, for example, when the natural length of a bungee cord is much longer than the elongation of other bungee cords. This can be solved by eliminating the corresponding slack bungee cord from the whole system while checking whether the solution satisfies all the given set of equations. Moreover, the converged solution can be simply justified by comparing the solution with the one for the system without the slack bungee cord.

3.2.1.2 Dynamic Formulation

For the dynamic formulation, kinetic energy is added to the previous static formulation. Kinetic energy of the system can be written as

$$K = \frac{1}{2} m \mathbf{v}^{B^*I} \cdot \mathbf{v}^{B^*I} - m \boldsymbol{\Omega} \cdot (\mathbf{v}^{B^*I} \times \boldsymbol{\xi}) + \frac{1}{2} \boldsymbol{\Omega} \cdot \mathbf{I} \cdot \boldsymbol{\Omega} \tag{54}$$

where \mathbf{v}^{B^*I} is the inertial velocity of the B^* (center of mass), \mathbf{I} is the inertia dyadic of the rigid body, $\boldsymbol{\Omega}$ is the inertial angular velocity of the rigid body, and $\boldsymbol{\xi}$ is the position vector

of center of mass relative to the beam reference line in the B basis. In matrix notation

$$K = \frac{1}{2}mV_B^T V_B - m\Omega_B^T \tilde{V}_B \xi_B + \frac{1}{2}\Omega_B^T I_B \Omega_B \quad (55)$$

where $V_{B_i} = \mathbf{v}^{B^*I} \cdot \mathbf{B}_i$ and $\Omega_{B_i} = \boldsymbol{\Omega} \cdot \mathbf{B}_i$.

As in the static formulation, the potential energy can be expressed as

$$P = \sum_{k=1}^N \frac{1}{2} K_k \left[\ln\left(1 + \frac{\sigma_k}{\ell_k}\right) \right]^2 + mg\mathbf{n}_3 \cdot \mathbf{P}_{OB^*} \quad (56)$$

So the total potential energy with augmented potentials of the constraints is

$$P^* = P - \sum_{k=1}^N F_k C_{k_1} + \sum_{k=1}^N \mu_k C_{k_2} \quad (57)$$

with

$$\begin{aligned} C_{k_1} &= \ell_k + \sigma_k - \epsilon_k^2 + \tau_{k_n}^T (p_{OQ_k} - p_{OB} - C^T p_{BP_k}) \\ C_{k_2} &= \tau_{k_n}^T \tau_{k_n} - 1 \end{aligned} \quad (58)$$

Hamilton's extended principle is

$$\int_{t_i}^{t_f} (\delta K - \delta P^* + \overline{\delta W}) dt = \overline{\delta A} \quad (59)$$

where $\overline{\delta W}$ is the virtual work of applied load and $\overline{\delta A}$ is the virtual action at end of the time interval. For simplicity, $\overline{\delta A}$ can be discarded for applications of Hamilton's principle (Ref. [22] describes the details for handling $\overline{\delta W}$ and $\overline{\delta A}$). Thus,

$$\int_{t_i}^{t_f} (\delta K - \delta P^*) dt = 0 \quad (60)$$

First,

$$\begin{aligned} \int_{t_i}^{t_f} \delta K dt &= \int_{t_i}^{t_f} [\delta V_B^T (mV_B) + \delta \Omega_B^T (I_B \Omega_B)] dt \\ &= \int_{t_i}^{t_f} [(\dot{\overline{\delta q}}_B + \tilde{\Omega}_B \overline{\delta q}_B + \tilde{V}_B \overline{\delta \psi})^T (P_B) + (\dot{\overline{\delta \psi}}_B + \tilde{\Omega}_B \overline{\delta \psi})^T (H_B)] dt \\ &= \int_{t_i}^{t_f} \left\{ \overline{\delta q}_B^T [-\dot{P}_B - \tilde{\Omega}_B P_B] + \overline{\delta \psi}_B^T (-\dot{H}_B - \tilde{\Omega}_B H_B - \tilde{V}_B P_B) \right\} dt \end{aligned} \quad (61)$$

where $P_B = m(V_B - \tilde{\xi}_B \Omega_B)$ is a column matrix of linear momentum and $H_B = I_B \Omega_B + m\tilde{\xi}_B V_B$ is a column matrix of angular momentum, so that

$$\int_{t_i}^{t_f} \delta P^* dt = \int_{t_i}^{t_f} \left[\delta P - \sum_{k=1}^N (\delta F_k C_{k_1} + F_k \delta C_{k_1}) + \sum_{k=1}^N (\delta \mu_k C_{k_2} + \mu_k \delta C_{k_2}) \right] dt \quad (62)$$

The Euler-Lagrange equations in matrix notation are

$$\begin{aligned}\dot{P}_B + \widetilde{\Omega}_B P_B + \sum_{k=1}^N F_k \tau_{k_B} + mgn_{3_B} &= 0 \\ \dot{H}_B + \widetilde{\Omega}_B H_B + \widetilde{V}_B P_B + \sum_{k=1}^N \widetilde{p_{BP_k}}(F_k \tau_{k_B}) - \widetilde{\xi}_B mgCn_3 &= 0\end{aligned}\tag{63}$$

Additional kinematic relations are

$$V_B = \dot{p}_{OB} + \widetilde{\Omega}_B p_{OB}\tag{64}$$

and

$$\widetilde{\Omega}_B = -\dot{C}C^T\tag{65}$$

The bungee formulation for $k = 1, 2, \dots, N$ is the same as the one derived for the static case, namely

$$\begin{aligned}K_k \frac{\ln(1 + \frac{\sigma_k}{\ell_k})}{1 + \frac{\sigma_k}{\ell_k}} - F_k &= 0 \\ -F_k(p_{OQ_k} - p_{OB} - C^T p_{BP_k}) + 2\mu_k \tau_{k_n} &= 0 \\ \epsilon_k F_k &= 0 \\ \ell_k + \sigma_k - \epsilon_k^2 + \tau_{k_n}^T(p_{OQ_k} - p_{OB} - C^T p_{BP_k}) &= 0 \\ \tau_{k_n}^T \tau_{k_n} - 1 &= 0 \\ \sigma_k - \zeta_k^2 &= 0\end{aligned}\tag{66}$$

3.2.1.3 Linearization for Eigenanalysis

For eigenanalysis, the set of governing equations derived in the previous section is linearized about a static equilibrium

$$X = \overline{X} + \widehat{X}(t)\tag{67}$$

where X is each state, \overline{X} is a value of each state at a static equilibrium, and \widehat{X} is a small perturbation on each state.

So a small perturbation on each variable can be expressed as

$$\begin{aligned}
p_{OB^*} &= \bar{p}_{OB^*} + \hat{u} \\
V_B &= \bar{V}_B + \hat{V}_B = \hat{V}_B \\
C &= \bar{C} + \hat{C} = (\Delta - \tilde{\theta})\bar{C} \\
\Omega &= \bar{\Omega} + \hat{\Omega} = \hat{\Omega} \\
F_k &= \bar{F}_k + \hat{F}_k \\
\tau_{k_n} &= \bar{\tau}_{k_n} + \hat{\tau}_{k_n} \\
\sigma_k &= \bar{\sigma}_k + \hat{\sigma}_k \\
\mu_k &= \bar{\mu}_k + \hat{\mu}_k \\
\epsilon_k &= \bar{\epsilon}_k + \hat{\epsilon}_k \\
\zeta_k &= \bar{\zeta}_k + \hat{\zeta}_k
\end{aligned} \tag{68}$$

Each linearized equation is

$$\begin{aligned}
\dot{\hat{P}}_B + \sum_{k=1}^N (\bar{F}_k \hat{\tau}_k + \bar{\tau}_k \hat{F}_k) - mg \tilde{\theta} \bar{C} n_3 &= 0 \\
\dot{\hat{H}}_B + \sum_{k=1}^N \widetilde{p_{B^*P_k}} (\bar{F}_k \hat{\tau}_k + \bar{\tau}_k \hat{F}_k) &= 0 \\
\hat{V}_B &= \hat{u} + \tilde{\Omega} \bar{p}_{OB} \\
\tilde{\hat{\Omega}}_B &= \tilde{\hat{\theta}}
\end{aligned} \tag{69}$$

For each bungee support ($k = 1, 2, \dots, N$),

$$\begin{aligned}
K_k \frac{1 - \ln(1 + \frac{\bar{\sigma}_k}{\ell_k})}{(1 + \frac{\bar{\sigma}_k}{\ell_k})^2} \hat{\sigma}_k - \hat{F}_k &= 0 \\
-\hat{F}_k [\bar{C} p_{OQ_k} - \bar{p}_{OB^*} - p_{B^*P_k}] + \bar{F}_k \left[\hat{u} + \tilde{\theta} \bar{C} p_{OQ_k} \right] + 2(\bar{\mu}_k \hat{\tau}_{k_B} + \bar{\tau}_{k_B} \hat{\mu}_k) &= 0 \\
\bar{\epsilon}_k \hat{F}_k + \bar{F}_k \hat{\epsilon}_k &= 0 \\
\hat{\sigma}_k - 2\bar{\epsilon}_k \hat{\epsilon}_k - \bar{\tau}_{k_B}^T \left[\hat{u} + \tilde{\theta} \bar{C} p_{OQ_k} \right] + [\bar{C} p_{OQ_k} - \bar{p}_{OB^*} - p_{B^*P_k}]^T \hat{\tau}_{k_B} &= 0 \\
\bar{\tau}_{k_B}^T \hat{\tau}_{k_B} &= 0 \\
\hat{\sigma}_k - 2\bar{\zeta}_k \hat{\zeta}_k &= 0
\end{aligned} \tag{70}$$

These linearized equation of motion can be expressed in matrix form as $A\hat{X} = B\hat{X}$, which is a system of first-order equations:

$$\begin{aligned}
 & \left[\begin{array}{cccc|cccccc} \Delta & 0 & 0 & 0 & 0 & 0 & 0 & 0 & 0 & 0 \\ 0 & m\Delta & 0 & 0 & 0 & 0 & 0 & 0 & 0 & 0 \\ 0 & 0 & \Delta & 0 & 0 & 0 & 0 & 0 & 0 & 0 \\ 0 & 0 & 0 & I_B & 0 & 0 & 0 & 0 & 0 & 0 \\ \hline 0 & 0 & 0 & 0 & 0 & 0 & 0 & 0 & 0 & 0 \\ 0 & 0 & 0 & 0 & 0 & 0 & 0 & 0 & 0 & 0 \\ 0 & 0 & 0 & 0 & 0 & 0 & 0 & 0 & 0 & 0 \\ 0 & 0 & 0 & 0 & 0 & 0 & 0 & 0 & 0 & 0 \\ 0 & 0 & 0 & 0 & 0 & 0 & 0 & 0 & 0 & 0 \end{array} \right]_{(12+4N) \times (12+4N)} \left\{ \begin{array}{c} \dot{\hat{u}} \\ \dot{\hat{V}}_B \\ \dot{\hat{\theta}} \\ \dot{\hat{\Omega}}_B \\ \hline \dot{\hat{F}}_k \\ \dot{\hat{\tau}}_{k_B} \\ \dot{\hat{\sigma}}_k \\ \dot{\hat{\mu}}_k \\ \dot{\hat{\epsilon}}_k \\ \dot{\hat{\zeta}}_k \end{array} \right\} \\
 & = \left[\begin{array}{cccc|cccccc} 0 & \Delta & 0 & \widetilde{\bar{p}}_{OB} & 0 & 0 & 0 & 0 & 0 & 0 \\ 0 & 0 & -mg\widetilde{\bar{C}n_3} & 0 & -\bar{\tau}_{k_B} & -\bar{F}_k\Delta & 0 & 0 & 0 & 0 \\ 0 & 0 & 0 & \Delta & 0 & 0 & 0 & 0 & 0 & 0 \\ 0 & 0 & 0 & 0 & -\widetilde{\bar{p}_{B^*P_k}\bar{\tau}_{k_B}} & -\widetilde{\bar{p}_{B^*P_k}\bar{F}_k} & 0 & 0 & 0 & 0 \\ \hline 0 & 0 & 0 & 0 & -1 & 0 & K_k^* & 0 & 0 & 0 \\ \bar{F}_k\Delta & 0 & -\bar{F}_k\widetilde{\bar{p}oQ_{k_B}} & 0 & -r & 2\bar{\mu}_k\Delta & 0 & 2\bar{\tau}_{k_B} & 0 & 0 \\ 0 & 0 & 0 & 0 & \bar{\epsilon}_k & 0 & 0 & 0 & \bar{F}_k & 0 \\ -\bar{\tau}_{k_B}^T & 0 & \bar{\tau}_{k_B}^T\widetilde{\bar{p}oQ_{k_B}} & 0 & 0 & r & 1 & 0 & -2\bar{\epsilon}_k & 0 \\ 0 & 0 & 0 & 0 & 0 & \bar{\tau}_{k_B}^T & 0 & 0 & 0 & 0 \\ 0 & 0 & 0 & 0 & 0 & 0 & 1 & 0 & 0 & -2\bar{\zeta}_k \end{array} \right] \left\{ \begin{array}{c} \hat{u} \\ \hat{V}_B \\ \hat{\theta} \\ \hat{\Omega}_B \\ \hline \hat{F}_k \\ \hat{\tau}_{k_B} \\ \hat{\sigma}_k \\ \hat{\mu}_k \\ \hat{\epsilon}_k \\ \hat{\zeta}_k \end{array} \right\} \quad (71)
 \end{aligned}$$

where $r = \bar{C}p_{OQ_k} - \bar{p}_{OB^*} - p_{B^*P_k}$, $p_{OQ_{k_B}} = \bar{C}p_{OQ_k}$, $K_k^* = \frac{1 - \ln(1 + \bar{\sigma}_k/\ell_k)}{(1 + \bar{\sigma}_k/\ell_k)^2}$ for $k=1, 2, \dots, N$,

Δ is the identity matrix and

$$\begin{aligned}
 B\hat{X} &= A\lambda\hat{X} \\
 \frac{1}{\lambda}\hat{X} &= B^{-1}A\hat{X} \\
 A^*\hat{X} &= \lambda^*\hat{X}
 \end{aligned} \quad (72)$$

Thus, the system is easily be cast as a generalized eigenvalue problem, as in the first

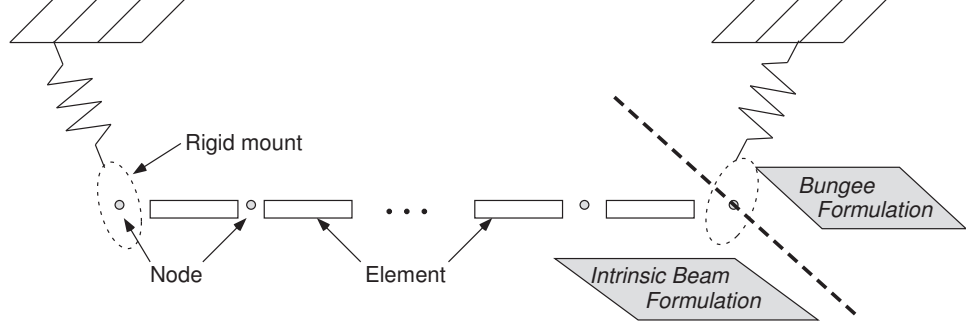


Figure 3: Schematic of incorporation bungee formulation to intrinsic beam formulation

equation, or as a standard eigenvalue problem when B^{-1} exists, as in the third.

3.2.2 Coupling of Bungee and Intrinsic Beam Formulations

The intrinsic beam and bungee formulations are developed separately. The coupling procedures follows. The schematic is shown in Figure 3. First, the Euler-Lagrange equation, Eqs. (63), of the bungee formulation is equivalent to the nodal equation in the intrinsic beam formulation after finite element discretization. The additional tension by the bungee cords (\hat{F}_k) should be included in the corresponding nodal equation of the intrinsic beam formulation if the bungee cord is attached to the node. These corrections are given in Eqs. (74). The next procedure is about how to arrange the variables which are associated with the rotation: gravity vector \hat{g}_r and rotation matrix C . At the nodes where bungee cords are attached, one can be eliminated by the other as a dummy variable. Here, however, we will keep both variables for the purpose of the computational implementation for arbitrary configurations. By this choice, some additional equations Eqs. (77) are needed to relate the rotational variables of each formulation.

However, in this incorporation procedure, the whole formulation cannot be fully intrinsic due to the geometric constraint by introducing bungee cords, which makes the system statically indeterminant. So it is inevitable that some variables for displacement and rotation are introduced at the nodes where bungee cords are attached to the beam. This information appears in the form of the strain-displacement relation Eq. (76).

3.2.2.1 Static Formulation

The element equations of the intrinsic beam formulation in finite element discretization are

$$\begin{aligned} \frac{\widehat{F}_l^{n+1} - \widehat{F}_r^n}{dl} + (\widetilde{\kappa}^n + \widetilde{k}^n) \overline{F}^n &= 0 \\ \frac{\widehat{M}_l^{n+1} - \widehat{M}_r^n}{dl} + (\widetilde{\kappa}^n + \widetilde{k}^n) \overline{M}^n + (\widetilde{e}_1 + \widetilde{\gamma}^n) \overline{F}^n &= 0 \\ \frac{\widehat{g}_l^{n+1} - \widehat{g}_r^n}{dl} + (\widetilde{\kappa}^n + \widetilde{k}^n) \overline{g}^n &= 0 \end{aligned} \quad (73)$$

where n is the index for the element of the beam.

The nodal equations will substitute the force and moment equilibrium in the bungee formulation with the correction term involving tension in the bungee cord (F_k), so that

$$\begin{aligned} \widehat{F}_r^n - \widehat{C}_{lr}^{nT} \widehat{F}_l^n + \widehat{\mu}^n \widehat{g}_r - \underline{F_k \tau_{k_B}} &= 0 \\ \widehat{M}_r^n - \widehat{C}_{lr}^{nT} \widehat{M}_l^n + \widehat{\mu}^n \widehat{\xi}^n \widehat{g}_r - \underline{\widehat{p}_{BP_k} (F_k \tau_{k_B})} &= 0 \end{aligned} \quad (74)$$

For each bungee support ($k = 1, 2, \dots$)

$$\begin{aligned} K_k \frac{\ln(1 + \frac{\sigma_k}{\ell_k})}{1 + \frac{\sigma_k}{\ell_k}} - F_k &= 0 \\ -F_k (p_{OQ_k} - p_{OB_m} - C_m^T p_{BP_k}) + 2\mu_k \tau_{k_n} &= 0 \\ \epsilon_k F_k &= 0 \\ \ell_k + \sigma_k - \epsilon_k^2 + \tau_{k_n}^T (p_{OQ_k} - p_{OB_m} - C_m^T p_{BP_k}) &= 0 \\ \tau_{k_n}^T \tau_{k_n} - 1 &= 0 \\ \sigma_k - \zeta_k^2 &= 0 \end{aligned} \quad (75)$$

To combine the two formulations, the strain-displacement relation between two nodes attached by bungee cords is needed. Thus,

$$C_{m+1}^T (p_{OB^*_{m+1}} - a e_1) = C_m^T (p_{OB^*_m} + a e_1) + \sum_{j=1}^J \overline{C}^{iB^j} (\bar{\gamma}^j + e_1) \quad (76)$$

where m is the index for the nodes attached to bungee cords, J is the total number of elements between two nodes attached to bungee cords, j is the index for the element between two nodes attached to bungee cords and a is the length of a virtual rigid bungee mount along e_1 . (The virtual rigid bungee mount is a rigid body that locates at arbitrary node where the bungee cords are attached. a can be zero.)

Additional equations to connect the two orientation variables (\hat{g}_r^n, C_m) in each scheme are as follows:

$$\begin{aligned}\hat{g}_r^m &= C_m [0 \ 0 \ -1]^T \\ \hat{C}^{Bi^{n+1}} C_{m+1}^T &= \Delta\end{aligned}\tag{77}$$

Eqs. (76) and (77) contain \bar{C}^{iB^j} and $\hat{C}^{Bi^{m+1}}$. So a secondary equation is necessary, so that

$$\begin{aligned}\bar{C}^{iB^j} &= \frac{1}{2} [\hat{C}^{iB^j} + \hat{C}^{iB^{j+1}}] \\ \hat{C}^{Bi^{n+1}} &= \left(\frac{\Delta}{dl} + \frac{\tilde{\kappa}^n + \tilde{k}^n}{2} \right)^{-1} \left(\frac{\Delta}{dl} - \frac{\tilde{\kappa}^n + \tilde{k}^n}{2} \right) \hat{C}^{Bi^n}\end{aligned}\tag{78}$$

To combine the orientation variables (\hat{g}_r^n, C_m) of each formulation, the detailed procedure follows. Let's stipulate that the 1st and 10th nodes are attached to bungee cords. (For the general case, bungees can be applied to arbitrary nodes.) By taking the 1st node as the reference node ($m = 1$), the gravity vector (\hat{g}_r) is related by the 1st equation in Eq. (77). Moreover $\hat{C}^{Bi^n} = C_m$ by definition at 1st node ($m = n = 1$). The 10th node ($n = 9, m = 2$), $\hat{C}^{Bi^{n+1}}$ can be expressed as C_m explicitly by virtue of the Eq. (78) for a straight beam without nodal kinks. In the 2nd equation of Eqs. (77) are actually six conditions. So only three more conditions are selected to relate the orientation at the 10th node to C_{m+1} . Some of these selections can make the Jacobian singular. For example, one of the possible choices is $A_{11} = 1, A_{12} = 0$, and $A_{23} = 0$ where $\hat{C}^{Bi^{m+1}} C_{m+1}^T = A_{ij}$. Generally if any other nodes are attached by a bungee cord, six equations will be added in the formulation; three equations from the strain-displacement relation, Eq. (76), and another three choices from the 2nd equation in Eq. (77) to relate the orientation of additional virtual rigid bungee mount. Finally the incorporation of procedures for the static formulation is completed with 12 boundary conditions, which are $\hat{F}_l^1 = \hat{F}_r^{N+1} = \hat{M}_l^1 = \hat{M}_r^{N+1} = 0$.

3.2.2.2 Dynamic Formulation

The procedure for the dynamic formulation is same as the static formulation except that it includes the rate of change in the linear and angular momenta in the governing equation.

The element equations of the intrinsic beam formulation are

$$\begin{aligned}
& \frac{\widehat{F}_l^{n+1} - \widehat{F}_r^n}{dl} + (\widetilde{\kappa}^n + \widetilde{k}^n)\overline{F}^n + \mu^n \overline{g}^n - \dot{\overline{P}}^n - \widetilde{\Omega}^n \overline{P}^n = 0 \\
& \frac{\widehat{M}_l^{n+1} - \widehat{M}_r^n}{dl} + (\widetilde{\kappa}^n + \widetilde{k}^n)\overline{M}^n + (\widetilde{e}_1 + \widetilde{\gamma}^n)\overline{F}^n + \mu^n \widetilde{\xi}^n \overline{g}^n - \dot{\overline{H}}^n - \widetilde{\Omega}^n \overline{H}^n - \widetilde{V}^n \overline{P}^n = 0 \\
& \frac{\widehat{V}_l^{n+1} - \widehat{V}_r^n}{dl} + (\widetilde{\kappa}^n + \widetilde{k}^n)\overline{V}^n + (\widetilde{e}_1 + \widetilde{\gamma}^n)\overline{\Omega}^n - \dot{\overline{\gamma}}^n = 0 \quad (79) \\
& \frac{\widehat{\Omega}_l^{n+1} - \widehat{\Omega}_r^n}{dl} + (\widetilde{\kappa}^n + \widetilde{k}^n)\overline{\Omega}^n - \dot{\overline{\kappa}}^n = 0 \\
& \frac{\widehat{g}_l^{n+1} - \widehat{g}_r^n}{dl} + (\widetilde{\kappa}^n + \widetilde{k}^n)\overline{g}^n = 0
\end{aligned}$$

The equations for nodes to which bungee cords are attached are corrected as follows

$$\begin{aligned}
& \widehat{F}_r^n - \widehat{C}_{lr}^{nT} \widehat{F}_l^n + \widehat{\mu}^n \widehat{g}_r^n - \dot{\widehat{P}}_r^n - \widetilde{\Omega}_r^n \widehat{P}_r^n - F_k \tau_{k_B} = 0 \\
& \widehat{M}_r^n - \widehat{C}_{lr}^{nT} \widehat{M}_l^n + \widehat{\mu}^n \widetilde{\xi}^n \widehat{g}_r^n - \dot{\widehat{H}}_r^n - \widetilde{\Omega}_r^n \widehat{H}_r^n - \widetilde{V}_r^n \widehat{P}_r^n - \widetilde{p_{BP_k}} (F_k \tau_{k_B}) - (\widetilde{ae_1}) \widehat{F}_r^n - (\widetilde{ae_1}) \widehat{F}_l^n = 0 \quad (80)
\end{aligned}$$

The variables \widehat{V}_r and $\widehat{\Omega}_r$ of the beam formulation are related to the position of the rigid body mount at a node by kinematical relations

$$\begin{aligned}
V_B &= \dot{p}_{OB} + \widetilde{\Omega}_B p_{OB} = \widehat{V}_r^{(m)} \\
\widetilde{\Omega}_B &= -\dot{C}_m C_m^T = \widetilde{\Omega}_r^{(m)} \quad (81)
\end{aligned}$$

Likewise the static formulation, the strain-displacement relation is

$$C_{m+1}^T (p_{OB^*_{m+1}} - ae_1) = C_m^T (p_{OB^*_m} + ae_1) + \sum_{j=1}^J \overline{C}^{iB^j} (\overline{\gamma}^j + e_1) dl^j \quad (82)$$

and the relations to connect the orientation are expressed as

$$\begin{aligned}
\widehat{g}_r^m &= C_m [0 \quad 0 \quad -1]^T \\
\widehat{C}^{Bi^{n+1}} C_{m+1}^T &= \Delta \quad (83)
\end{aligned}$$

For each bungee cord ($k = 1, 2, \dots$)

$$\begin{aligned}
K_k \frac{\ln(1 + \frac{\sigma_k}{\ell_k})}{1 + \frac{\sigma_k}{\ell_k}} - F_k &= 0 \\
-F_k(p_{OQ_k} - p_{OB} - C^T p_{BP_k}) + 2\mu_k \tau_{k_n} &= 0 \\
\epsilon_k F_k &= 0 \\
\ell_k + \sigma_k - \epsilon_k^2 + \tau_{k_n}^T (p_{OQ_k} - p_{OB} - C^T p_{BP_k}) &= 0 \\
\tau_{k_n}^T \tau_{k_n} - 1 &= 0 \\
\sigma_k - \zeta_k^2 &= 0
\end{aligned} \tag{84}$$

The 12 boundary conditions complete the dynamic formulation.

3.2.2.3 Linearization for Eigenanalysis

Next, procedures for eigenanalysis involving linearization of the dynamic formulation about a static equilibrium are considered. First,

$$X = X_{eq} + X^*(t) \tag{85}$$

where X is a state, X_{eq} is a value of the state at a static equilibrium, and X^* is small perturbation on the state.

The linearized element equation from the intrinsic beam formulation are

$$\begin{aligned}
\frac{\widehat{F}_l^{*n+1} - \widehat{F}_r^{*n}}{dl} + (\widetilde{\kappa}_{eq}^n + \widetilde{k}^n) \overline{F}^{*n} + \widetilde{\kappa}^{*n} \overline{F}_{eq}^n + \mu^n \overline{g}^{*n} &= \dot{\overline{P}}^{*n} \\
\frac{\widehat{M}_l^{*n+1} - \widehat{M}_r^{*n}}{dl} + (\widetilde{\kappa}_{eq}^n + \widetilde{k}^n) \overline{M}^{*n} + \widetilde{\kappa}^{*n} \overline{M}_{eq}^n + (\widetilde{e}_1 + \widetilde{\gamma}_{eq}^n) \overline{F}^{*n} + \widetilde{\gamma}^{*n} \overline{F}_{eq}^n + \mu^n \widetilde{\xi}^n \overline{g}^{*n} &= \dot{\overline{H}}^{*n} \\
\frac{\widehat{V}_l^{*n+1} - \widehat{V}_r^{*n}}{dl} + (\widetilde{\kappa}_{eq}^n + \widetilde{k}^n) \overline{V}^{*n} + (\widetilde{e}_1 + \widetilde{\gamma}_{eq}^n) \overline{\Omega}^{*n} &= \dot{\overline{\gamma}}^{*n} \\
\frac{\widehat{\Omega}_l^{*n+1} - \widehat{\Omega}_r^{*n}}{dl} + (\widetilde{\kappa}_{eq}^n + \widetilde{k}^n) \overline{\Omega}^{*n} &= \dot{\overline{\kappa}}^{*n} \\
\frac{\widehat{g}_l^{*n+1} - \widehat{g}_r^{*n}}{dl} + (\widetilde{\kappa}_{eq}^n + \widetilde{k}^n) \overline{g}^{*n} + \widetilde{\kappa}^{*n} \overline{g}_{eq}^n &= 0
\end{aligned} \tag{86}$$

The equations for the nodes to which bungee cords are attached will be corrected as follows:

$$\begin{aligned}
\widehat{F}_r^{*n} - \widehat{C}_{lr}^{nT} \widehat{F}_l^{*n} + \widehat{\mu}^n \widehat{g}_r^{*n} - \dot{\widehat{P}}_r^{*n} - F_{k_{eq}}^* \tau_{k_B}^* - F_k^* \tau_{k_{Beq}} &= 0 \\
\widehat{M}_r^{*n} - \widehat{C}_{lr}^{nT} \widehat{M}_l^{*n} + \widehat{\mu}^n \widetilde{\xi}^n \widehat{g}_r^{*n} - \dot{\widehat{H}}_r^{*n} - \widetilde{p}_{BP_k} (F_{k_{eq}}^* \tau_{k_B}^* + F_k^* \tau_{k_{Beq}}) - (\widetilde{ae}_1) (\widehat{F}_r^{*n} + \widehat{F}_l^{*n}) &= 0
\end{aligned} \tag{87}$$

The linearized kinematical relations at the nodes to which bungee cords are attached are

$$\widehat{V}_r^{*m} = \dot{u}^* + \widetilde{\Omega}_r^{*m} p_{OBeq}^m \quad (88)$$

and

$$\widetilde{\Omega}_r^{*m} = \widetilde{\theta}^{*m} \quad (89)$$

One difficulty arises in the linearization of the additional equations for GVT modeling: strain-displacement and rotational relation. It is infeasible to get an analytic expression for the linearized equation of Eq. (82), and the three choices $A_{11} = 1, A_{12} = 0, A_{23} = 0$ in 2nd equation of Eq. (83). So the one from the numerical perturbation on these equations with respect to each state is substituted for the analytic counterpart, viz.,

$$B_{(82)-(83)} \approx B_{num(82)-(83)} = \frac{F_{(82)-(83)}(X_{eq} + q) - F_{(82)-(83)}(X_{eq} - q)}{2q} \quad (90)$$

where q is a numerical perturbation and

$$F_{(82)-(83)} = \left\{ \begin{array}{c} C_{m+1}^T (p_{OB^*_{m+1}} - ae_1) - C_m^T (p_{OB^*_m} + ae_1) - \sum_{j=1}^J \overline{C}^{iB^j} (\overline{\gamma}^j + e_1) dl^j \\ A_{11} - 1 \\ A_{12} \\ A_{23} \end{array} \right\}^{6 \times 1} \quad (91)$$

$$\widehat{g}_r^{*m} = -\widetilde{\theta}^* C_{eq}^m [0 \ 0 \ -1]^T \quad (92)$$

For each bungee cord ($k = 1, 2, \dots$),

$$\begin{aligned} K_k \frac{1 - \ln(1 + \frac{\overline{\sigma}_k}{\ell_k})}{(1 + \frac{\overline{\sigma}_k}{\ell_k})^2} \widehat{\sigma}_k - \widehat{F}_k &= 0 \\ -\widehat{F}_k [\overline{C} p_{OQ_k} - \overline{p}_{OB^*} - p_{B^*P_k}] + \overline{F}_k \left[\widehat{u} + \widetilde{\theta} \overline{C} p_{OQ_k} \right] + 2(\overline{\mu}_k \widehat{\tau}_{k_B} + \overline{\tau}_{k_B} \widehat{\mu}_k) &= 0 \\ \overline{\epsilon}_k \widehat{F}_k + \overline{F}_k \widehat{\epsilon}_k &= 0 \\ \widehat{\sigma}_k - 2\overline{\epsilon}_k \widehat{\epsilon}_k - \overline{\tau}_{k_B}^T \left[\widehat{u} + \widetilde{\theta} \overline{C} p_{OQ_k} \right] + [\overline{C} p_{OQ_k} - \overline{p}_{OB^*} - p_{B^*P_k}]^T \widehat{\tau}_{k_B} &= 0 \\ \overline{\tau}_{k_B}^T \widehat{\tau}_{k_B} &= 0 \\ \widehat{\sigma}_k - 2\overline{\zeta}_k \widehat{\zeta}_k &= 0 \end{aligned} \quad (93)$$

where here \hat{X} is perturbed state and \bar{X} is equilibrium state. The 12 boundary conditions complete the system of linearized equations.

3.2.3 GVT in Multiple Beam Configuration

The GVT modeling for conventional aircrafts can also be developed by incorporating the multiple beam formulation into the GVT modeling. For example, let's take a conventional aircraft. Right and left wing tips, and the fuselage tip are attached to bungee cords for GVT analysis. For static equilibrium, Eqs. (42) and (44) are used to connect the fuselage to the wing, dropping all the dynamic terms such as $\hat{\Omega}_r^n, \hat{V}_r^n, \dot{\hat{P}}_r^n, \dot{\hat{H}}_r^n$. However, Eqs. (42) – (44) will involve the eigenanalysis after linearization. Additionally, the strain-displacement relation is used to relate the bungee cords attached to fuselage tip. One of the three bungee cords is chosen as a reference to apply the strain-displacement relation. If the bungee cord attached to left wing tip is taken as the reference one, two sets of strain-displacement are required: one from the reference one to right wing tip and another from the reference to fuselage tip.

3.3 *Engine/Propeller Modeling*

Previously NATASHA has constant thrust vectors located at arbitrary nodes to provide thrust. The main purpose of the Engine/Propeller modeling is to extend the analysis methodology to HALE aircraft which are typically propeller-driven aircrafts by incorporating an Engine/Propeller model into NATASHA adding two new two degrees of freedom, pitch and yaw angles.

Several assumptions are made for the methodology.

- The blades are rigid.
- The twist angle of the blade (Θ_{tw}) in Eq. (111) is set linear values from root to tip of the blade before the computation. Then $\Theta_{tw}(r)$ is adjusted so that the angle of attack at both root and tip are proper values which lie between -20° and 20° after the solution converges.
- The reverse flow region that can occur close to the root is ignored.
 - After the procedure converges to a trim solution, it is necessary to check how much of the region is under going reverse flow.
- The constant approximation of the propeller airloads is assumed by taking an average over one revolution divided by the number of blades.
 - The effect of periodic side forces and moments is investigated in the result section.
- For simplicity, the induced velocity is ignored, which is a higher-order effect than the perpendicular velocity component because the pylon is closely aligned to the freestream direction. “The induced inflow will, in fact, be very small for typical proprotor operation; this is due to the high inflow V ” [26].
- The blade element theory using 2-D aerodynamics is taken for propeller aerodynamics.
- Compressibility and tip loss are not considered.
- Pitch and yaw angle are small.

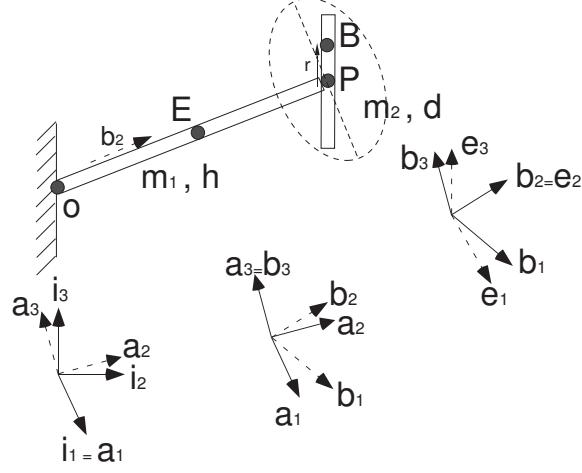


Figure 4: Schematic of simple Engine/Propeller system

3.3.1 Structural Modeling

Figure 4 shows the schematic of simple Engine/Propeller system with rigid blades. A virtual hinge is located at point O with pitch and yaw torsional springs attached to wing. The point E is the center of mass of pylon and m_1, h are total mass and length of pylon. The point P is the hub center of propeller. The point B is arbitrary point of the propeller blade with distance r from the hub center along the unit vector \mathbf{e}_3 and m_2, d are total mass and diameter of blade.

Let's first define reference frames. $\mathbf{i}_1, \mathbf{i}_2, \mathbf{i}_3$ are unit basis vectors for reference frame (\mathcal{F}_i) in a beam cross section and $\mathbf{a}_1, \mathbf{a}_2, \mathbf{a}_3$ are the unit basis vectors of the reference frame (\mathcal{F}_a) rotated from \mathcal{F}_i with α (pitch angle) of the pylon. Thus,

$$\begin{Bmatrix} \mathbf{i}_1 \\ \mathbf{i}_2 \\ \mathbf{i}_3 \end{Bmatrix} = \begin{bmatrix} 1 & 0 & 0 \\ 0 & c_\alpha & -s_\alpha \\ 0 & s_\alpha & c_\alpha \end{bmatrix} \begin{Bmatrix} \mathbf{a}_1 \\ \mathbf{a}_2 \\ \mathbf{a}_3 \end{Bmatrix} = C^{ia} \begin{Bmatrix} \mathbf{a}_1 \\ \mathbf{a}_2 \\ \mathbf{a}_3 \end{Bmatrix} \quad (94)$$

$\mathbf{b}_1, \mathbf{b}_2, \mathbf{b}_3$ are the unit basis vectors of the reference frame (\mathcal{F}_b) rotated from \mathcal{F}_a with β (yaw angle) of the pylon. Therefore,

$$\begin{Bmatrix} \mathbf{a}_1 \\ \mathbf{a}_2 \\ \mathbf{a}_3 \end{Bmatrix} = \begin{bmatrix} c_\beta & -s_\beta & 0 \\ s_\beta & c_\beta & 0 \\ 0 & 0 & 1 \end{bmatrix} \begin{Bmatrix} \mathbf{b}_1 \\ \mathbf{b}_2 \\ \mathbf{b}_3 \end{Bmatrix} = C^{ab} \begin{Bmatrix} \mathbf{b}_1 \\ \mathbf{b}_2 \\ \mathbf{b}_3 \end{Bmatrix} \quad (95)$$

Let $\mathbf{e}_1, \mathbf{e}_2, \mathbf{e}_3$ be the unit basis vectors for the reference frame (\mathcal{F}_e) rotated from \mathcal{F}_b with Ψ (azimuth angle) of reference blade.

$$\begin{Bmatrix} \mathbf{b}_1 \\ \mathbf{b}_2 \\ \mathbf{b}_3 \end{Bmatrix} = \begin{bmatrix} c_\Psi & 0 & s_\Psi \\ 0 & 1 & 0 \\ -s_\Psi & 0 & c_\Psi \end{bmatrix} \begin{Bmatrix} \mathbf{e}_1 \\ \mathbf{e}_2 \\ \mathbf{e}_3 \end{Bmatrix} = C^{be} \begin{Bmatrix} \mathbf{e}_1 \\ \mathbf{e}_2 \\ \mathbf{e}_3 \end{Bmatrix} \quad (96)$$

The analytic modeling of an Engine/Propeller system can be formulated by incorporating the additional kinetic and potential energies to current methodology. Several additional terms will be added to the intrinsic governing equation Eq. (1). First, the kinetic and potential energies of the Engine/Propeller system are

$$\begin{aligned} K &= \frac{1}{2}(m_1 V_E^T V_E + \Omega_E^T i_E \Omega_E) + \frac{1}{2}(m_2 V_P^T V_P + \Omega_P^T i_P \Omega_P) \\ P &= \frac{1}{2}k_\alpha \alpha^2 + \frac{1}{2}k_\beta \beta^2 \end{aligned} \quad (97)$$

Here, the column matrix of the velocity vector of the pylon and propeller center of mass (V_E and V_P) and angular velocity of pylon and propeller (Ω_E and Ω_P) can be expressed in terms of the beam reference velocity variables (V, Ω) where the Engine/Propeller system is attached.

$$\begin{aligned} V_E &= C^{abT} C^{iaT} V + \tilde{\Omega}_E \xi_E \\ \Omega_E &= \Omega^* + \Omega_{\alpha\beta} \end{aligned} \quad (98)$$

where $\Omega^* = C^{abT} C^{iaT} \Omega$ and $\Omega_{\alpha\beta} = C^{abT} (\dot{\alpha} \mathbf{a}_1) + \dot{\beta} \mathbf{b}_3$ which is a relative angular velocity of the pylon with respect to the wing cross section.

With small angle assumption on α and β ,

$$\begin{aligned} V_E &= (\Delta - \tilde{\Theta}_E) V + \left(\widetilde{\Omega_{\Delta\Theta}} + \dot{\tilde{\Theta}}_E \right) \xi_E \\ \Omega_E &= (\Delta - \tilde{\Theta}_E) \Omega + \dot{\Theta}_E \\ V_P &= (\Delta - \tilde{\Theta}_E) V + \left(\widetilde{\Omega_{\Delta\Theta}} + \dot{\tilde{\Theta}}_E \right) \xi_P \\ \Omega_P &= (\Delta - \tilde{\Theta}_E) \Omega + \dot{\Theta}_P \end{aligned} \quad (99)$$

where $\Theta_E = [\alpha \ 0 \ \beta]^T$, $\Theta_P = [\alpha \ \Psi \ \beta]^T$, and $\Omega_{\Delta\Theta} = (\Delta - \tilde{\Theta}_E) \Omega$.

Taking variations on the kinetic energy K and potential energy P to apply these to Hamilton's principle Eq. (60),

$$\begin{aligned}
& \int_{t_1}^{t_2} \delta K dt \\
&= \int_{t_1}^{t_2} (\delta V_E^T P_E + \delta \Omega_E^T H_E + \delta V_P^T P_P + \delta \Omega_P^T H_P) dt \\
&= \int_{t_1}^{t_2} \left[\delta V^T (\Delta + \widetilde{\Theta}_E) (P_E + P_P) + \delta \Omega^T (\Delta + \widetilde{\Theta}_E) (H_E + H_P + \widetilde{\xi}_E P_E + \widetilde{\xi}_P P_P) \right] dt \\
&\quad + \int_{t_1}^{t_2} -\delta \Theta_E^T \left[(\widetilde{V} + \widetilde{\Omega} \widetilde{\xi}_E) P_E + \widetilde{\Omega} H_E + (\widetilde{V} + \widetilde{\Omega} \widetilde{\xi}_P) P_P + \widetilde{\Omega} H_P \right] dt \\
&\quad + \int_{t_1}^{t_2} \left[\delta \dot{\Theta}_E^T (\widetilde{\xi}_E P_E + H_E) + \delta \dot{\Theta}_P^T (\widetilde{\xi}_P P_P + H_P) \right] dt \\
&= \int_{t_1}^{t_2} (\dot{\overline{\delta q}}^T - \overline{\delta q}^T \widetilde{\Omega} - \overline{\delta \psi}^T \widetilde{V}) (\Delta + \widetilde{\Theta}_E) (P_E + P_P) dt \\
&\quad + \int_{t_1}^{t_2} (\dot{\overline{\delta \psi}}^T - \overline{\delta \psi}^T \widetilde{\Omega}) (\Delta + \widetilde{\Theta}_E) (H_E + H_P + \widetilde{\xi}_E P_E + \widetilde{\xi}_P P_P) dt \\
&\quad + \int_{t_1}^{t_2} -\delta \Theta_E^T \left[(\widetilde{V} + \widetilde{\Omega} \widetilde{\xi}_E) P_E + \widetilde{\Omega} H_E + (\widetilde{V} + \widetilde{\Omega} \widetilde{\xi}_P) P_P + \widetilde{\Omega} H_P \right] dt \\
&\quad + \int_{t_1}^{t_2} \left[\delta \dot{\Theta}_E^T (\widetilde{\xi}_E P_E + H_E) + \delta \dot{\Theta}_P^T (\widetilde{\xi}_P P_P + H_P) \right] dt
\end{aligned} \tag{100}$$

where $P_E = m_1 V_E$, $P_P = m_2 V_P$, $H_E = i_E \Omega_E$ and $H_P = i_P \Omega_P$.

$$\int_{t_1}^{t_2} \delta P dt = \int_{t_1}^{t_2} (k_\alpha \alpha \delta \alpha + k_\beta \beta \delta \beta) dt \tag{101}$$

The detailed virtual variation on the variables are as follows:

$$\begin{aligned}
\delta V_E^T &= \left\{ -\delta \widetilde{\Theta}_E V + (\Delta - \widetilde{\Theta}_E) \delta V + \left[-\widetilde{\delta \Theta}_E \widetilde{\Omega} + \widetilde{\delta \Omega}_{\Delta \Theta} + \delta \dot{\widetilde{\Theta}}_E \right] \xi_E \right\}^T \\
&= -\delta \Theta_E^T (\widetilde{V} + \widetilde{\Omega} \widetilde{\xi}_E) + \delta V^T (\Delta + \widetilde{\Theta}_E) + \delta \Omega^T (\Delta + \widetilde{\Theta}_E) \widetilde{\xi}_E + \delta \dot{\Theta}_E^T \widetilde{\xi}_E \\
\delta \Omega_E^T &= -\delta \Theta_E^T \widetilde{\Omega} + \delta \Omega^T (\Delta + \widetilde{\Theta}_E) + \delta \dot{\Theta}_E^T \\
\delta V_P^T &= -\delta \Theta_E^T (\widetilde{V} + \widetilde{\Omega} \widetilde{\xi}_P) + \delta V^T (\Delta + \widetilde{\Theta}_E) + \delta \Omega^T (\Delta + \widetilde{\Theta}_E) \widetilde{\xi}_P + \delta \dot{\Theta}_E^T \widetilde{\xi}_P \\
\delta \Omega_P^T &= -\delta \Theta_E^T \widetilde{\Omega} + \delta \Omega^T (\Delta + \widetilde{\Theta}_E) + \delta \dot{\Theta}_P^T
\end{aligned} \tag{102}$$

where $\delta \Omega_{\Delta \Theta} = (\Delta - \widetilde{\Theta}_E) \delta \Omega$. The final result can be incorporated into the intrinsic governing equation Eq. (1) with respect to $\overline{\delta q}$ and $\overline{\delta \psi}$. Moreover the result leads to three more equations about the additional generalized coordinates ($\delta \alpha$, $\delta \beta$, and $\delta \Psi$) in $\delta \Theta_E$ and $\delta \Theta_P$ due to the Engine/Propeller system.

If the Engine/Propeller system is located at the n^{th} node, the nodal equation is modified

as

$$\begin{aligned} \widehat{F}_r^n - \widehat{C}_{lr}^{nT} \widehat{F}_l^n + \widehat{\mu}^n \widehat{g}_r^n + \widehat{f}_{\text{aero}}^n - \dot{\widehat{P}}_r^n - \widetilde{\widehat{\Omega}}_r^n \widehat{P}_r^n \\ + \left[-\widetilde{\widehat{\Omega}}_r^n (\Delta + \widetilde{\Theta}_E) + \dot{\widetilde{\Theta}}_E \right] (P_E + P_P) - (\Delta + \widetilde{\Theta}_E) (\dot{P}_E + \dot{P}_P) = 0 \end{aligned} \quad (103)$$

$$\begin{aligned} \widehat{M}_r^n - \widehat{C}_{lr}^{nT} \widehat{M}_l^n + \widehat{\mu}^n \widetilde{\xi}^n \widehat{g}_r^n + \widehat{m}_{\text{aero}}^n - \dot{\widehat{H}}_r^n - \widetilde{\widehat{\Omega}}_r^n \widehat{H}_r^n - \widetilde{\widehat{V}}_r^n \widehat{P}_r^n \\ - \widetilde{\widehat{V}}_r^n (\Delta + \widetilde{\Theta}_E) (P_E + P_P) + \left[-\widetilde{\widehat{\Omega}}_r^n (\Delta + \widetilde{\Theta}_E) + \dot{\widetilde{\Theta}}_E \right] (H_E + H_P + \widetilde{\xi}_E P_E + \widetilde{\xi}_P P_P) \\ - (\Delta + \widetilde{\Theta}_E) (\dot{H}_E + \dot{H}_P + \widetilde{\xi}_E \dot{P}_E + \widetilde{\xi}_P \dot{P}_P) = 0 \end{aligned} \quad (104)$$

$$\widehat{g}_r^n - (\Delta + \widetilde{\Theta}_E) \widehat{g}_{\alpha\beta} = 0 \quad (105)$$

where $\widehat{g}_{\alpha\beta}$ is the column matrix of the components of the gravity vector in Engine/Propeller basis. For $\delta\Theta_E$ and $\delta\Theta_P$ in terms of $\delta\alpha, \delta\beta$ and $\delta\Psi$,

$$\begin{aligned} (e_1 e_1^T + e_3 e_3^T) \left[(\widetilde{\widehat{V}}^n + \widetilde{\widehat{\Omega}}^n \widetilde{\xi}_E) (P_E + P_P) + \widetilde{\widehat{\Omega}}^n (H_E + H_P) + \dot{H}_E + \widetilde{\xi}_E \dot{P}_E + \dot{H}_P + \widetilde{\xi}_P \dot{P}_P \right] \\ + \begin{Bmatrix} k_\alpha \alpha \\ 0 \\ k_\beta \beta \end{Bmatrix} = \begin{Bmatrix} 0 \\ 0 \\ 0 \end{Bmatrix} \\ e_2 e_2^T (\widetilde{\xi}_P \dot{P}_P + \dot{H}_P) = 0 \end{aligned} \quad (106)$$

where $e_1 = [1 \ 0 \ 0]^T$, $e_2 = [0 \ 1 \ 0]^T$ and $e_3 = [0 \ 0 \ 1]^T$. The previous final equations are for the three-bladed case. For the two-bladed case, the inertia matrix is not constant and becomes periodic in time if it is expressed in the hub-fixed reference frame to be included in the nodal equation. Eq. (100) should then include a variation on the inertia matrix such that

$$\frac{1}{2} \Omega_p^T \delta(i_p) \Omega_p = \delta\Psi \frac{1}{2} \Omega_p^T i_\Psi \Omega_p \quad (107)$$

where

$$\begin{aligned}
i_p &= \mathbf{b} \cdot \mathbf{i}_p \cdot \mathbf{b} = C^{be} I_{[\mathcal{F}_e]} C^{beT} \\
&= \begin{bmatrix} c_\Psi & 0 & s_\Psi \\ 0 & 1 & 0 \\ -s_\Psi & 0 & c_\Psi \end{bmatrix} \begin{bmatrix} I_1^* & 0 & 0 \\ 0 & I_2^* & 0 \\ 0 & 0 & I_3^* \end{bmatrix} \begin{bmatrix} c_\Psi & 0 & s_\Psi \\ 0 & 1 & 0 \\ -s_\Psi & 0 & c_\Psi \end{bmatrix}^T = \begin{bmatrix} I_1^* c_\Psi^2 & 0 & -I_1^* c_\Psi s_\Psi \\ 0 & I_2^* & 0 \\ -I_1^* c_\Psi s_\Psi & 0 & I_1^* s_\Psi^2 \end{bmatrix} \\
\delta i_p &= \delta \Psi \begin{bmatrix} -2I_1^* c_\Psi s_\Psi & 0 & I_1^* (c_\Psi^2 - s_\Psi^2) \\ 0 & 0 & 0 \\ I_1^* (c_\Psi^2 - s_\Psi^2) & 0 & 2I_1^* s_\Psi c_\Psi \end{bmatrix} = \delta \Psi i_\Psi
\end{aligned} \tag{108}$$

if $I_3^* \approx 0$. This difference only modifies the Eq. (106).

$$e_2 e_2^T (\widetilde{\xi_P} \dot{P}_P + \dot{H}_P) + \frac{1}{2} \Omega_p^T i_\Psi \Omega_p = 0 \tag{109}$$

3.3.2 Propeller Aerodynamics

The propeller aerodynamic model is evaluated from the blade element theory using the 2-D aerodynamics of Ref. [26].

The following descriptions on propeller aerodynamics are for the Engine/Propeller system located at right wing with positive angular velocity. Let's first evaluate the velocity vector of point B on a blade, given by

$$V_B = \begin{bmatrix} c_\Psi & 0 & -s_\Psi \\ 0 & 1 & 0 \\ s_\Psi & 0 & c_\Psi \end{bmatrix} V_P + \begin{Bmatrix} r\omega_o \\ 0 \\ 0 \end{Bmatrix} \tag{110}$$

where $V_{Bi} = \mathbf{V}_B \cdot \mathbf{e}_i$. The angle of attack can be defined as

$$\alpha_{AOA} = \Theta_{tw}(r) + \alpha_{wind} \tag{111}$$

where Θ_{tw} is the twist angle along the radius of the blade and $\alpha_{wind} = \tan^{-1} \left(\frac{-V_{B2}}{V_{B1}} \right)$.

The average thrust (T_o) and side forces (H_o, Y_o) can be written as

$$\begin{aligned} Y_o &= N \frac{1}{2\pi} \int_0^{2\pi} \int_0^{d/2} qc (c_{l_\alpha} \alpha_{\text{AOA}} s_{\alpha_{\text{wind}}} - c_d c_{\alpha_{\text{wind}}}) c_\Psi dr d\Psi \\ T_o &= N \frac{1}{2\pi} \int_0^{2\pi} \int_0^{d/2} qc (c_{l_\alpha} \alpha_{\text{AOA}} c_{\alpha_{\text{wind}}} + c_d s_{\alpha_{\text{wind}}}) dr d\Psi \\ H_o &= -N \frac{1}{2\pi} \int_0^{2\pi} \int_0^{d/2} qc (c_{l_\alpha} \alpha_{\text{AOA}} s_{\alpha_{\text{wind}}} - c_d c_{\alpha_{\text{wind}}}) s_\Psi dr d\Psi \end{aligned} \quad (112)$$

where $q = \frac{1}{2}\rho U^2$, $U^2 = V_{B1}^2 + V_{B2}^2$, N is the number of blades, and c is the chord length.

The average torque (Q_o) and hub moments (M_x, M_z) can be written as

$$\begin{aligned} M_x &= -N \frac{1}{2\pi} \int_0^{2\pi} \int_0^{d/2} qc (c_{l_\alpha} \alpha_{\text{AOA}} c_{\alpha_{\text{wind}}} + c_d s_{\alpha_{\text{wind}}}) r c_\Psi dr d\Psi \\ Q_o &= N \frac{1}{2\pi} \int_0^{2\pi} \int_0^{d/2} qc (c_{l_\alpha} \alpha_{\text{AOA}} s_{\alpha_{\text{wind}}} - c_d c_{\alpha_{\text{wind}}}) r dr d\Psi \\ M_z &= N \frac{1}{2\pi} \int_0^{2\pi} \int_0^{d/2} qc (c_{l_\alpha} \alpha_{\text{AOA}} c_{\alpha_{\text{wind}}} + c_d s_{\alpha_{\text{wind}}}) r s_\Psi dr d\Psi \end{aligned} \quad (113)$$

$$\begin{aligned} \mathbf{F}_{\text{prop}} \cdot \mathbf{b} &= \begin{Bmatrix} Y_o \\ T_o \\ H_o \end{Bmatrix}, \quad \delta \mathbf{r}_{\mathbf{p}} \cdot \mathbf{b} = (\Delta - \widetilde{\Theta}_E) \overline{\delta q} + \left[(\Delta - \widetilde{\Theta}_E) \overline{\delta \psi} + \delta \widetilde{\Theta}_E \right] \xi_p \\ \mathbf{M}_{\text{prop}} \cdot \mathbf{b} &= \begin{Bmatrix} M_x \\ Q_o \\ M_z \end{Bmatrix}, \quad \overline{\delta \psi}_{\mathbf{p}} \cdot \mathbf{b} = (\Delta - \widetilde{\Theta}_E) \overline{\delta \psi} + \delta \Theta_E \end{aligned} \quad (114)$$

The virtual work by the propeller airloads and gravity force is

$$\begin{aligned} \overline{\delta W} &= (\mathbf{F}_{\text{prop}} + \mathbf{F}_{g2}) \cdot \delta \mathbf{r}_{\mathbf{p}} + \mathbf{F}_{g1} \cdot \delta \mathbf{r}_{\mathbf{e}} + \mathbf{M}_{\text{prop}} \cdot \overline{\delta \psi}_{\mathbf{p}} + Q_A \delta \Psi \\ &= \left[\overline{\delta q}^T (\Delta + \widetilde{\Theta}_E) + \overline{\delta \psi}^T (\Delta + \widetilde{\Theta}_E) \widetilde{\xi}_P + \delta \Theta_E^T \widetilde{\xi}_P \right] \left\{ \begin{Bmatrix} Y_o \\ T_o \\ H_o \end{Bmatrix} + m_2 \widehat{g}_{\alpha\beta} \right\} \\ &\quad + \left[\overline{\delta q}^T (\Delta + \widetilde{\Theta}_E) + \overline{\delta \psi}^T (\Delta + \widetilde{\Theta}_E) \widetilde{\xi}_E + \delta \Theta_E^T \widetilde{\xi}_E \right] m_1 \widehat{g}_{\alpha\beta} \\ &\quad + \left[\overline{\delta \psi}^T (\Delta + \widetilde{\Theta}_E) + \delta \Theta_E^T \right] \begin{Bmatrix} M_x \\ Q_o \\ M_z \end{Bmatrix} + Q_A \delta \Psi \end{aligned} \quad (115)$$

where \mathbf{F}_{prop} is the propeller force vector, \mathbf{M}_{prop} is the propeller moment vector, \mathbf{F}_{g_1} is the gravity force vector of pylon, \mathbf{F}_{g_2} is the gravity force vector of total blade, and \mathbf{Q}_A is the applied torque vector.

These generalized forces and moments are included in the previous equations Eq. (103) – (106). For powered rotation, the last equation in Eq. (106) or (109) can be eliminated from the formulation which are associated with the virtual variation on Ψ , but it should be included when it is needed to calculate the applied torque (Q_A) required to maintain constant propeller angular speed (ω_o) or for free-rotation case.

CHAPTER IV

PARAMETRIC STUDY

The following parametric studies illustrate some of the uses of the current HALE aircraft analysis methodology by completing the proposed three modeling demands.

- 4.1: Payload Distribution
 - The effect of payload distribution along a highly flexible flying wing aircraft on flight dynamic characteristics is investigated.
- 4.2: Horizontal Tail's Contribution
 - The aerodynamic contribution of horizontal tail's size and location on flight dynamics characteristics is studied.
- 4.3: Modal Characteristics of Stiff and Flexible Beams in GVT
 - The modal characteristics of stiff and flexible beams in GVT are shown to be possible to couple GVT rigid-body modes and the lowest structural modes for highly flexible beams.
- 4.4: Modal Characteristics of a Highly Flexible Beam for Different Bungee Cord Locations
 - Different bungee cord locations are considered to observe the difference in modal characteristics of highly flexible beams.
- 4.5: Modal Characteristics of Flying Wing and Conventional Configuration in GVT
 - This parametric study compares the modal characteristics between flying wing and conventional aircraft configurations.
- 4.6: Time Simulation of NATASHA_{WF}
 - The nonlinear dynamic simulation with Engine/Propeller model shows three possible

time histories such as decaying, divergent motions, and periodic oscillation especially when certain propeller-driven HALE aircraft have an unstable mode.

- 4.7: Periodic Inertia Effect of Two-Bladed Engine/Propeller System
 - A boundary for certain HALE aircraft configuration is determined about in which condition the two-bladed Engine/Propeller system can be treated like an equivalent three-bladed Engine/Propeller system so that Floquet theory is not required.
- 4.8 : Periodic Propeller Airloads
 - The trim condition determined by the constant approximation on the propeller airloads is verified whether the trim states are disturbed by the periodic side forces and moments.

4.1 Payload Distribution

One big difference in highly flexible HALE aircraft is that they operate under large wing deflection. The deformation of the highly flexible wing is affected by how the payload is distributed along the span. Therefore, the effect of payload distribution along the highly flexible flying wing aircraft on flight dynamic and aeroelastic characteristics is investigated. If the given payload is evenly distributed, the deformation will be small. However, if it is concentrated at mid-span, the wing deforms to a U shape with a much larger tip deflection. The deformed shape of the highly flexible wing may lead to the changes in the flight dynamic characteristics.

Two cases are compared to each other with same total payload: Case I with payloads ($35/13 \approx 2.6923$ kg) located at nodes from 3 to 15 and Case II with concentrated payload (35 kg) at mid-span. (the corresponding node is 9th.)

Figures 5 and 6 show the deformed shape of Cases I and II in trim condition with parameters in Table 1. The large wing tip deflection is seen in Figure 6 due to the concentrated payload 35 kg at mid-span. Case I shows relatively small wing deformation because the payloads are evenly distributed from node 3 to 15. Intermediate cases are exercised to observe how the eigenvalues change from Case I to Case II and one additional case is added

which the payloads are evenly distributed from node 1 to 17 along the whole span.

Figure 7 shows the root locus of three lowest eigenvalues. The 1st eigenvalue is related to the pitch attitude and 1st structural bending modes. (The partition of each mode on the 1st eigenvalues depends on the payload distribution.) The 2nd eigenvalue is related to the yaw attitude mode. As the payload gets distributed over a larger portion of the wing span (from “★” to “o” in Figure 7), the eigenvalues become more unstable. At some configuration, the 1st and 2nd eigenvalues for the flight dynamics modes become unstable. If the payloads are evenly distributed from node 1 to 17 along the whole span, the wing is deflected to downward which is an inverted U shape (corresponding “o” in Figure 7). The U shape of highly flexible aircraft provides much stable flight dynamic characteristics than the less deformed shapes or inverted U shape. As the beam flexibility increase there would be more U shape for more stable flight dynamic characteristic. On the other hand, as the wing becomes more flexible, it would be more prone to wing flutter. Figure 8 shows that 4th eigenvalue associated with 1st structural bending mode becomes unstable after certain flexibility. The vertical bending stiffness (EI_2) decreases from $2.0 \times 10^4 \text{ Nm}^2$ (corresponding to “o” in Figure 8) to $1.0 \times 10^4 \text{ Nm}^2$ (corresponding “★” in Figure 8) and the payload at mid-span is a fixed value of 21 kg.

Table 1: Parameters in “Payload Distribution”

parameters		values	units
m	(mass per unit length)	0.75	kg/m
ℓ	(length of flying wing)	16	m
UU	(magnitude of aircraft forward velocity)	20	m/sec
phi	(flight path angle)	0	rad
GJ	(Torsional stiffness)	1.0×10^4	Nm^2
EI_2	(Vertical Bending stiffness)	2.0×10^4	Nm^2
EI_3	(Chordwise Bending stiffness)	4.0×10^6	Nm^2

Table 2: Three lowest eigenvalues of each case in “Payload Distribution”

Case	1 st eigenvalue	2 nd eigenvalue	3 rd eigenvalues
node 9 (Case I, “★”)	$-0.0621 \pm 0.4060 i$	$-0.0003 \pm 0.5691 i$	$-3.5334 \pm 1.7659 i$
node 3 to 15 (Case II)	$-0.0120 \pm 0.2361 i$	$0.0195 \pm 0.6269 i$	$-1.9983 \pm 1.0742 i$
node 1 to 17 (“o”)	$0.1233 \pm 0.0000 i$	$0.0266 \pm 0.6391 i$	$-1.7072 \pm 0.6366 i$

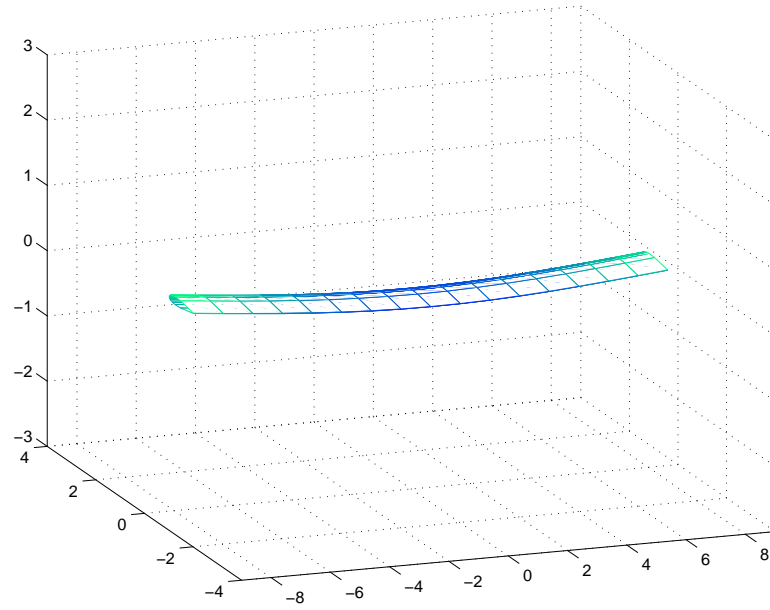


Figure 5: Trim configuration of Case I of "Payload Distribution"

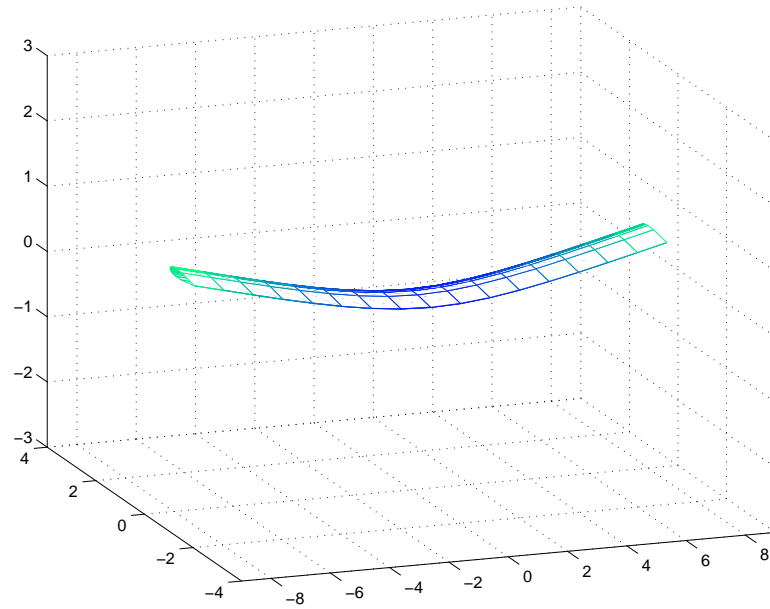


Figure 6: Trim configuration of Case II of "Payload Distribution"

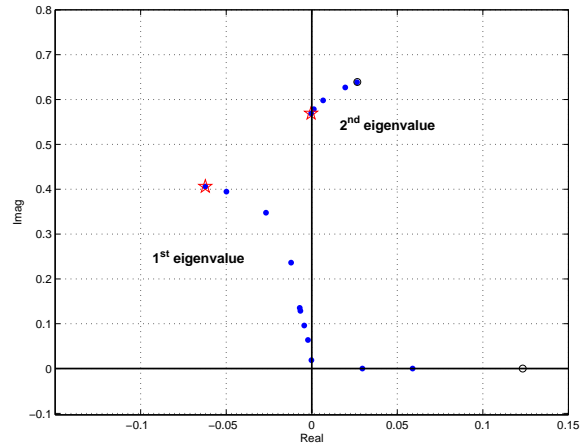
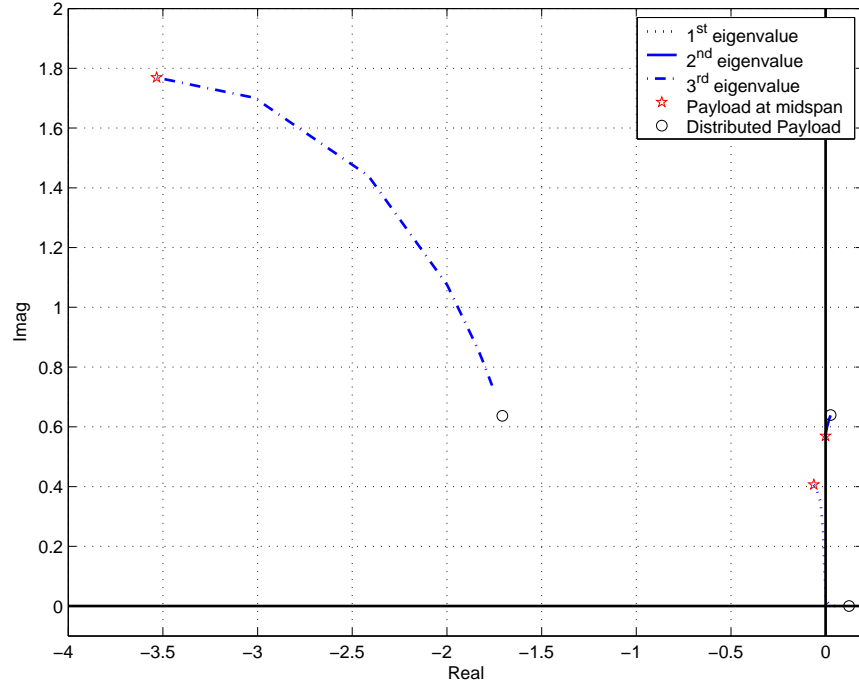


Figure 7: Root locus of three lowest eigenvalues of “Payload Distribution” (lower figure is zoomed in for 1st and 2nd eigenvalues)

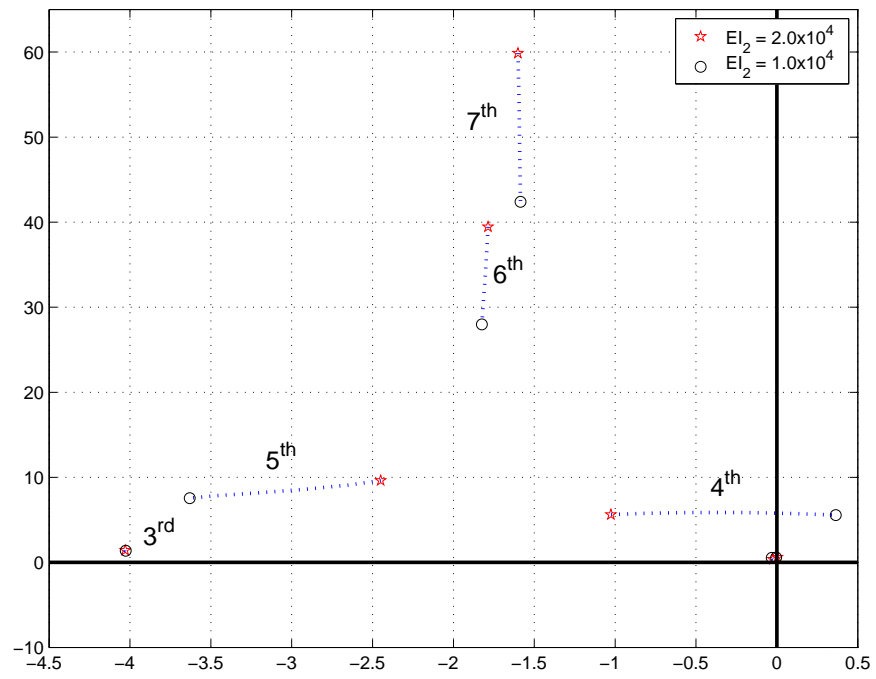


Figure 8: Root locus of seven lowest eigenvalues depending on beam flexibility

4.2 Horizontal Tail's Contribution

Some highly flexible flying wings have a mildly unstable phugoid mode. Now with the contribution of the present work the structural modeling can include the fuselage and horizontal tail. Thus, the possible aerodynamic contribution of horizontal tail's size and location on the mildly unstable phugoid mode can be studied.

It is assumed that the horizontal tail's mass is neglected along with the fuselage aerodynamics and mass so as to see only the aerodynamic contribution of horizontal tail. The fuselage stiffnesses are $GJ = 10^6$, $EI_2 = 2 \times 10^6$, $EI_3 = 4 \times 10^8$ Nm². The horizontal tail is located at 2 m from the wing reference line and its aerodynamic contribution is set by the ratio of horizontal tail's chord to the wing's. Additionally, the elevator angle (δ_e) in horizontal tail is set as default value 0° for all the cases. In Figure 9, the flight dynamics modes move to the left half plane as the aerodynamic contribution of horizontal tail increases from the case without horizontal tail to 67% chord size.

Next, like the previous study the horizontal tail with 10% chord size and 0° elevator deflection is located at 2 m from the wing reference line. The location of the tail is defined by the length of the fuselage from the wing reference line. In Figure 10, the flight dynamics modes move to the left half plane as the horizontal tail is located farther from the wing reference line. So if a horizontal tail can provide enough aerodynamic force and moment, it would improve the stability of the flight dynamic characteristic of a highly flexible flying wing aircraft.

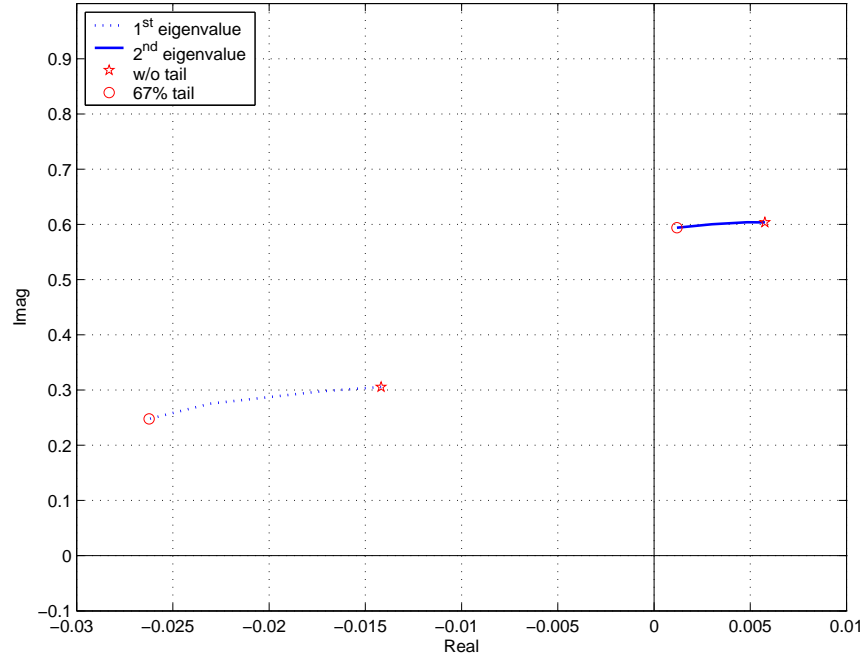


Figure 9: Root locus of three lowest eigenvalues of “Contribution of Horizontal Tail’s Aerodynamics: size”

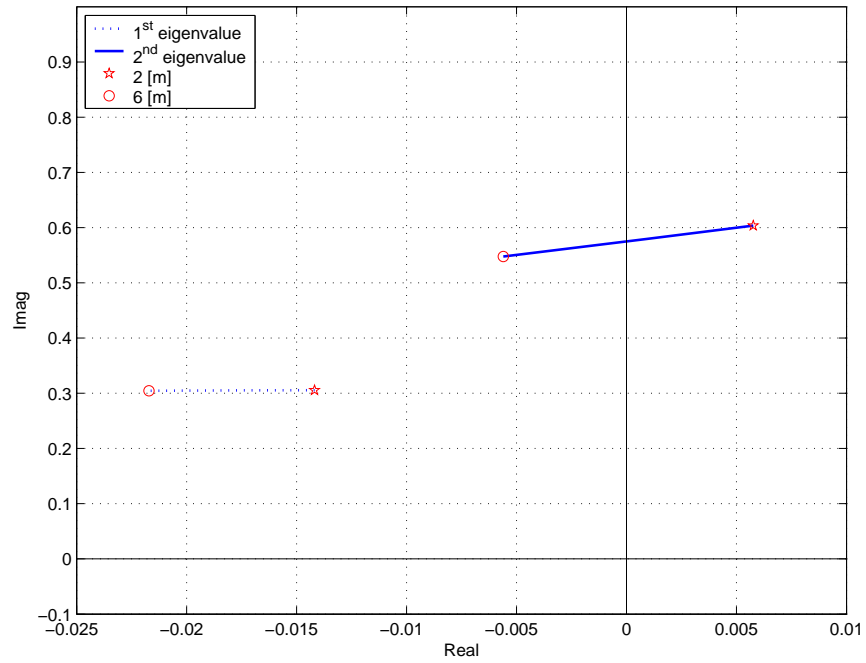


Figure 10: Root locus of three lowest eigenvalues of “Contribution of Horizontal Tail’s Aerodynamics: location”

Table 3: Eigenvalues of “Contribution of Horizontal Tail’s Aerodynamics: size”

Case	Eigenvalues	
size	1 st eigenvalue	2 nd eigenvalue
w/o tail	$-0.0124 \pm 0.3111 \ i$	$0.0063 \pm 0.6017 \ i$
10%	$-0.0141 \pm 0.3055 \ i$	$0.0057 \pm 0.6035 \ i$
25%	$-0.0172 \pm 0.2979 \ i$	$0.0048 \pm 0.6037 \ i$
50%	$-0.0230 \pm 0.2752 \ i$	$0.0030 \pm 0.6002 \ i$
67%	$-0.0262 \pm 0.2478 \ i$	$0.0011 \pm 0.5969 \ i$

Table 4: Eigenvalues of “Contribution of Horizontal Tail’s Aerodynamics: location”

Case	Eigenvalues	
location	1 st eigenvalue	2 nd eigenvalue
2 m	$-0.0141 \pm 0.3055 \ i$	$0.0057 \pm 0.6035 \ i$
4 m	$-0.0174 \pm 0.3053 \ i$	$0.0009 \pm 0.5795 \ i$
6 m	$-0.0217 \pm 0.3044 \ i$	$-0.0056 \pm 0.5476 \ i$

4.3 Modal Characteristics of Stiff and Flexible Beams

By comparing the modal characteristics between stiff and flexible beams in GVT, the possible coupling of GVT rigid-body modes and the lowest frequency structural modes for a highly flexible beam is shown.

The GVT static equilibria of both stiff and flexible beams with attached bungee cords are computed numerically. 3D and 2D plots are given in Figures 11 and 12. (x , y , and z correspond to the inertial basis n_1, n_2 and n_3 in the figures.) The beams are loaded only by their own weight. The beam is attached one bungee cord at each end. The properties of stiff and flexible beams are given in Table 5. The stiffness (k) of bungee cords are 2000 N/m and natural length (ℓ) is 1 m. Table 6 shows the converged solutions of static equilibrium.

Table 5: Stiff and flexible beams beam properties: GJ (torsional stiffness: Nm^2), EI_2 , EI_3 (bending stiffness: Nm^2), N (number of elements), ℓ (length of the beam: m), and m (mass per unit length: kg/m)

	GJ	EI_2	EI_3	N	ℓ	m
Stiff Beam	10^6	10^8	10^8	10	10	10
Flexible Beam	10^4	2×10^4	2×10^4	10	10	10

Table 6: Static equilibrium solution of stiff and flexible beam (upper and lower tables for stiff and flexible beams respectively)

$pOB_{1n}^*[m]$	$pOB_{2n}^*[m]$	$C_{1,2}$	$\sigma_k[m]$	τ_{k_n}
$\begin{Bmatrix} 0.0000 \\ 0.0000 \\ 8.4852 \end{Bmatrix}$	$\begin{Bmatrix} 10.0000 \\ 0.0000 \\ 8.4852 \end{Bmatrix}$	$\begin{bmatrix} 1.0000 & 0.0000 & 0.0000 \\ 0.0000 & 1.0000 & 0.0000 \\ 0.0000 & 0.0000 & 1.0000 \end{bmatrix}$	0.4147	$\begin{Bmatrix} 0.0000 \\ 0.0000 \\ -1.0000 \end{Bmatrix}$
$\begin{Bmatrix} 0.0460 \\ 0.0000 \\ 8.4881 \end{Bmatrix}$	$\begin{Bmatrix} 9.9539 \\ 0.0000 \\ 8.4881 \end{Bmatrix}$	$\begin{bmatrix} 0.9812 & 0.0000 & \pm 0.1928 \\ 0.0000 & 1.0000 & 0.0000 \\ \mp 0.1928 & 0.0000 & 0.9812 \end{bmatrix}$	0.4152	$\begin{Bmatrix} \pm 0.0461 \\ 0.0000 \\ -0.9989 \end{Bmatrix}$

Tables 7 and 8 show the ten lowest eigenvalues about the static equilibrium with each description on the associated mode. In these tables, the six lowest eigenvalues are associated with the GVT rigid-body modes (See the details about GVT rigid-body modes in Appendix A.) The rest are associated with structural modes. (For displaying a structural mode shape, only one reference line is magnified enough to be observed.) The corresponding eigenmodes are given in Figures 13 – 17.

In eigenanalysis for the stiff beam, the GVT rigid-body modes are clearly separated

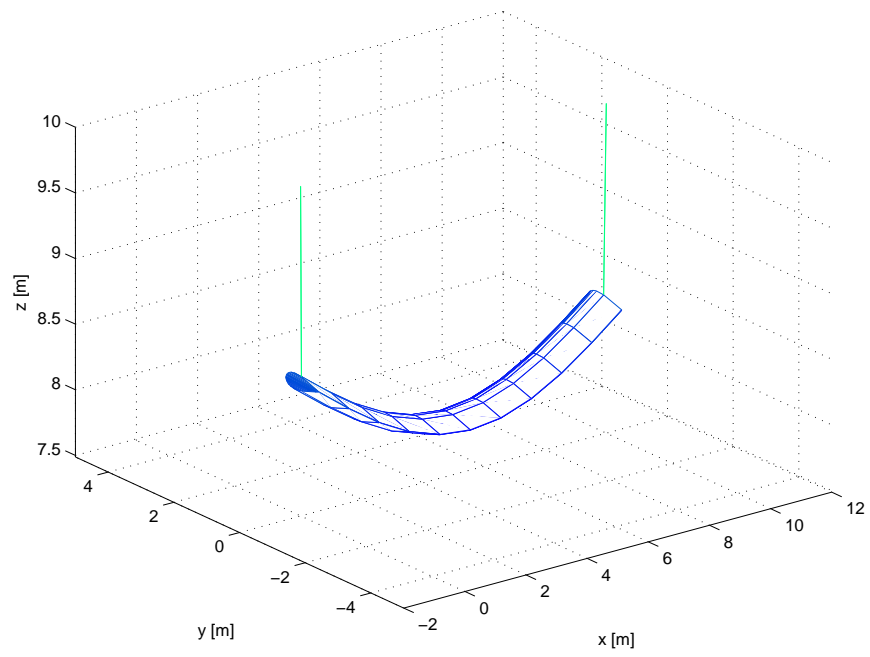
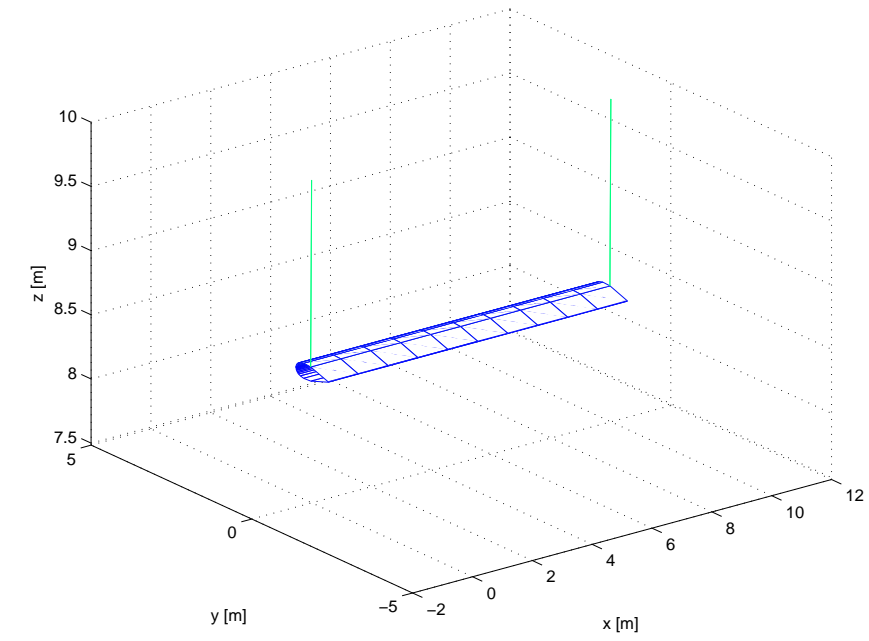


Figure 11: 3D plot of the GVT static equilibria of stiff and flexible beams

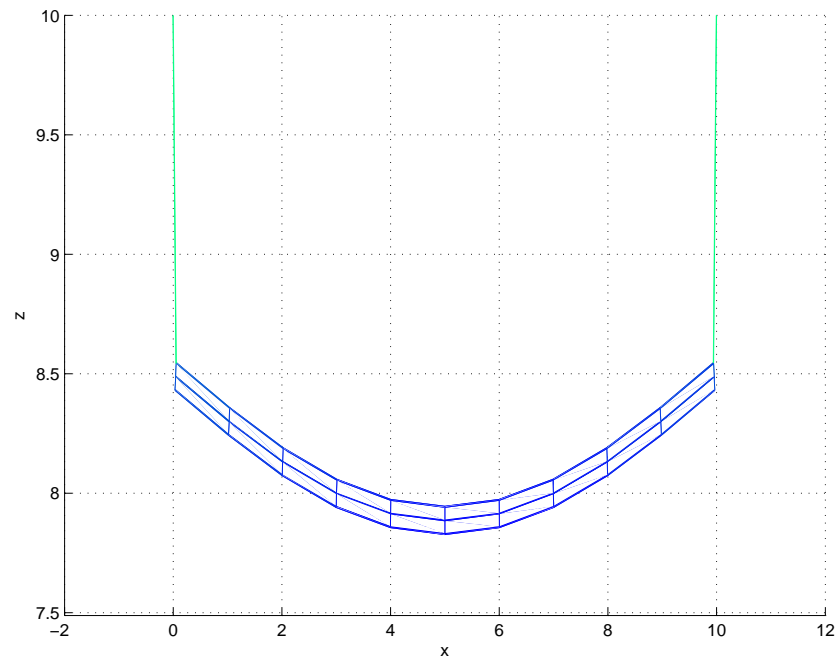
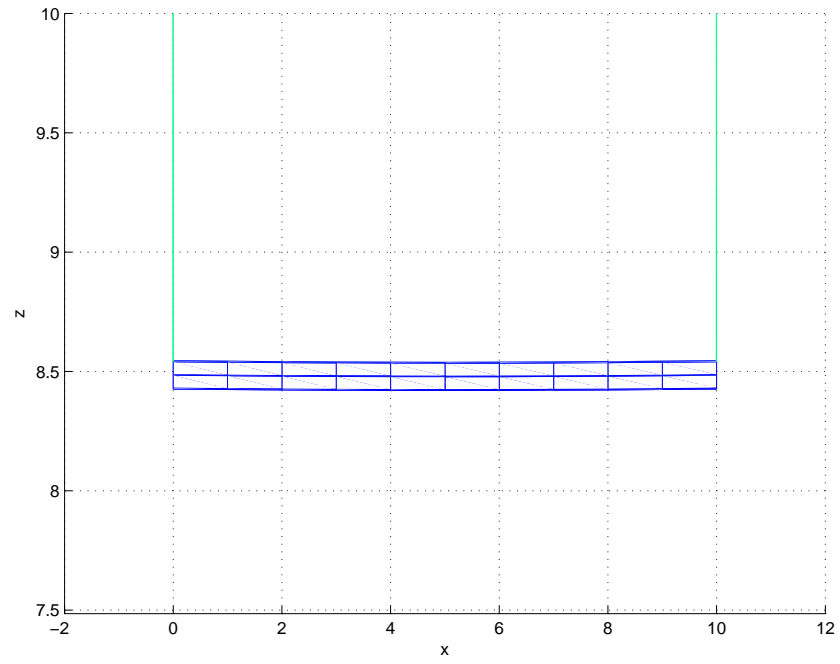


Figure 12: 2D plot of the static equilibria of stiff and flexible beams

from the structural modes as the eigenvalues are shown in Table 7. However, with regard to the highly flexible beam, the 1st symmetric elastic bending modes with respect to \mathbf{n}_2 (flapwise) and \mathbf{n}_3 (chordwise) drops significantly and becomes quite close to the pitching modes and those might not be separated enough to the GVT rigid-body modes. The four lowest eigenvalues of a free-free beam simulated by NATASHA are shown in Table 9. It confirms the possible coupling between the GVT rigid-body modes and low structural modes, leading about 16 – 24% relative difference for the 1st symmetric bending modes and 2.1 – 3.4% for 1st anti-symmetric bending modes. It indicates that the lowest structural frequencies are significantly overestimated by the presence of bungee cords.

Table 7: Six GVT rigid-body and four lowest GVT structural modes and corresponding eigenvalues of stiff beam

Eigenvalues	Description
$0 \pm 2.5389 i$	swing mode w.r.t \mathbf{n}_1 + plunging mode
$0 \pm 2.6329 i$	swing mode w.r.t \mathbf{n}_2
$0 \pm 3.6123 i$	plunging mode
$0 \pm 4.5838 i$	twisting mode
$0 \pm 6.2987 i$	rolling mode
$0 \pm 10.272 i$	pitching mode
$0 \pm 733.81 i$	1 st symm. structural bending mode w.r.t \mathbf{n}_3
$0 \pm 733.83 i$	1 st symm. structural bending mode w.r.t \mathbf{n}_2
$0 \pm 1001.8 i$	1 st structural torsional mode
$0 \pm 2055.0 i$	2 nd symm. structural bending mode w.r.t \mathbf{n}_2

Table 8: Ten lowest GVT modes and corresponding eigenvalues of flexible beam

Eigen values	Description
$0 \pm 2.2625 i$	swing mode w.r.t \mathbf{n}_1 + plunging mode
$0 \pm 2.6317 i$	swing mode w.r.t \mathbf{n}_2
$0 \pm 2.9491 i$	plunging mode
$0 \pm 4.4934 i$	twisting mode
$0 \pm 6.0759 i$	rolling mode
$0 \pm 9.7848 i$	pitching mode
$0 \pm 12.114 i$	1 st symm. structural bending mode w.r.t \mathbf{n}_3
$0 \pm 12.907 i$	1 st symm. structural bending mode w.r.t \mathbf{n}_2
$0 \pm 31.346 i$	1 st anti-symm. structural bending mode w.r.t \mathbf{n}_3
$0 \pm 31.760 i$	1 st anti-symm. structural bending mode w.r.t \mathbf{n}_2

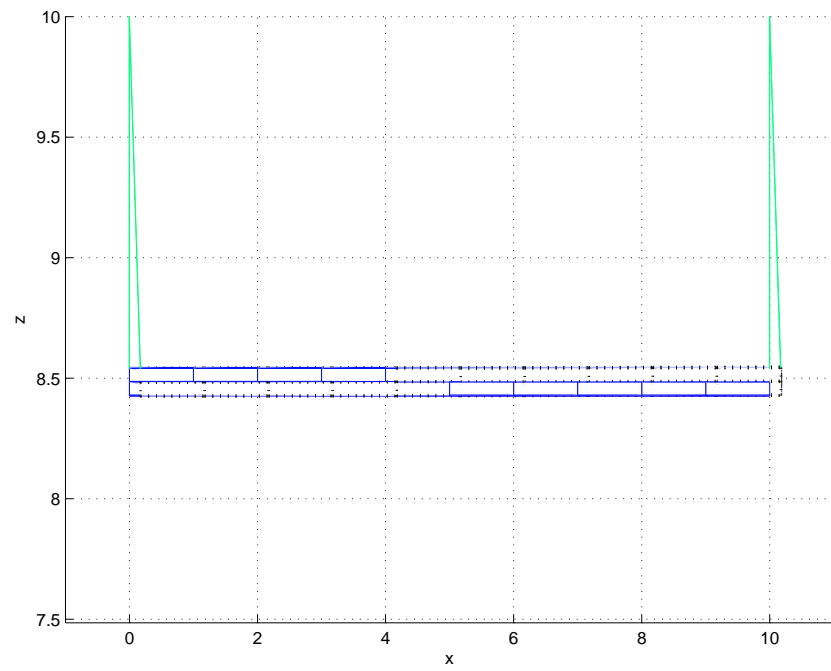
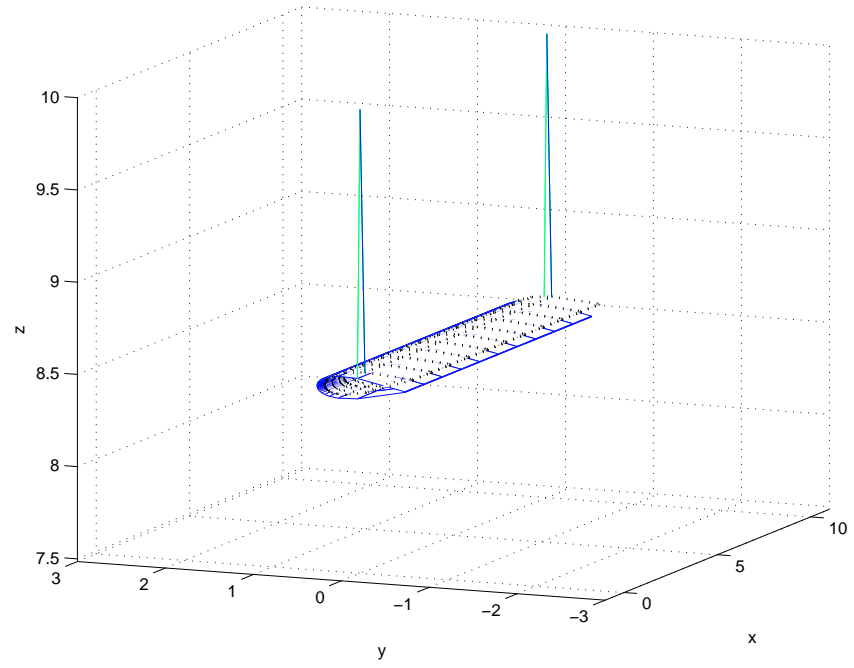


Figure 13: 1st and 2nd GVT rigid-body modeshapes of stiff beam

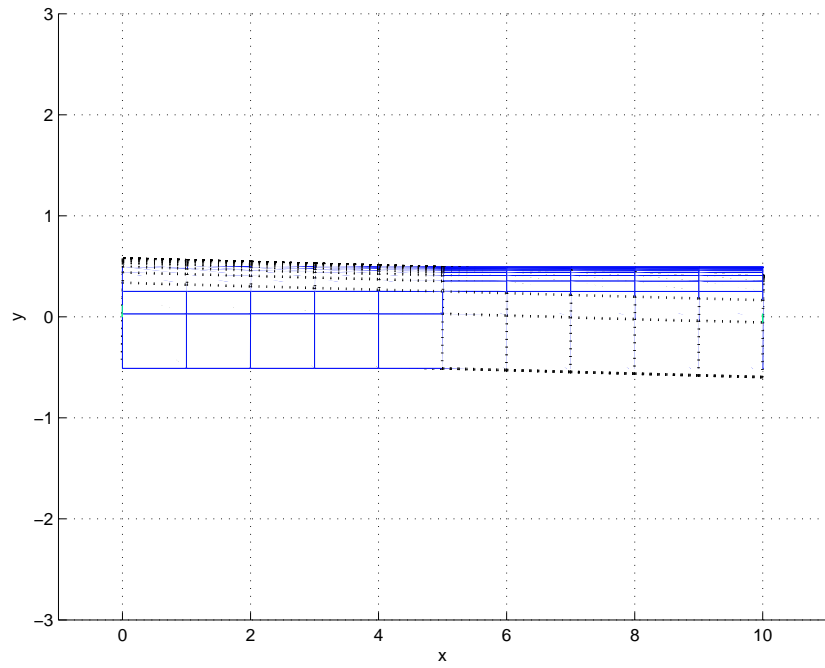
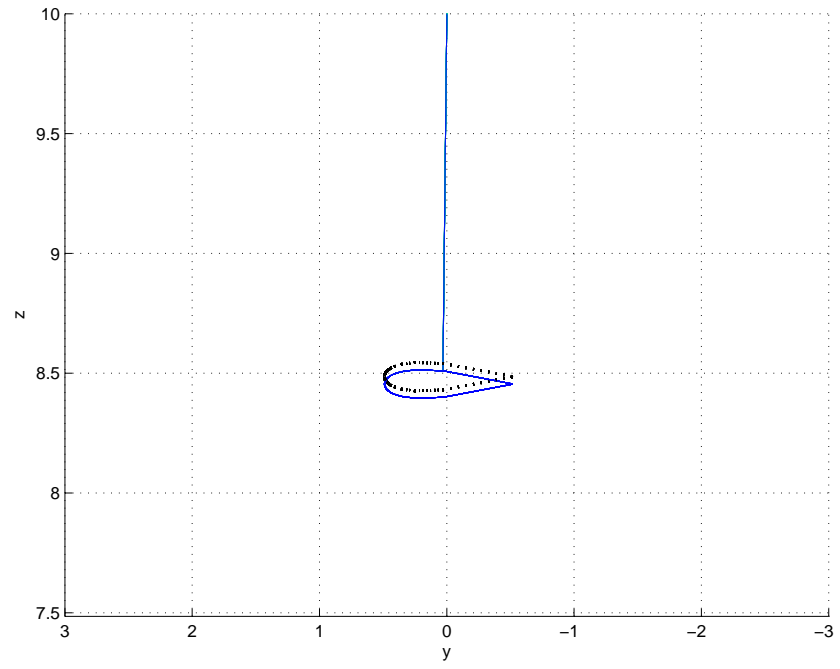


Figure 14: 3rd and 4th GVT rigid-body modeshapes of stiff beam

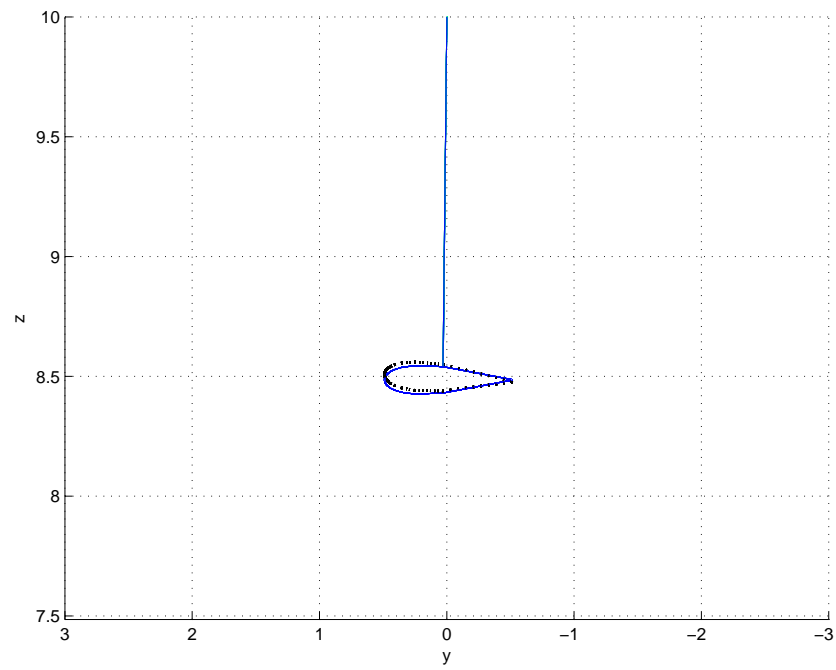
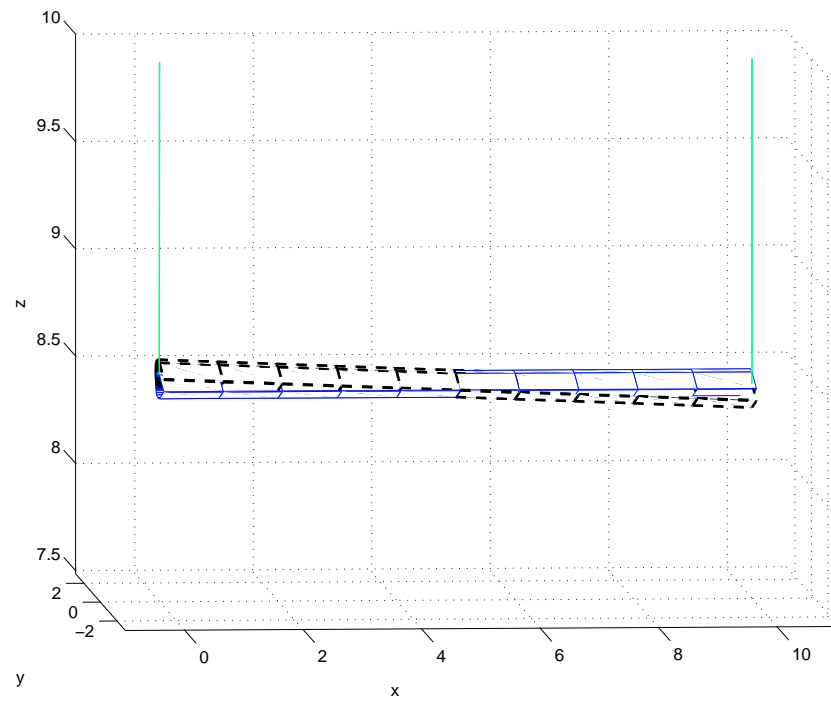


Figure 15: 5th and 6th GVT rigid-body modeshapes of stiff beam

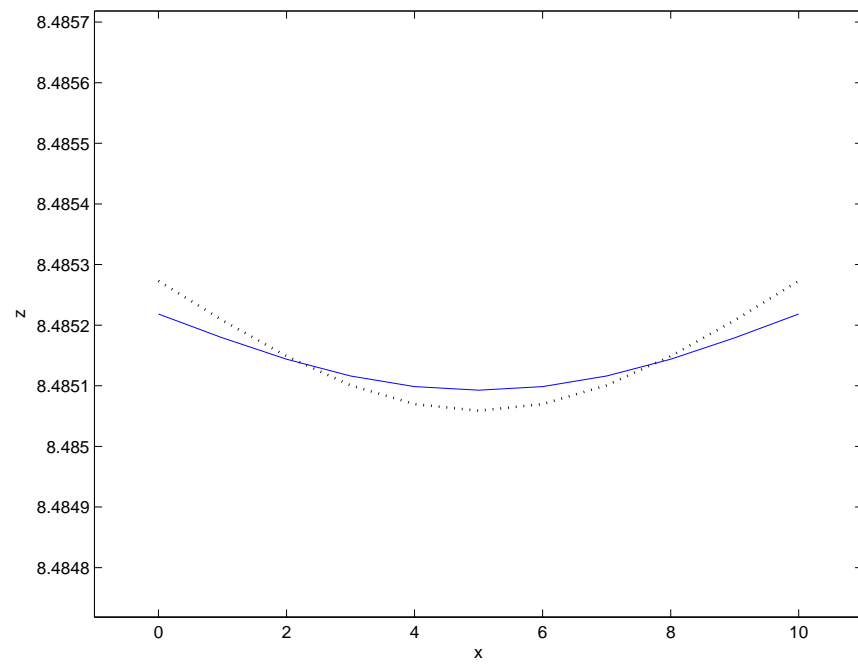
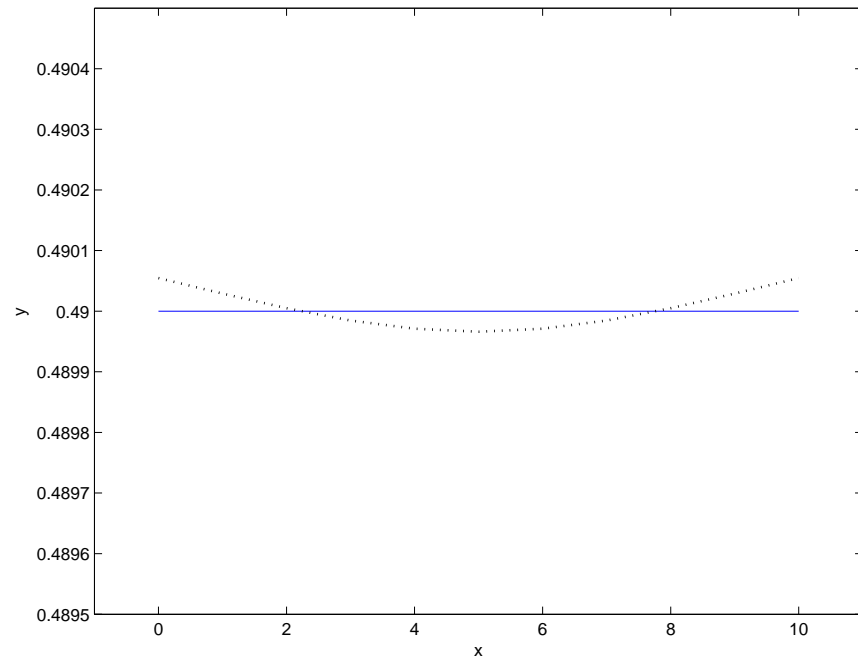


Figure 16: 1st and 2nd GVT structural modeshapes of stiff beam

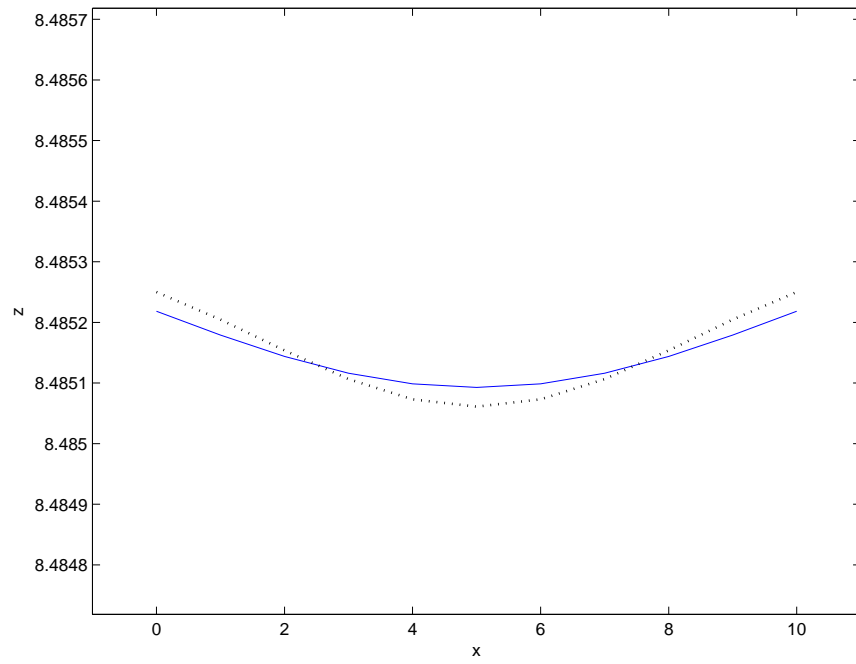
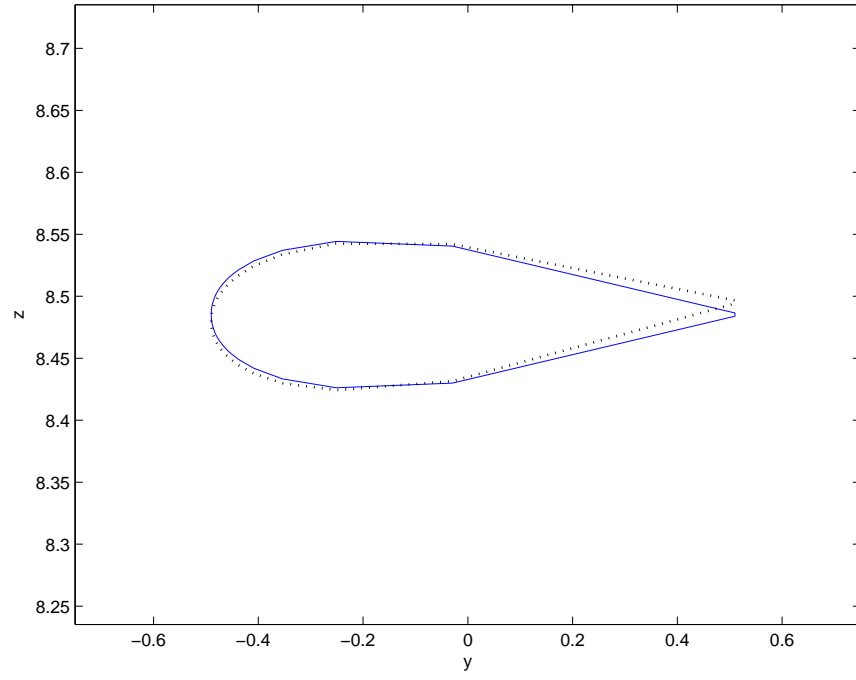


Figure 17: 3rd and 4th GVT structural modeshapes of stiff beam

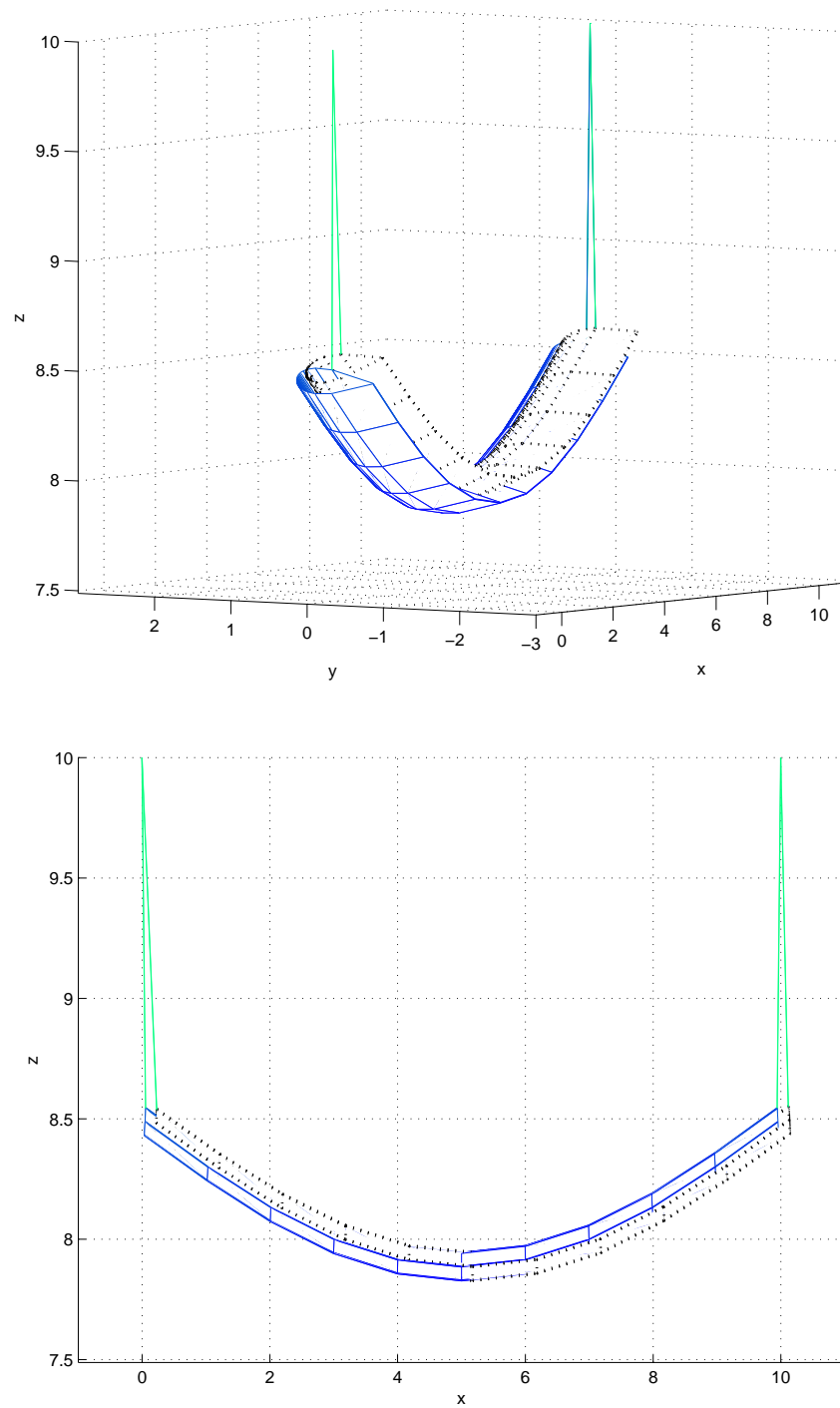


Figure 18: 1st and 2nd GVT rigid-body modeshapes of flexible beam

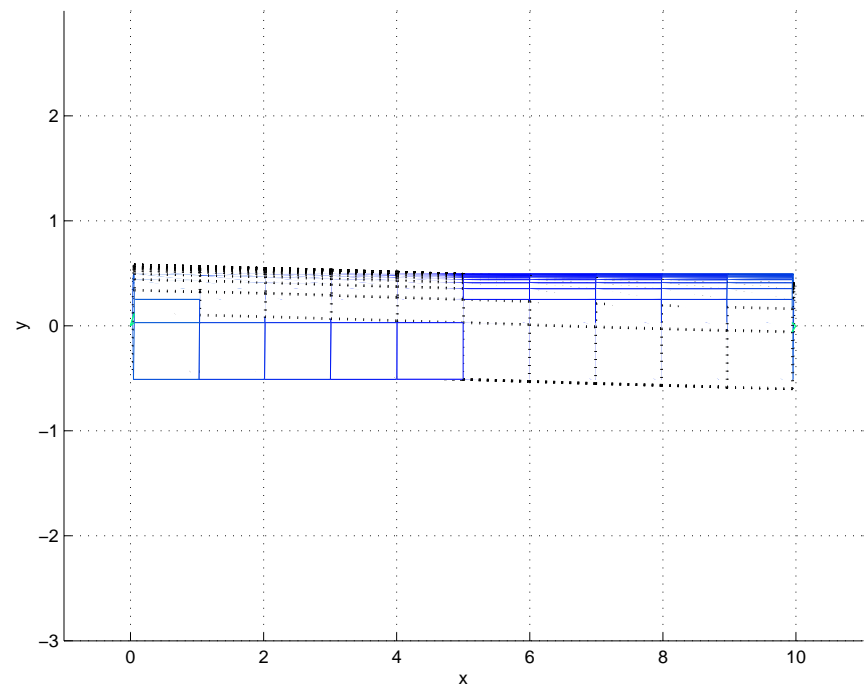
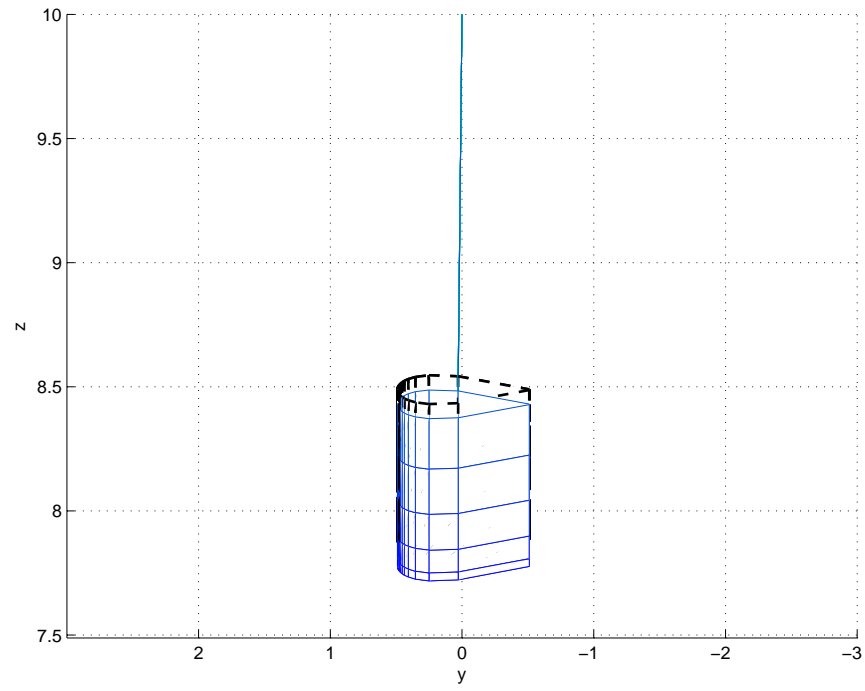


Figure 19: 3rd and 4th GVT rigid-body modeshapes of flexible beam

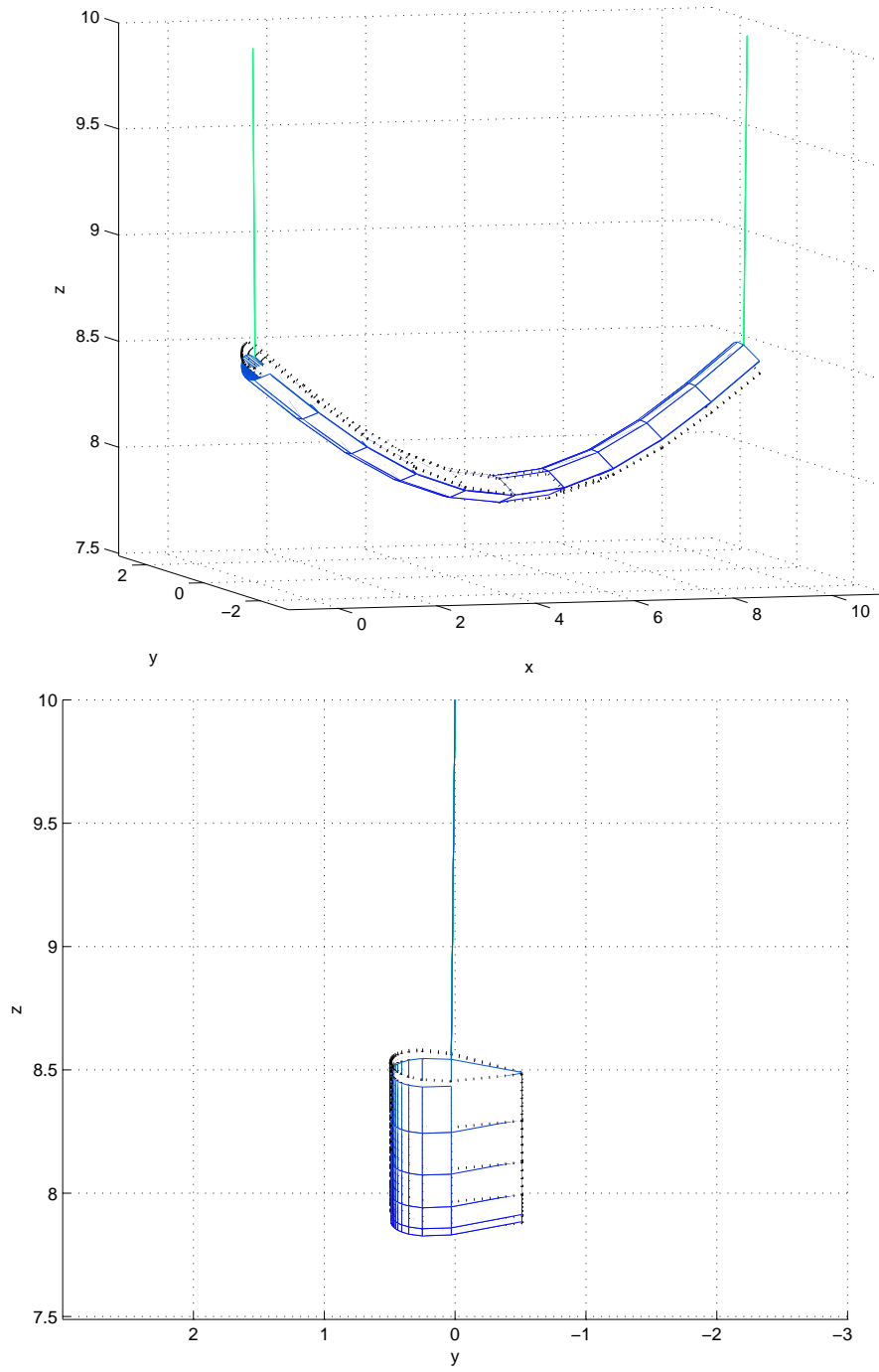


Figure 20: 5th and 6th GVT rigid-body modeshapes of flexible beam

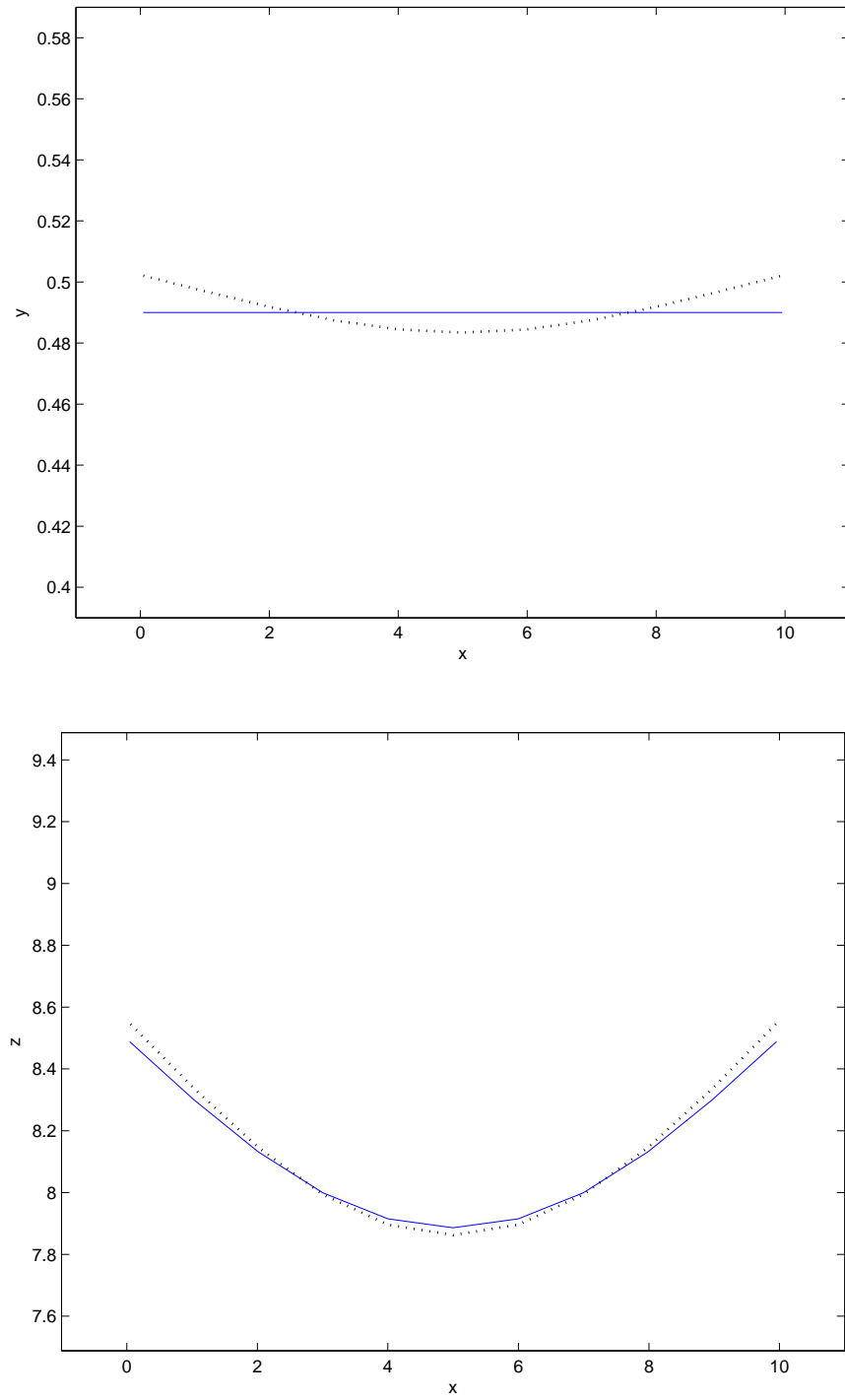


Figure 21: 1st and 2nd GVT structural modes of flexible beam

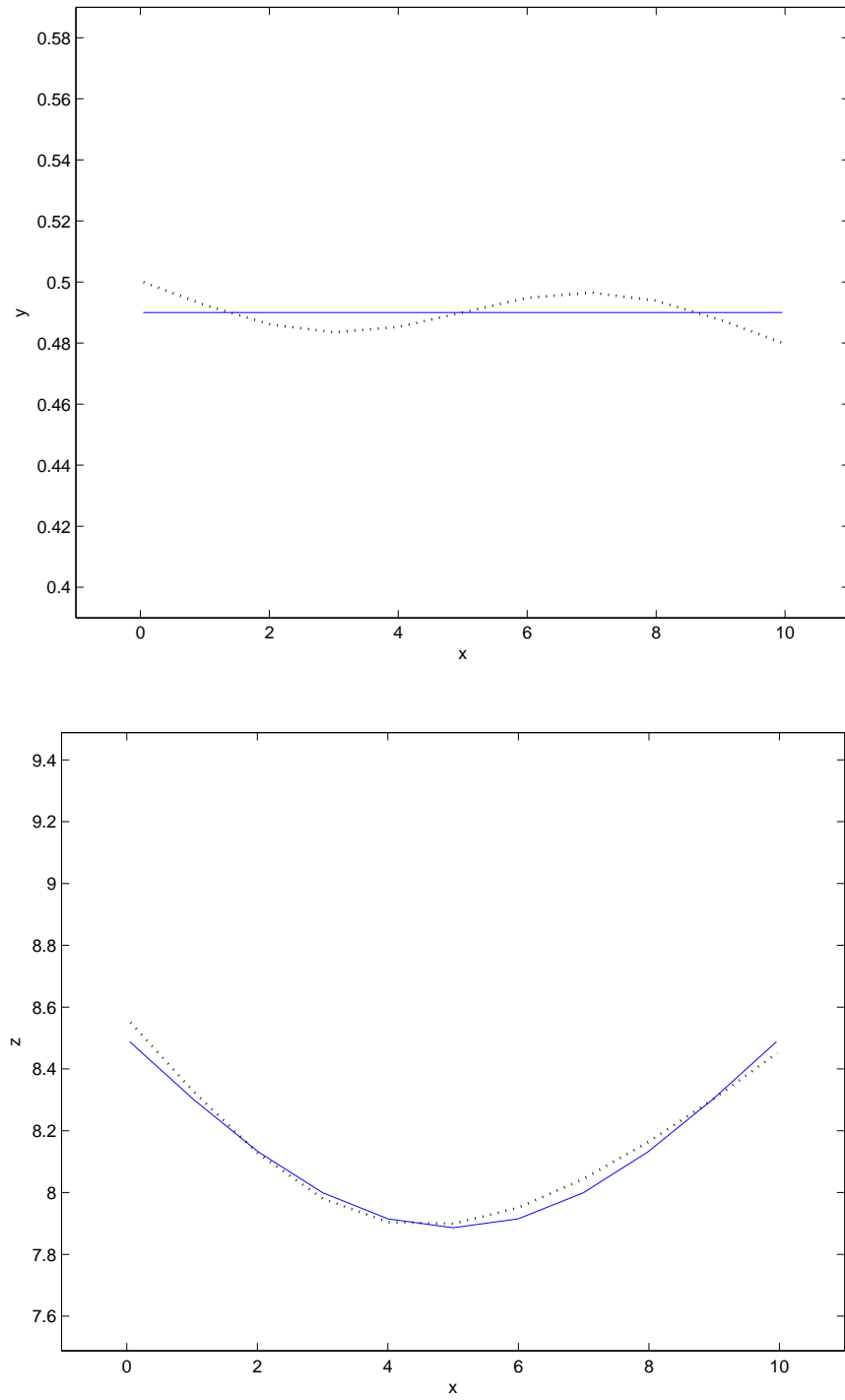


Figure 22: 3rd and 4th GVT structural modeshapes of flexible beam

Table 9: Four lowest GVT structural modes of the free-free flexible beam simulated by NATASHA

Eigenvalues	Description
$0 \pm 10.377 i$	1 st symm. structural bending mode w.r.t \mathbf{n}_3
$0 \pm 10.377 i$	1 st symm. structural bending mode w.r.t \mathbf{n}_2
$0 \pm 30.689 i$	1 st anti-symm. structural bending mode w.r.t \mathbf{n}_3
$0 \pm 30.689 i$	1 st anti-symm. structural bending mode w.r.t. \mathbf{n}_2

4.4 Modal Characteristics of a Highly Flexible Beam for Different Bungee Cord Locations

This parametric study is motivated by the fact that the shape of highly flexible flying wing in GVT will be quite different according to the locations of points to which bungee cords are connected. The study looks at different bungee cord locations to observe any differences in modal characteristics.

Case 1 is the case in which bungee cords are attached to each tip of the beam and Case 5 is the case in which bungee cords are attached close to mid-span. Cases 2 – 4 are intermediate cases between Cases 1 and 5. The static equilibrium of each case is shown in Figure 23. Depending on the locations of bungee cords, the deformed shapes of highly flexible beam in GVT are very different.

Table 11 shows the ten lowest eigenvalues of Cases 1 – 5 of flexible beams. Values for the four lowest eigenvalues of stiff beams are added for comparison. The relative difference of four lowest elastic modes for cases 1 – 5 with respect to those of the free-free flexible beam simulated by NATASHA are shown in Figure 24. The horizontal axis corresponds to the case numbers ($x = 1$ indicates Case 1). Figure 25 is an equivalent graph for stiff beam. This result shows that the shape of the flexible beam determined by the location to which bungee cords are attached in GVT affects the modal characteristics. The modal frequencies of the U shape and inverted U shape deviate from the least deformed case (Case 3). Some of the structural modes such as 1st symmetric bending and 1st torsional modes are more affected by either the deformed shape or a boundary condition due to bungee cords than are other modes. To determine that, the model with linear spring ($k = 20$ N/m) is simulated especially for Cases 1, 3, and 5. The results are given in Table 12. The eigenvalue for 1st symmetric bending mode in Case 1 changes from $\pm 12.582 i$ to $\pm 10.409 i$ from lowering the bungee stiffness ($k = 20$ N/m), which indicates that if bungee cords are located at the point where the most displacement occurs, 1st symmetric bending mode will be different from the solution for the free-free beam ($\pm 10.096 i$). The relative difference of 1st symmetric bending mode for Case 1 is still the largest among them. However, even in the model with the linear spring, 1st torsional mode in Cases 1 and 3 doesn't change much, from $\pm 90.817 i$ to

$\pm 90.419 i$ and $\pm 97.895 i$ to $\pm 97.880 i$, respectively. The one for Case 3 also doesn't change much, from $\pm 100.23 i$ to $\pm 100.19 i$, and is the closest to the analytical solution ($\pm 99.551 i$). It indicates that the U and inverted U shape tend to lower the 1st torsional frequency. For a stiff beam, the difference among the four lowest structural modes for each case is not very noticeable in Figure 25.

Table 10: Beam and bungee cord properties for “Different Bungee Cord Locations”

parameters		values	units
m	(mass per unit length)	10	kg/m
ℓ	(span of wing)	10	m
k	(bungee stiffness)	2000	N/m
		flexible	stiff
GJ	(Torsional stiffness)	1.0×10^4	1.0×10^6
EI_2	(Vertical Bending stiffness)	2.0×10^4	2.0×10^6
EI_3	(Chordwise Bending stiffness)	4.0×10^6	1.0×10^8

Table 11: Eigenvalues of Cases 1 – 5 with four lowest eigenvalues of flexible and stiff beams
< Flexible beam >

Eigenmode	Case 1	Case 2	Case 3	Case 4	Case 5
Swing (n_1)	$\pm 2.2574 i$	$\pm 2.4468 i$	$\pm 2.5309 i$	$\pm 1.8278 i$	$\pm 0.9163 i$
Swing (n_2)	$\pm 2.6316 i$	$\pm 2.6313 i$	$\pm 2.6312 i$	$\pm 2.4791 i$	$\pm 1.3353 i$
Plunging	$\pm 2.9358 i$	$\pm 3.3532 i$	$\pm 2.7378 i$	$\pm 2.5110 i$	$\pm 2.4492 i$
Twisting	$\pm 4.5561 i$	$\pm 3.6493 i$	$\pm 3.5888 i$	$\pm 2.6593 i$	$\pm 2.6425 i$
Rolling	$\pm 6.0353 i$	$\pm 5.0162 i$	$\pm 3.7530 i$	$\pm 3.5289 i$	$\pm 3.3556 i$
Pitching	$\pm 12.082 i$	$\pm 10.823 i$	$\pm 10.161 i$	$\pm 10.339 i$	$\pm 10.807 i$
1 st sym. bending (n_2)	$\pm 12.582 i$	$\pm 10.951 i$	$\pm 10.583 i$	$\pm 10.553 i$	$\pm 10.860 i$
1 st anti-sym. bending (n_2)	$\pm 29.326 i$	$\pm 28.392 i$	$\pm 28.480 i$	$\pm 28.725 i$	$\pm 28.526 i$
2 nd sym. bending (n_2)	$\pm 57.444 i$	$\pm 56.919 i$	$\pm 57.115 i$	$\pm 57.003 i$	$\pm 56.944 i$
1 st torsional	$\pm 90.817 i$	$\pm 98.260 i$	$\pm 100.23 i$	$\pm 98.872 i$	$\pm 97.895 i$

< Stiff beam >

1 st sym. bending (n_2)	$\pm 101.23 i$	$\pm 101.04 i$	$\pm 100.97 i$	$\pm 100.99 i$	$\pm 101.04 i$
1 st anti-sym. bending (n_2)	$\pm 283.17 i$	$\pm 283.07 i$	$\pm 283.08 i$	$\pm 283.11 i$	$\pm 283.09 i$
2 nd sym. bending (n_2)	$\pm 569.20 i$	$\pm 569.15 i$	$\pm 569.16 i$	$\pm 569.16 i$	$\pm 569.15 i$
1 st sym. bending (n_3)	$\pm 714.06 i$	$\pm 713.96 i$	$\pm 713.92 i$	$\pm 713.93 i$	$\pm 713.96 i$

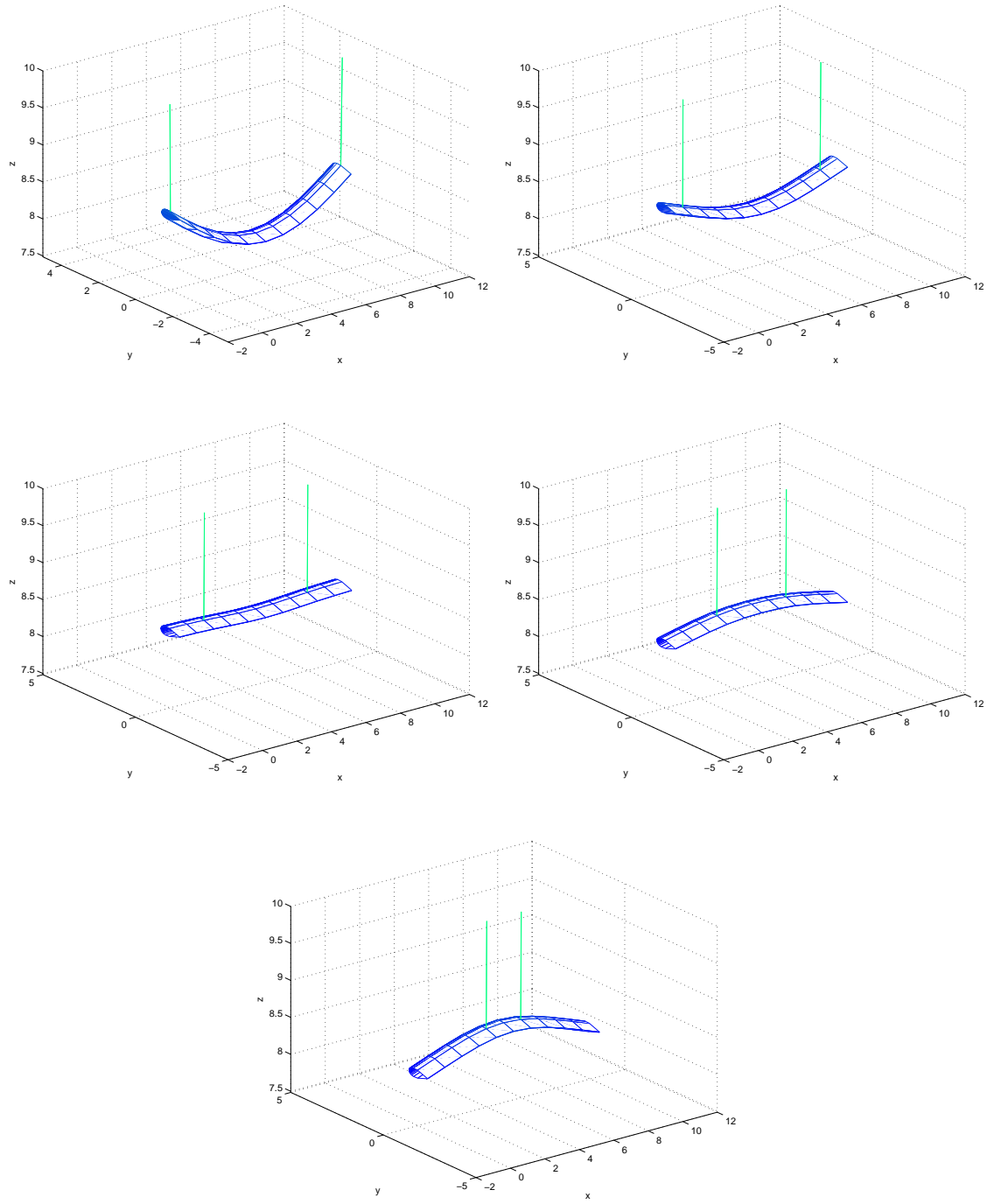


Figure 23: Static equilibria of Cases 1 – 5 (from top to bottom, from left to right, the case number increases as the bungee cord location moves to the mid-span)

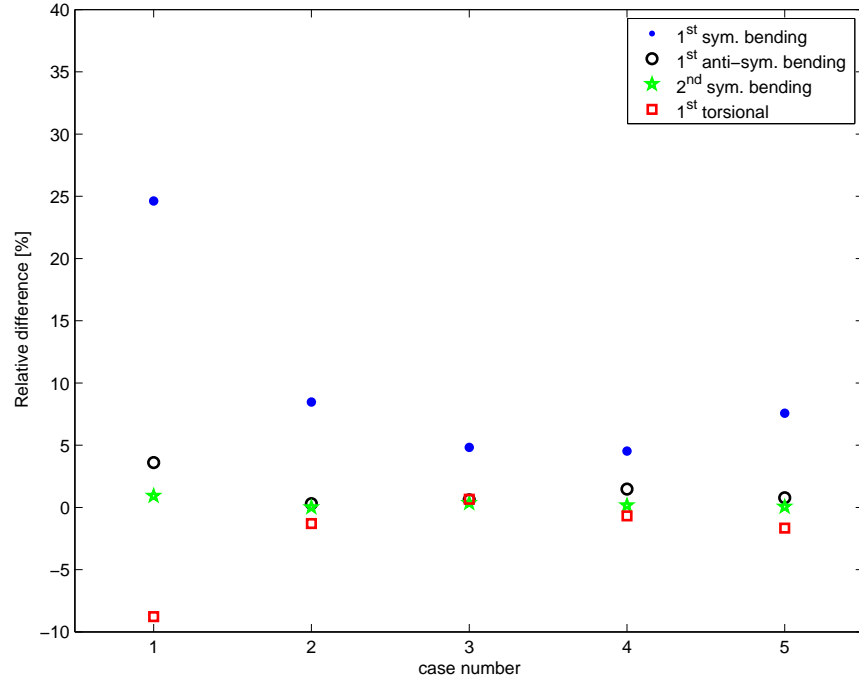


Figure 24: Relative difference of 4 lowest elastic modes of Cases 1 – 5 with respect to those of the free-free beam simulated by NATASHA. (x axis corresponds to the case number)

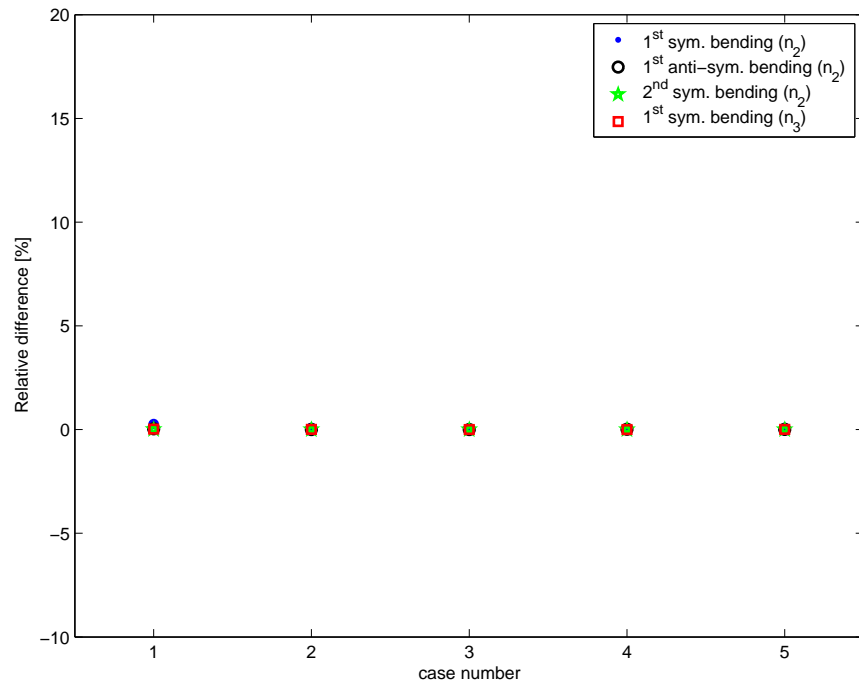


Figure 25: Relative difference of 4 lowest elastic modes for Cases 1 – 5 with respect to those of the free-free beam simulated by NATASHA. (x axis corresponds to the case number)

Table 12: Eigenvalues of cases 1, 3, and 5 with linear spring, and of the free-free flexible beam simulated by NATASHA

Eigenmode	Case 1	Case 3	Case 5	free-free beam
1 st sym. bending (n_2)	$\pm 10.409\ i$	$\pm 10.195\ i$	$\pm 10.120\ i$	$\pm 10.096\ i$
1 st anti-sym. bending (n_2)	$\pm 28.382\ i$	$\pm 28.327\ i$	$\pm 28.309\ i$	$\pm 28.307\ i$
2 nd sym. Bending (n_2)	$\pm 56.942\ i$	$\pm 56.912\ i$	$\pm 56.893\ i$	$\pm 56.915\ i$
1 st torsional	$\pm 90.419\ i$	$\pm 100.19\ i$	$\pm 97.880\ i$	$\pm 99.551\ i$

4.5 *Modal Characteristics of Flying Wing and Conventional Configurations*

For the purpose of comparing their features, a flying wing and conventional aircraft configurations are considered. For the flying wing, the payload is located at mid-span which corresponds to the total mass of fuselage for the conventional aircraft configuration. The static equilibrium of each case is shown in Figure 26. For simplicity the horizontal tail of the conventional aircraft is replaced by a concentrated mass at the tail end of the fuselage. The properties of wing, fuselage, and bungees are given in Table 13. (Bungee 1 and 2 are attached to each wing tip, and bungee 3 is attached to fuselage tip for conventional configuration.)

The GVT rigid-body modes (in which the beam behaves almost like a rigid body) in the flying wing configuration, such as plunging, twisting, pitching, rolling, and two swing modes, are quite similar to Figures 18 – 20 in the previous parametric study “4.3 Modal Characteristics of stiff and flexible beams.” Figures 27 – 28 show the four lowest structural modes: 1st symmetric, 1st anti-symmetric bending, and two torsional modes. (Counterparts of the conventional ones are Figures 29 – 33.) The associated eigenvalues with mode descriptions are given in Tables 14 and 15.

In the conventional aircraft configuration, some of the GVT rigid-body modes match those of flying wing configuration, and the types of the four lowest elastic modes are same in both cases. However the fuselage, tip mass, the additional bungee cord at the tip lead to an unusual GVT rigid-body mode that can be described as “pitching about the tail” The fuselage inertia and tail mass also lead to some differences in the structural modes. The fuselage inertia and tail mass will tend to lower the wing torsional mode in same phase between right and left tips. Due to the relatively short fuselage length, however, no structural modes of the fuselage appear among lowest structural modes.

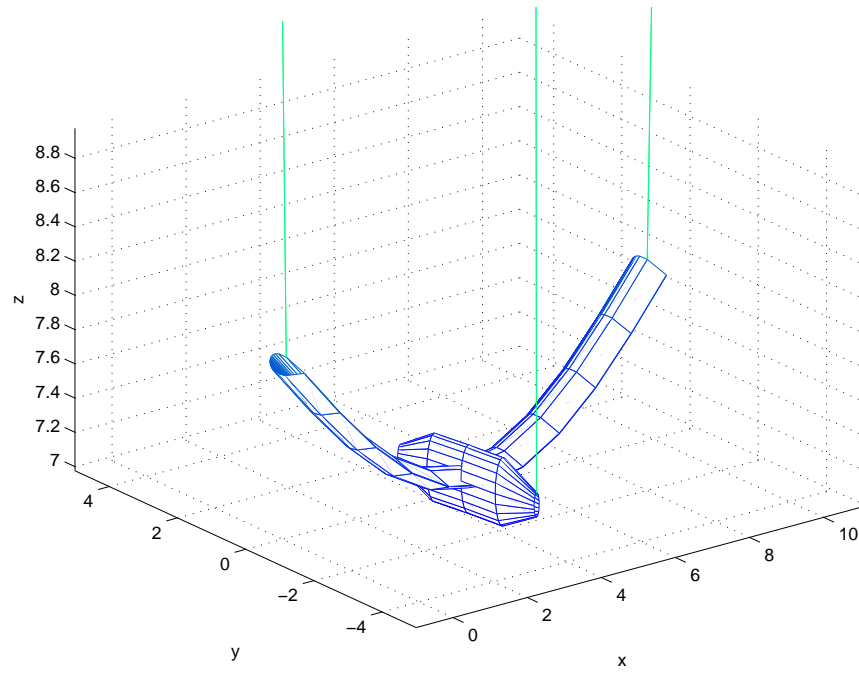
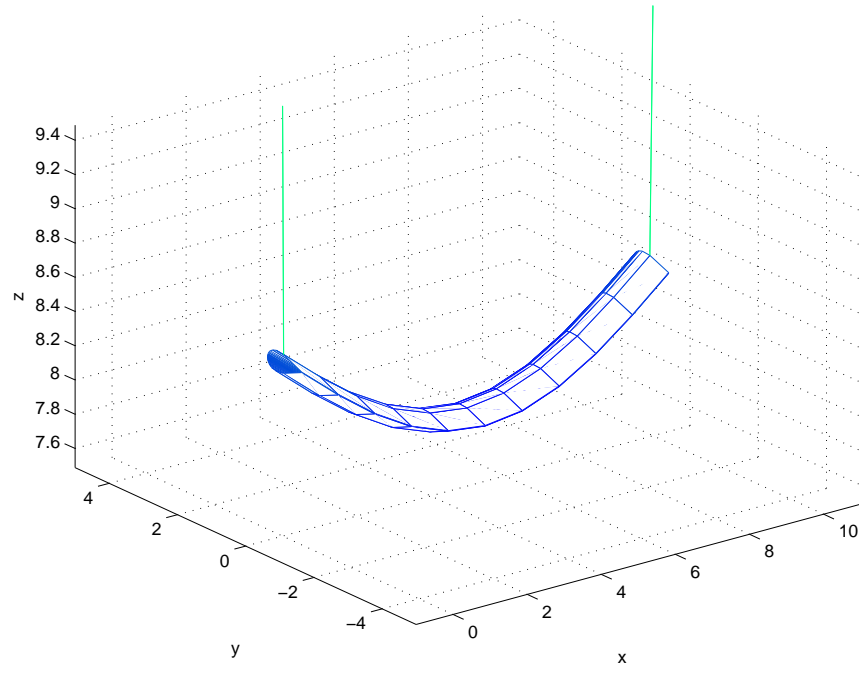


Figure 26: 3D plot of GVT static equilibria of flying wing and conventional configuration

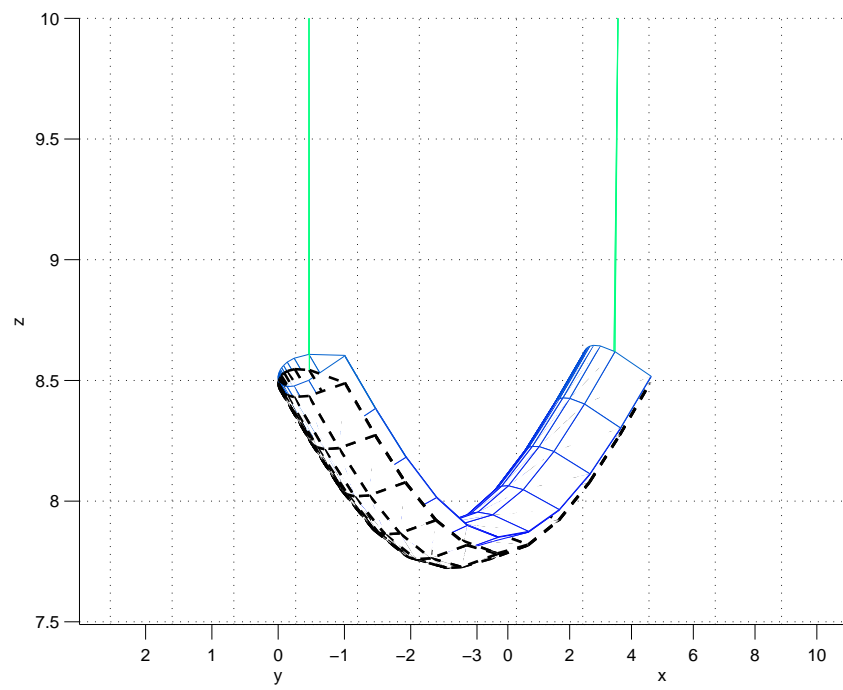
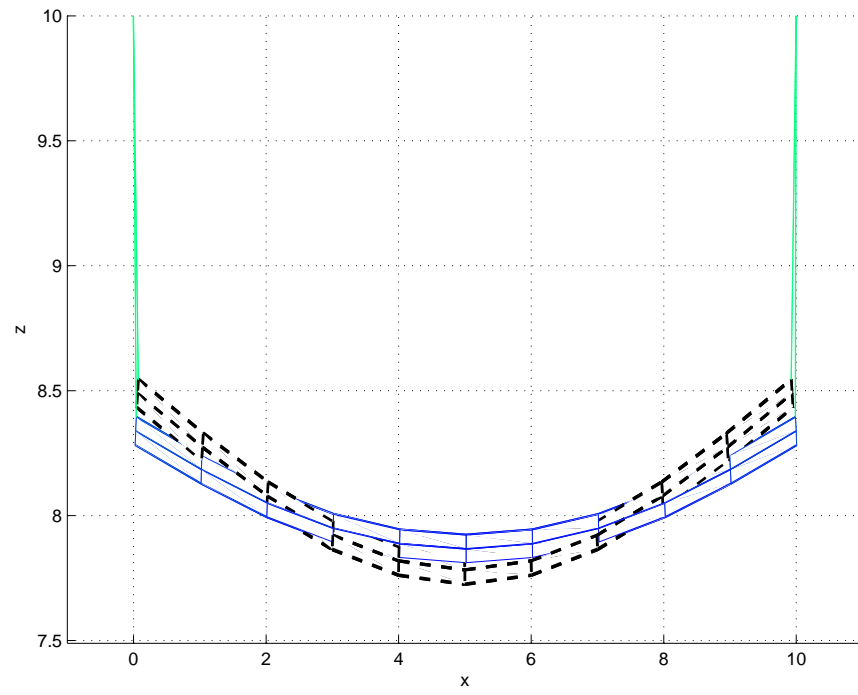


Figure 27: 1st and 2nd GVT structural modeshapes of flying wing configuration

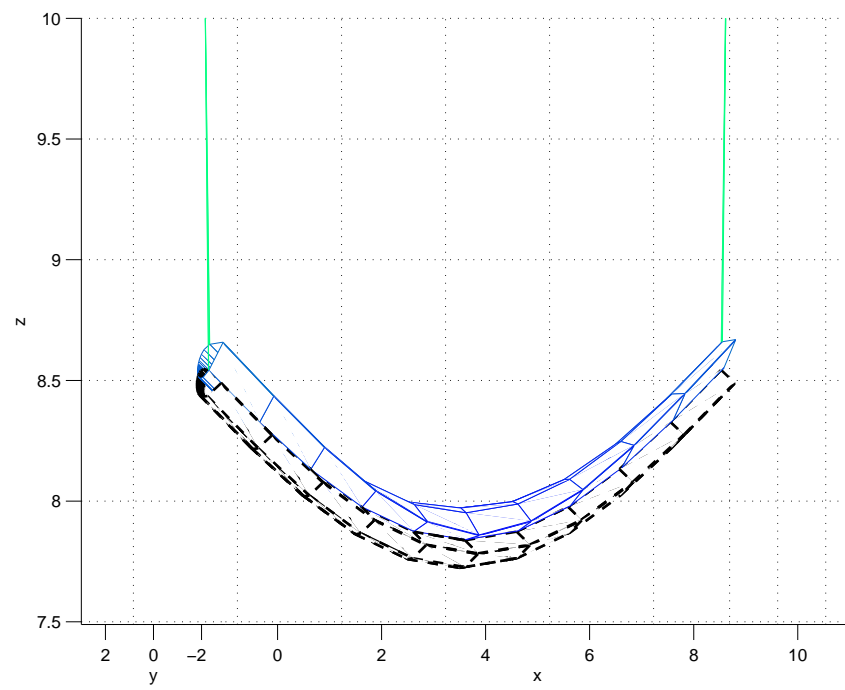
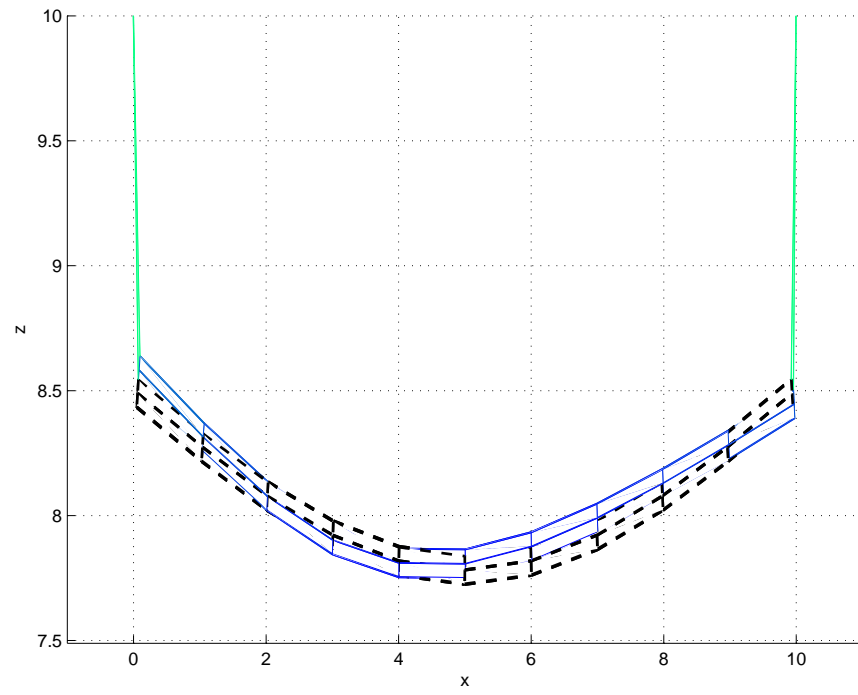


Figure 28: 3rd and 4th GVT structural modeshapes of flying wing configuration

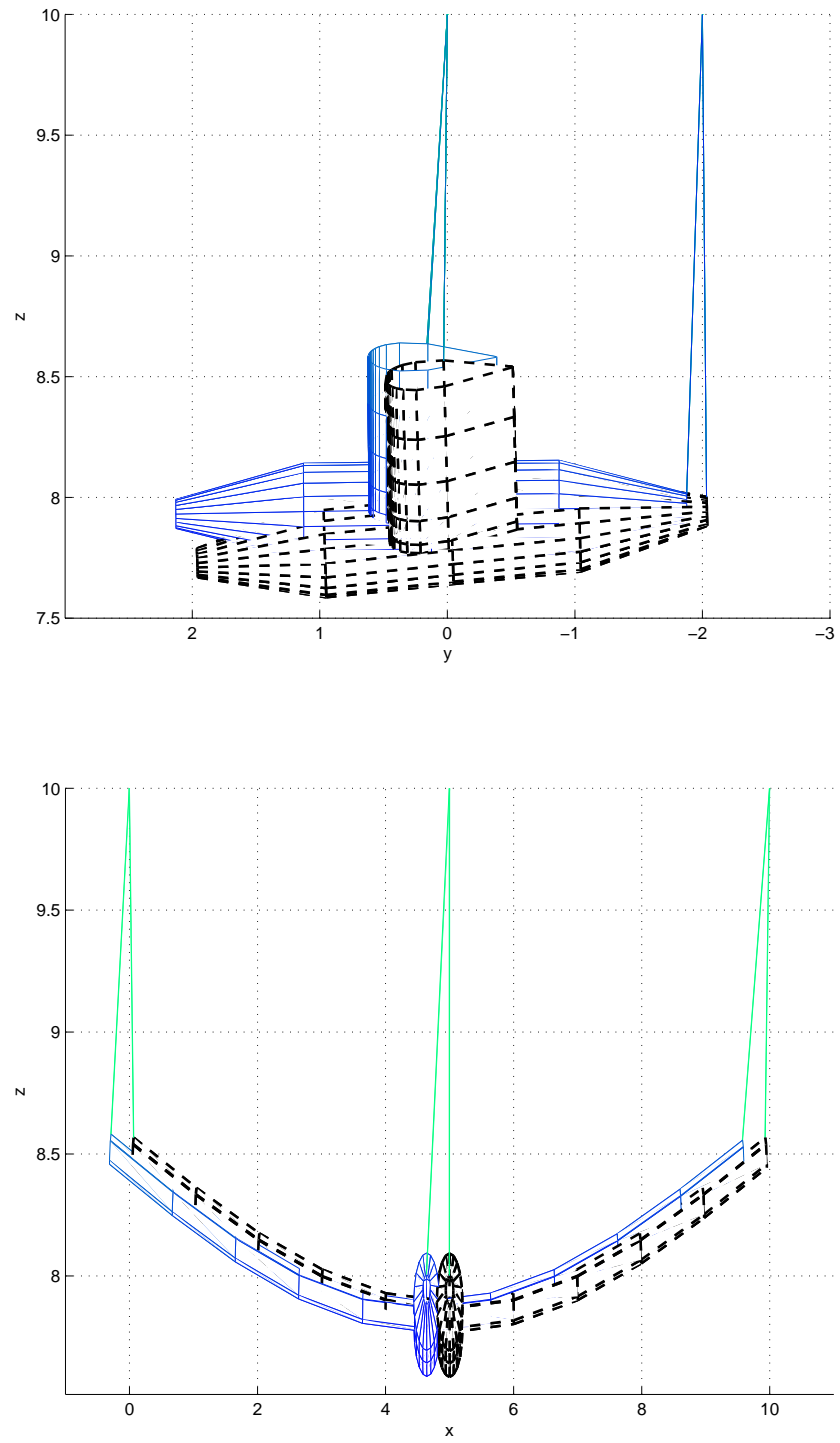


Figure 29: 1st and 2nd GVT rigid-body modeshapes of conventional configuration

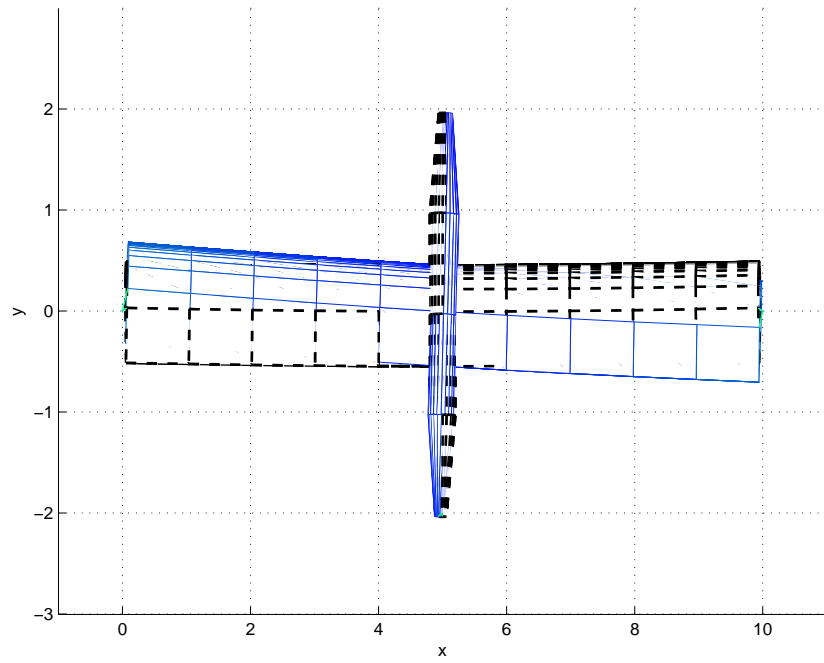
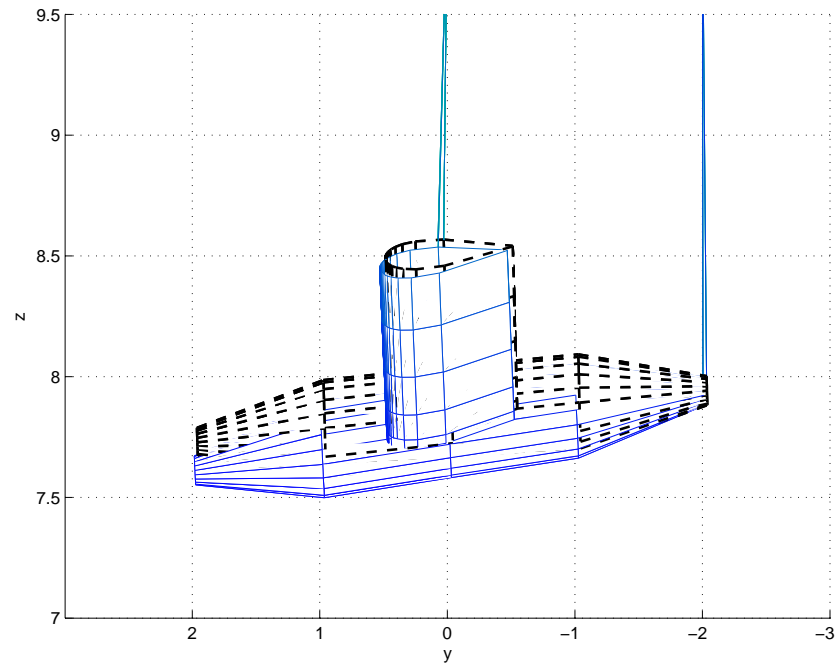


Figure 30: 3rd and 4th GVT rigid-body modeshapes of conventional configuration

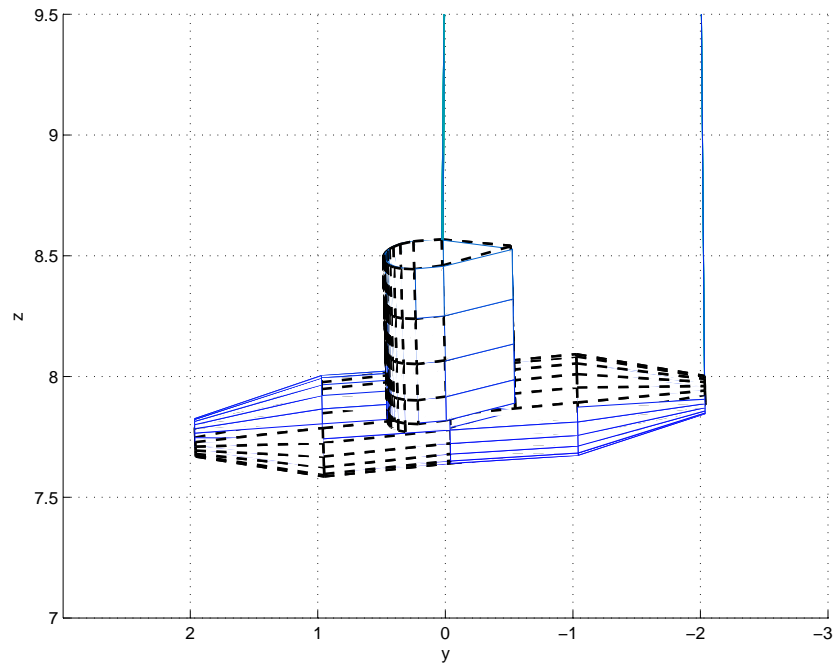
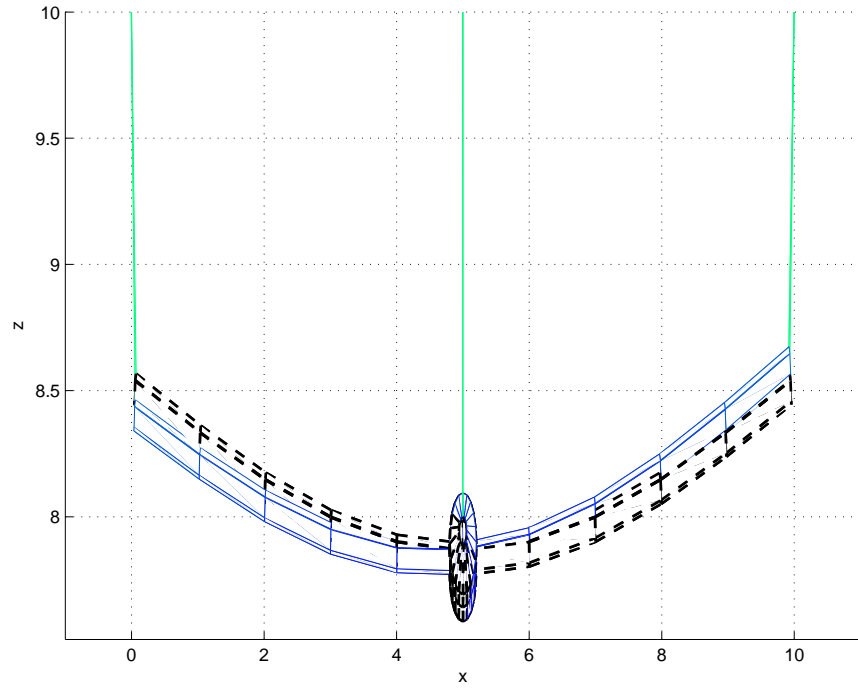


Figure 31: 5th and 6th GVT rigid-body modeshapes of conventional configuration

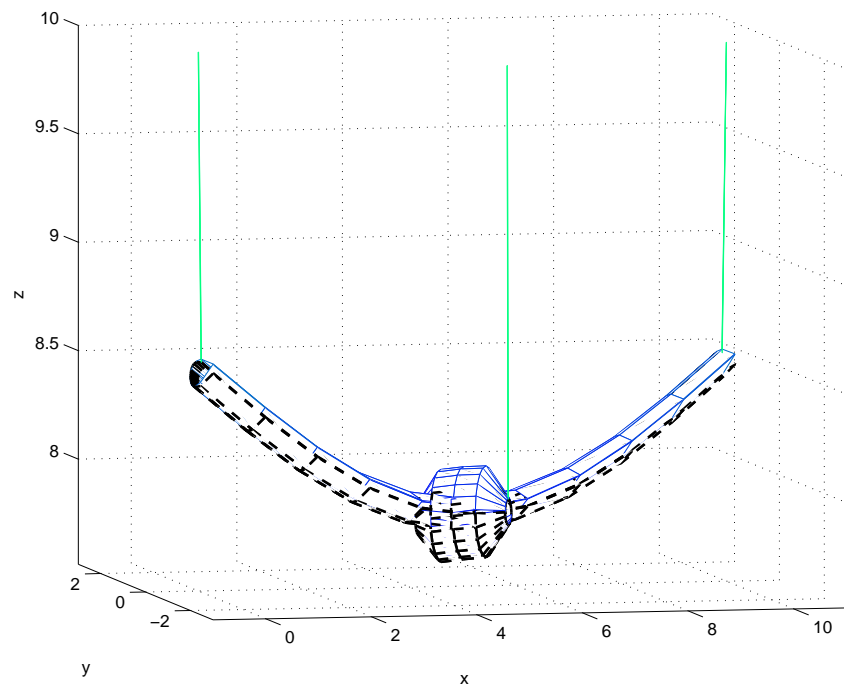
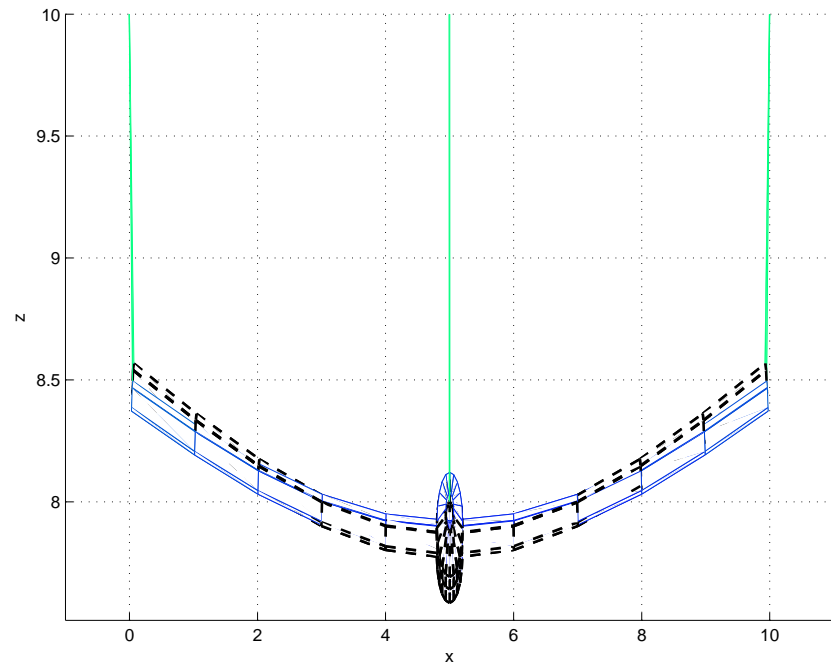


Figure 32: 1st and 2nd GVT structural modeshapes of conventional configuration

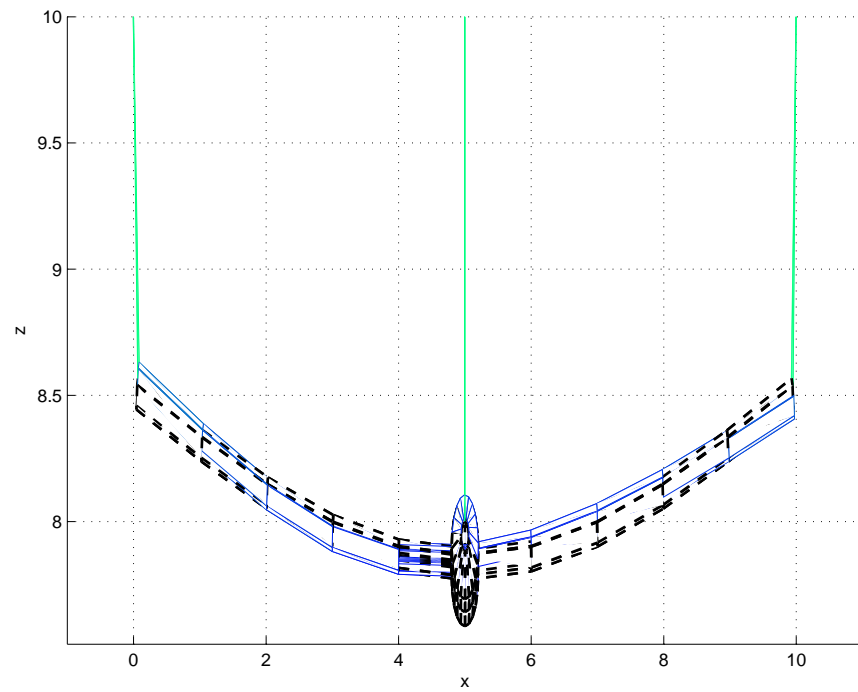
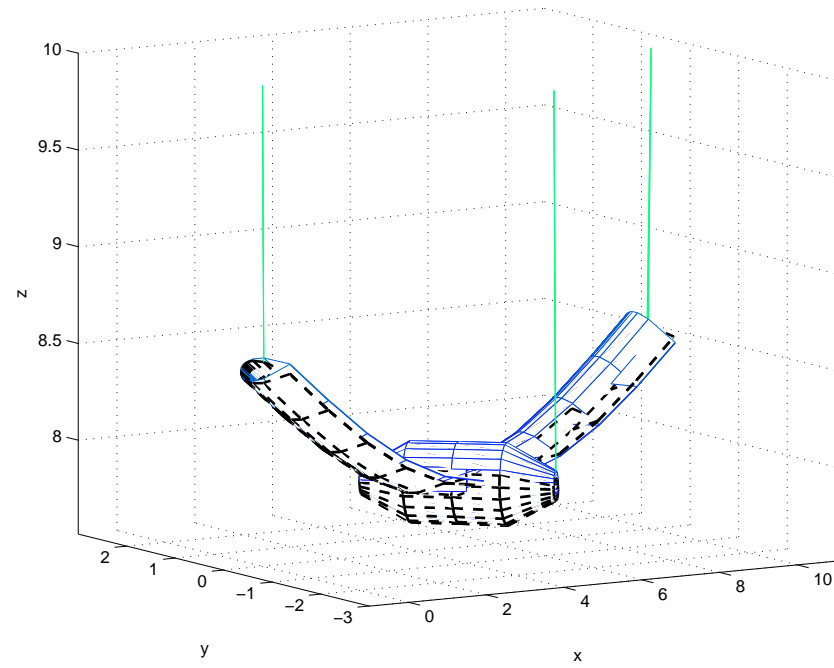


Figure 33: 3rd and 4th GVT structural modeshapes of conventional configuration

Table 13: Beam and bungee cord properties

property	wing	fuselage	units
m (mass per unit length)	7	7	kg/m
ℓ (span of beam)	10	4	m
GJ (Torsional stiffness)	1.0×10^4	1.0×10^4	Nm ²
EI_2 (Vertical Bending stiffness)	2.0×10^4	2.0×10^4	Nm ²
EI_3 (Chordwise Bending stiffness)	4.0×10^6	4.0×10^6	Nm ²
	bungees 1, 2	bungee 3	
k (bungee stiffness)	2000	2850	N/m
ℓ_b (bungee natural length)	1	1.9	m

Table 14: Ten lowest GVT modes and corresponding eigenvalues of flying wing configuration

Eigenvalues	Description
$0 \pm 2.1465 i$	swing mode w.r.t \mathbf{n}_1 + plunging mode
$0 \pm 2.6319 i$	swing mode w.r.t \mathbf{n}_2
$0 \pm 2.7946 i$	plunging mode
$0 \pm 5.4670 i$	twisting mode
$0 \pm 7.1812 i$	pitching mode
$0 \pm 7.2576 i$	rolling mode
$0 \pm 13.425 i$	1 st symmetric bending mode w.r.t \mathbf{n}_2
$0 \pm 33.192 i$	torsional mode with 180° phase delay between right and left tips
$0 \pm 37.891 i$	1 st anti-symmetric vertical bending mode w.r.t \mathbf{n}_2
$0 \pm 49.040 i$	torsional mode with same phase between right and left tips

Table 15: Ten lowest GVT modes and corresponding eigenvalues of conventional aircraft configuration

Eigenvalues	Description
$\pm 2.3710 i$	swing mode w.r.t \mathbf{n}_1
$\pm 2.6261 i$	swing mode w.r.t \mathbf{n}_2
$\pm 3.3024 i$	pitching about tail
$\pm 5.1714 i$	twisting mode
$\pm 7.4294 i$	rolling mode
$\pm 11.896 i$	pitching mode
$\pm 14.298 i$	1 st symmetric wing bending mode w.r.t \mathbf{n}_2
$\pm 30.961 i$	wing torsional mode with same phase between right and left tips
$\pm 32.925 i$	wing torsional mode with 180° phase delay between right and left tips
$\pm 35.340 i$	1 st anti-symmetric wing vertical bending mode w.r.t \mathbf{n}_2

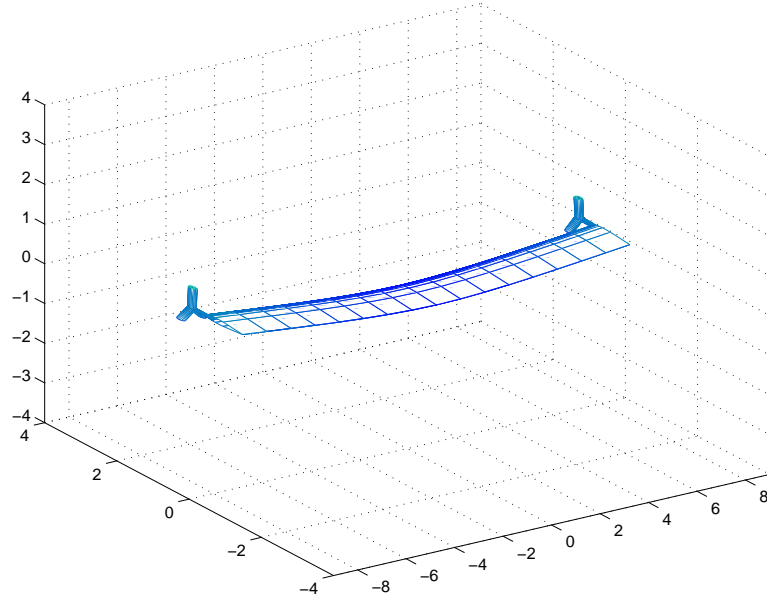


Figure 34: Trim configuration of highly flexible flying wing aircraft with two Engine/Propeller systems

4.6 Time Simulation of $NATASHA_{WF}$

$NATASHA_{WF}$ can simulate the dynamic behavior of propeller-driven HALE aircraft. It can confirm the whirl flutter instability by its nonlinear dynamic simulation especially if the eigenanalysis indicates that the given configuration has unstable modes. First, it determines the trim condition of the HALE aircraft with a three-bladed Engine/Propeller system or an equivalent three-bladed Engine/Propeller system for the two-bladed case. Then it performs an eigenanalysis about the trim condition. In certain trim condition, it might have one or more unstable eigenvalues. Three possible dynamic behaviors are simulated in finite time: decaying, periodic oscillation, and divergent cases. The excitation level in time and the perturbation of the initial condition are determined by the level of the periodic airloads and associated eigenvectors from the eigenanalysis. Due to the computational demand, the time history of each case is only shown in finite time. Note that the nonlinear dynamic simulation might make an unstable mode appear to be stable for a finite time interval unless it is simulated for a long period time. Thus, Floquet analysis is needed for stability analysis.

The parameters for the reference configuration are given in Table 16. A left Engine/Propeller system is clamped to the wing and it rotates about the negative y direction. The right one is connected to the wing with pitch and yaw degree-of-freedom with stiffness (k_α and k_β) and it is rotating opposite to the one on the left. Both pylons are aligned to \mathbf{b}_2 (one of unit basis vectors of undeformed beam reference frame). One of the structural modes is unstable, with eigenvalues of $0.0555 \pm 5.3600 i$.

Figure 35 and 36 show the nonlinear dynamic simulation of a decaying case. The excitation force determined as half of periodic propeller airloads is applied to the right propeller hub center for first 0.2 seconds with perturbation on the initial condition.

Figure 37 and 38 show the nonlinear dynamic simulation of a divergent case. The excitation force determined as twice of periodic propeller airloads is applied to the right propeller hub center for first 2 seconds. The angle of attack and the tip transverse position are increasing in time in Figure 37. The pitch and yaw angles are also increasing in time in Figure 38.

Figure 39 and 40 show the nonlinear dynamic simulation of periodic oscillation case after increasing k_α and k_β as 600 Nm/rad, and EI_2 as 0.94×10^4 Nm². (The real part of the unstable eigenvalue becomes 0.002 .) The excitation force determined as half of periodic propeller airloads is applied to the right propeller hub center for first 0.5 seconds with a slight perturbation of the initial conditions. Wing and whirl motions reach a low frequency periodic oscillation in low frequency after the high frequency oscillations decay.

Table 16: Parameters for the reference configuration

parameters		values	units
m	(mass per unit length)	0.75	kg/m
$\hat{\mu}$	(payload at mid-span)	21	kg
ℓ	(length of the beam)	16	m
UU	(magnitude of aircraft forward velocity)	20	m/sec
phi	(flight path angle)	0	rad
GJ	(Torsional stiffness)	1.0×10^4	Nm ²
EI_2	(Vertical Bending stiffness)	0.9×10^4	Nm ²
EI_3	(Chordwise Bending stiffness)	4.0×10^6	Nm ²
k_α, k_β	(pitch and yaw stiffness)	300	Nm/rad
d	(diameter of propeller)	1	m
c_{blade}	(blade chord)	0.1	m

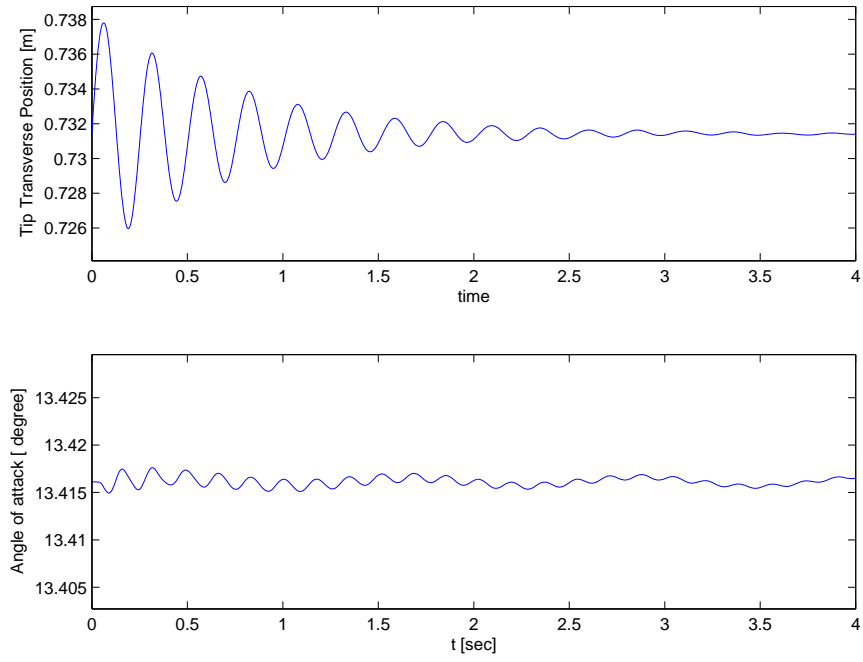


Figure 35: Time history of decaying tip transverse position and angle of attack

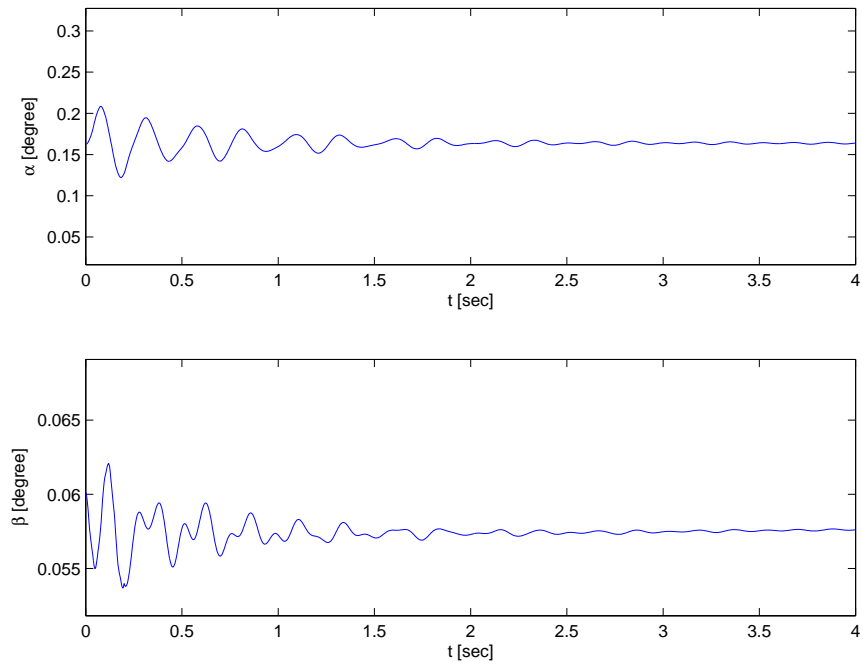


Figure 36: Time history of decaying pitch (α) and yaw angles (β)

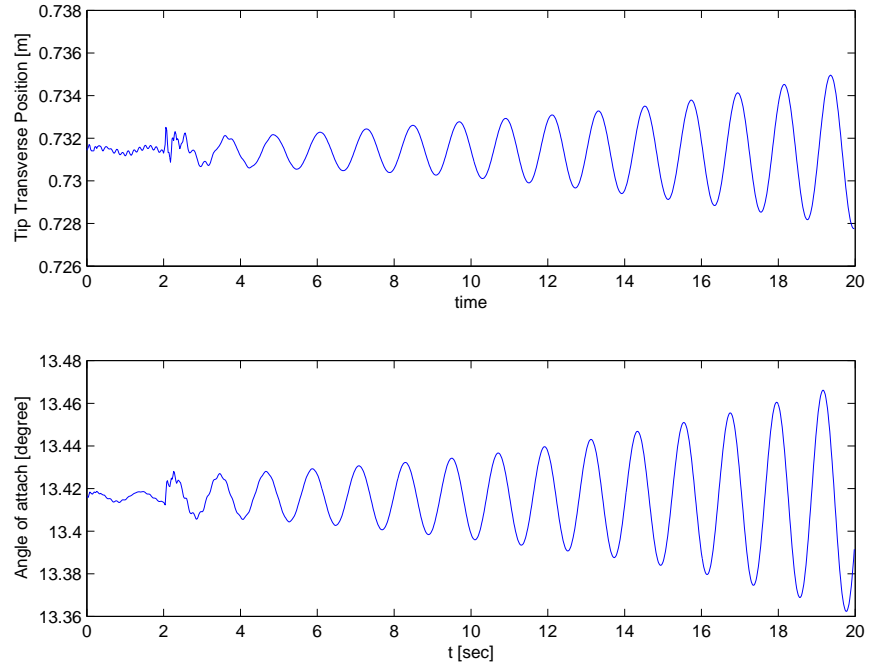


Figure 37: Time history of divergent tip transverse position and angle of attack

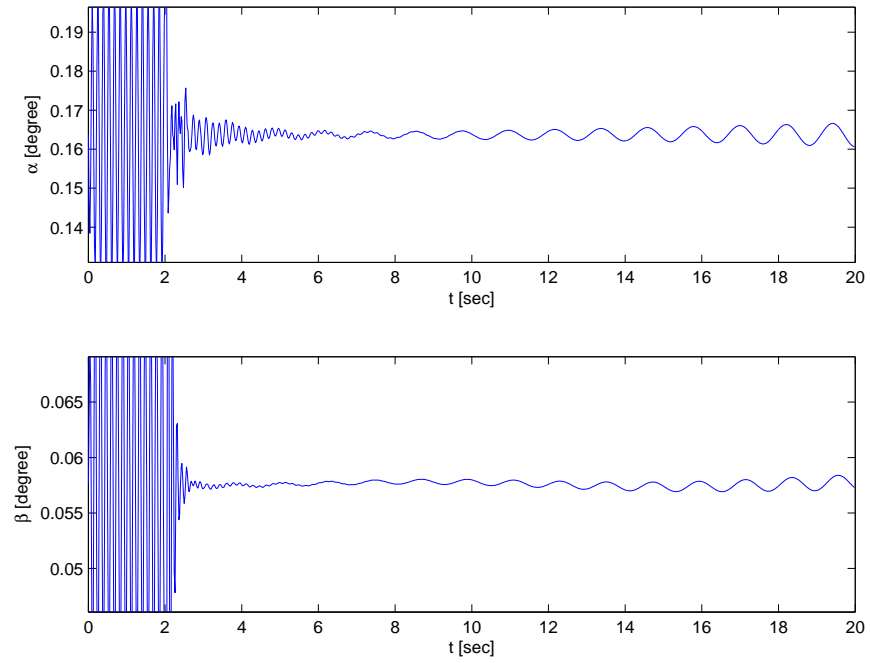


Figure 38: Time history of divergent pitch and yaw angles

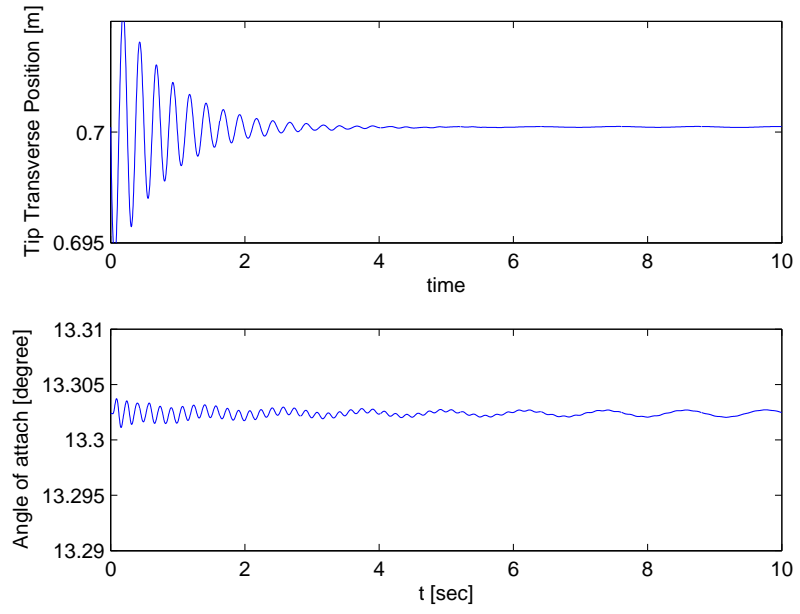


Figure 39: Time history of tip transverse position and angle of attack in periodic oscillation

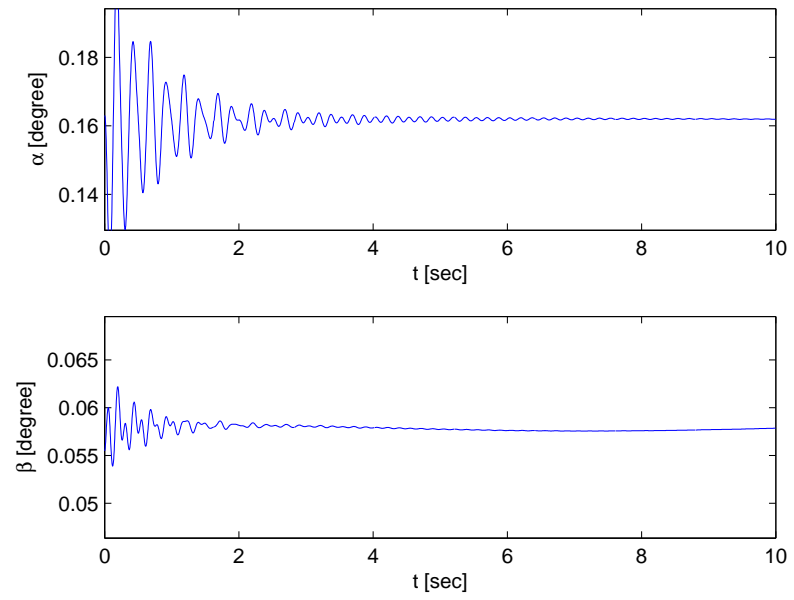


Figure 40: Time history of pitch and yaw angles in periodic oscillation

4.7 Periodic Inertia Effect

Before addressing other advanced analysis methodology, it needs to be investigated first whether the periodic inertia effect is dominant or not and when it becomes ignorable. The reason for this is that certain HALE aircraft use two-bladed propellers with a relatively small diameter. Even though they may have two-bladed propellers, they can be treated as an equivalent three-bladed case if the effect is ignorable.

Two- and three-bladed Engine/Propeller systems are considered to see the periodic inertia effect of two-bladed case on dynamic characteristics. First, the equivalent three-bladed case is run to determine the trim condition. Then a nonlinear dynamic simulation of the two-bladed case is run with the initial conditions taken from the trim solution of the three-bladed case. The preliminary Engine/Propeller analysis in Appendix B confirmed that the critical parameter that can lead to large differences in both dynamic behaviors is the length ratio R_ℓ (pylon length to propeller diameter).

The following assumptions are made for the simulation:

- Both cases have the same total blade mass.
- A powered rotation case is considered with constant propeller angular speed.
- The propeller airload is taken to be the same for both two- and three-bladed cases.
- Whether the dynamic behaviors of the two- and three-bladed cases are the same or not is determined by whether the time simulation of the two-bladed case 1) stays nearly periodic and 2) deviates from the trim states of three-bladed case.

Figure 41 shows the trace of the hub center of the two-bladed cases deviates from the trim states of equivalent three-bladed case. The length ratio ($R_\ell = 2.5$) is rather large with respect to the given pitch and yaw stiffness ($k_\alpha = k_\beta = 300$ Nm/rad). Therefore, the periodic inertia effect makes it diverge. (“*” is the trim condition of three-bladed case and “o” is an end point of simulation.) Another case is simulated after reduce the length ratio ($R_\ell = 2.2$) and increasing the stiffness ($k_\alpha = k_\beta = 600$ Nm/rad). The whirling motion

of the two-bladed Engine/Propeller system stay periodically around the trim solution of equivalent three-bladed case in finite time shown in Figure 42.

Figure 43 shows one of the boundary of certain HALE aircraft configuration. (The parameters are given in Table 17.) Inside the boundary, the periodic inertia effect is small, so it doesn't contribute much either the whirling or wing motion. However, beyond the boundary, the periodic inertia effect of the given two-bladed Engine/Propeller configuration should be considered to determine trim and stability characteristics because R_ℓ is relatively large, the dynamic behavior is dominated by the blade inertia properties and the off diagonal components in inertia matrix are not negligible. Floquet theory is thus needed. (The boundary in Figure 43 is determined with respect to different length ratios, and same pitch and yaw stiffnesses. The boundary will be changed if a configuration changes from the simulated configuration. For example, different wing properties such as mass per unit length and total length, and different flight condition such as aircraft forward speed and altitude, and etc can affect the boundary.)

Table 17: Parameters in “Periodic Inertia Effect”

parameters		values	units
m	(mass per unit length)	0.75	kg/m
ℓ	(length of the beam)	16	m
UU	(magnitude of aircraft forward velocity)	20	m/sec
phi	(flight path angle)	0	rad
$\hat{\mu}$	payload at midspan	25	kg
GJ	(Torsional stiffness)	1.0×10^4	Nm ²
EI_2	(Vertical Bending stiffness)	2.0×10^4	Nm ²
EI_3	(Chordwise Bending stiffness)	4.0×10^6	Nm ²
m_1	(pylon mass)	0.075	kg
m_2	(total blade mass)	0.15	kg
h_1	(pylon length)	0.6	m
d	(diameter of blade)	$= h_1 \times R_\ell$	m
R_ℓ	(length ratio)	$= \frac{d}{h_1}$	

Two things should be indicated here. First, if the pitch and yaw stiffnesses are relatively small, then the Engine/Propeller system is quite susceptible to the loads produced by periodic inertia terms or periodic airloads. Even though the trim states of wing do not change much from the periodic loads, the whirling motion can become divergent. Second, if

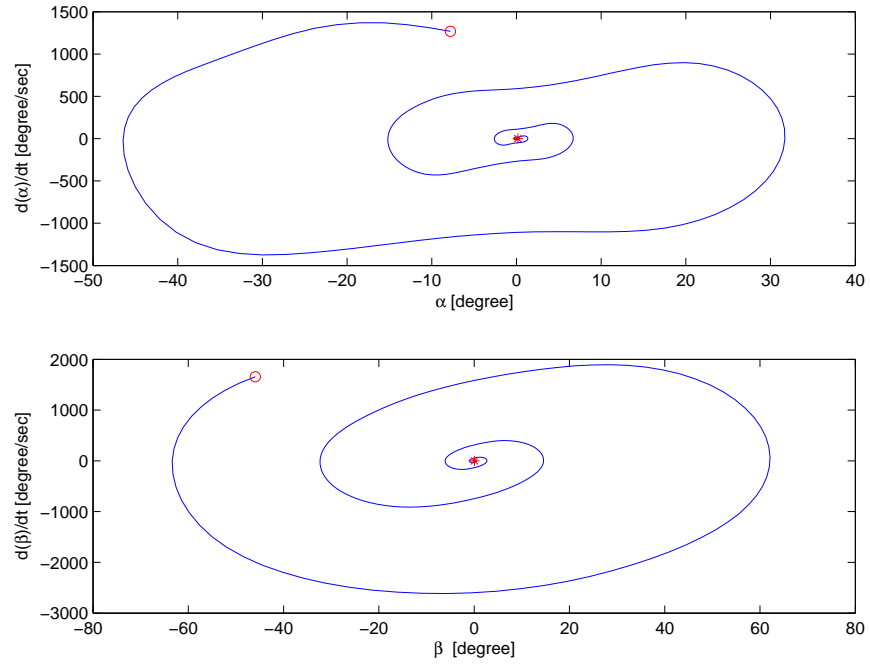


Figure 41: α vs $\dot{\alpha}$ and β vs $\dot{\beta}$ in phase plane in divergent case

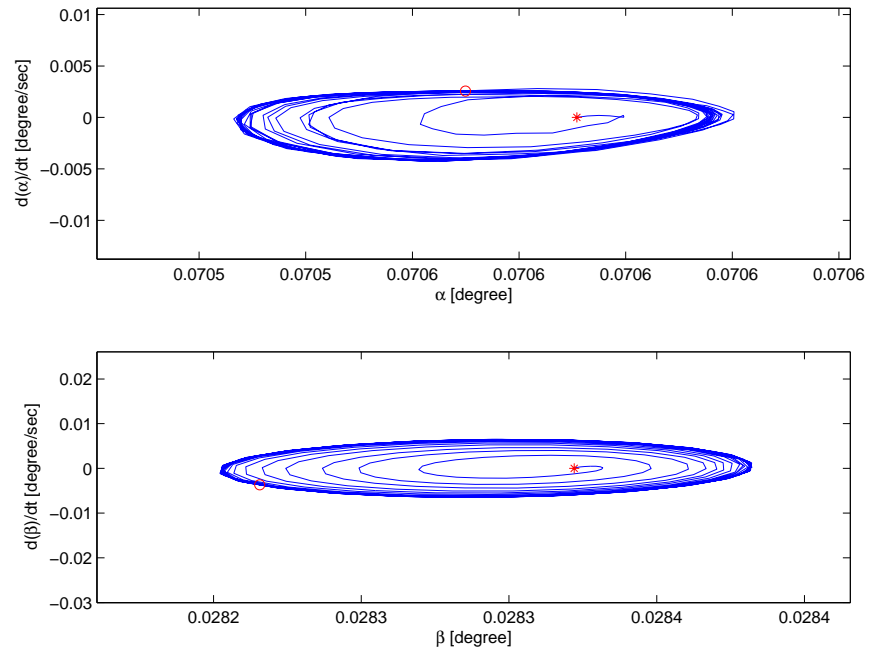


Figure 42: α vs $\dot{\alpha}$ and β vs $\dot{\beta}$ in phase plane in periodic oscillation

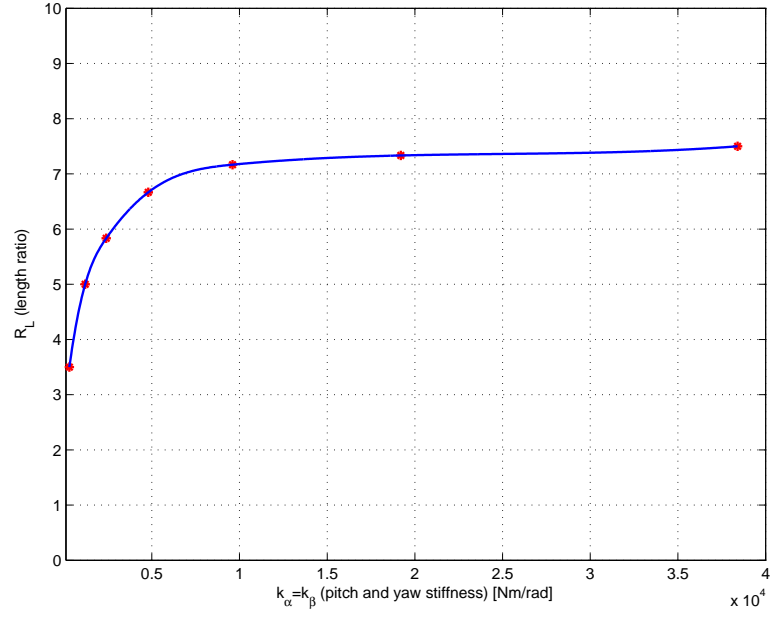


Figure 43: Boundary for whether two-bladed Engine/Propeller system can be approximated as equivalent three-bladed Engine/Propeller system

the pitch and yaw stiffness is relatively large, then the whirling motion oscillates very close to the trim states, but the vehicle can be excited by the periodic loads. In time, the aircraft can deviate from the trim condition. This fact motivates the next parametric study about periodic propeller airloads to see if the trim condition changes or not.

4.8 *Periodic Propeller Airloads*

In reality, the propeller side force and hub moments are periodic as a function of azimuth angle shown in Figures 44 – 45. For three- and four-bladed propeller systems, the periodicity is not quite noticeable. But for two-bladed case, the periodicity still exists. These figures are from the simulation when the angle of a pylon is 7° to the freestream. ($\omega_o = 36$ rad/sec, $d = 1$ m, $c_{\text{blade}} = 0.1$ m) Generally the periodicity increases as the angle between the pylon and the freestream increases due to the unsymmetry in propeller disk caused by the velocity component parallel to the propeller disk. For simplicity, when the trim condition is determined, the propeller airloads are assumed to be constant. It should then be verified whether or not the periodicity perturbs the trim condition determined by constant approximation on the propeller airloads. A time simulation can easily verify that if one evaluates the propeller airloads at each azimuth angle within a given time step and takes the trim condition as an initial condition. If the pitch and yaw stiffnesses are low, then it is more likely to be perturbed from the trim condition by the periodic side forces and moments. One of the reference result is taken from the previous parametric study. The reference configuration in two-bladed Engine/Propeller system is given in Table 18. The previous parametric study confirmed that the equivalent three-bladed case can substitute the two-bladed counterpart for this reference parameters.

Figures 46 and 47 show that the periodic propeller airloads do affect the trim condition, but the trim condition determined by constant approximation of propeller airloads stay periodic. Compared to the other wing airloads and gravity, the level of periodic propeller airload effect is relatively low, because for propeller-driven HALE aircraft, the propeller thrust level is mainly determined by the total drag of the wing, not by the total lift. It is not enough to make the trim states deviate from the values from the constant approximation. An additional case is investigated by reducing the payload at mid-span from 35 to 20 kg in order to make the periodic airload effect more influential. Figures 48 and 49 shows that the level of states in periodic oscillation increases. Roughly the pitch angle in periodic oscillation increases from 0.4° to 1° and the angle of attack in periodic oscillation increases from 0.02° to 0.8° . For other configurations, it should be verified whether it stays inside

the permissible range from the trim condition determined by the constant approximation if it uses two- or three-bladed Prop/Eng system.

Table 18: Parameters in “Periodic Propeller Airloads”

parameters		values	units
m	(mass per unit length)	0.75	kg/m
ℓ	(length of the beam)	16	m
UU	(magnitude of aircraft forward velocity)	20	m/sec
phi	(flight path angle)	0	rad
$\hat{\mu}$	payload at midspan	35	kg
GJ	(Torsional stiffness)	1.0×10^4	Nm ²
EI_2	(Vertical Bending stiffness)	2.0×10^4	Nm ²
EI_3	(Chordwise Bending stiffness)	4.0×10^6	Nm ²
m_1	(pylon mass)	0.075	kg
m_2	(total blade mass)	0.15	kg
h_1	(pylon length)	0.6	m
d	(diameter of blade)	1	m

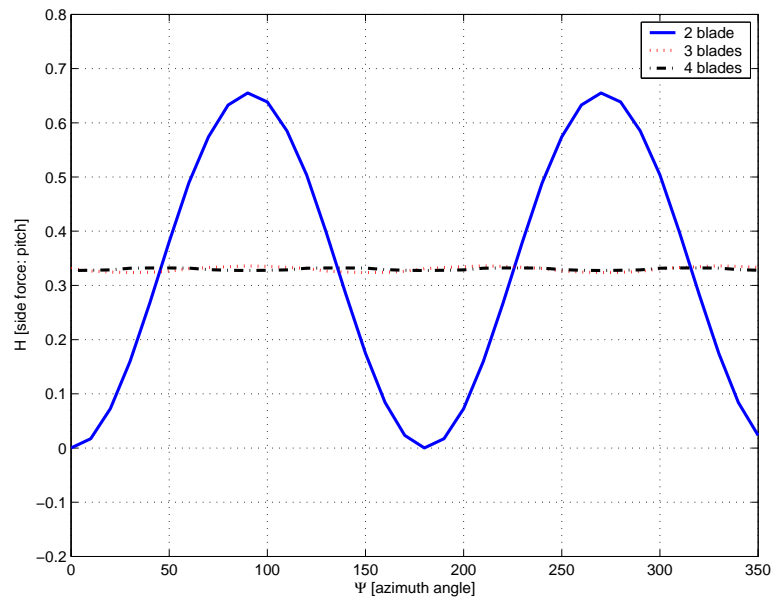
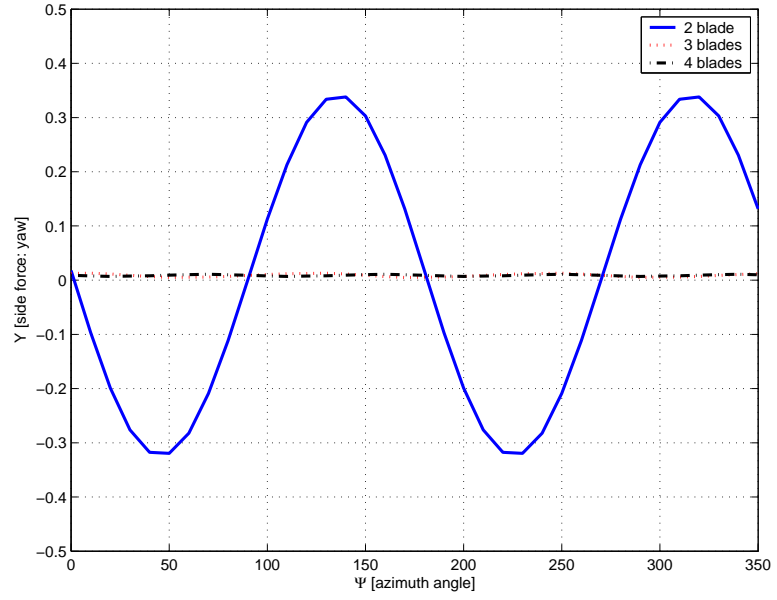


Figure 44: Propeller side forces (Y, H) per number of blades

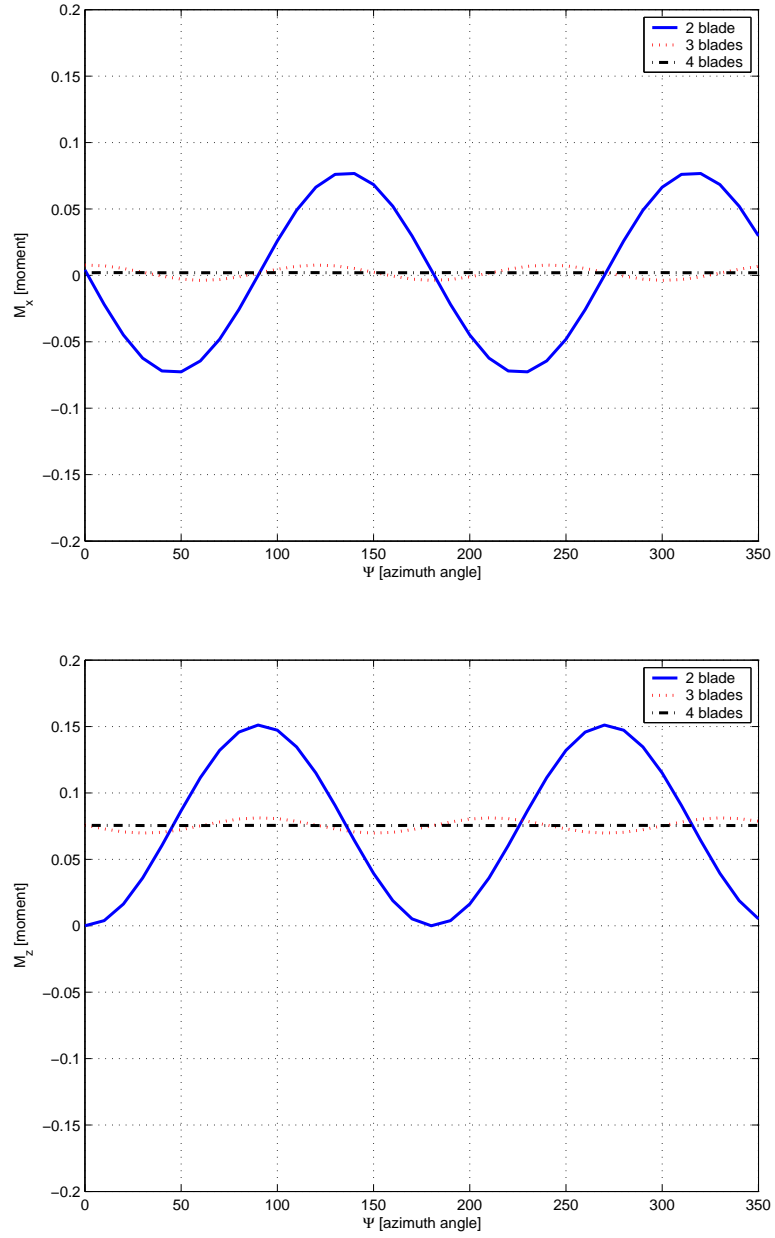


Figure 45: Propeller hub moments (M_x, M_z) per number of blades

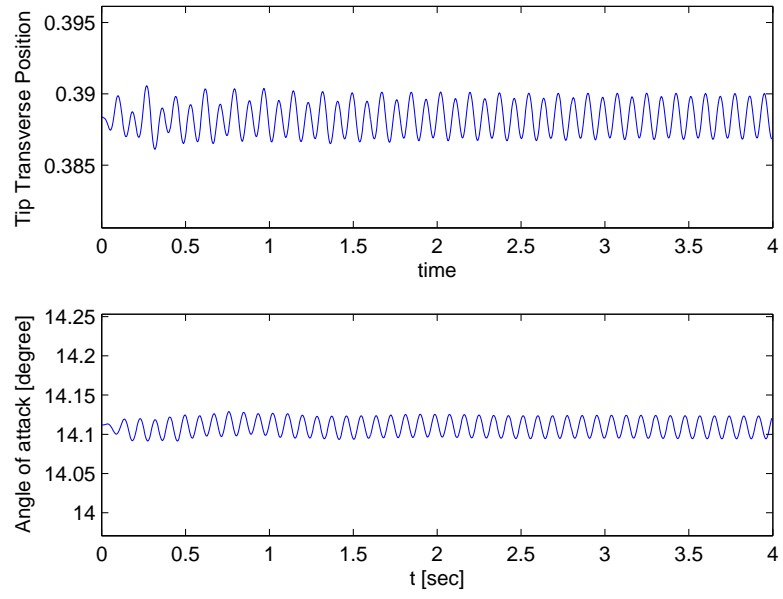


Figure 46: Time history of tip transverse position and angle of attack

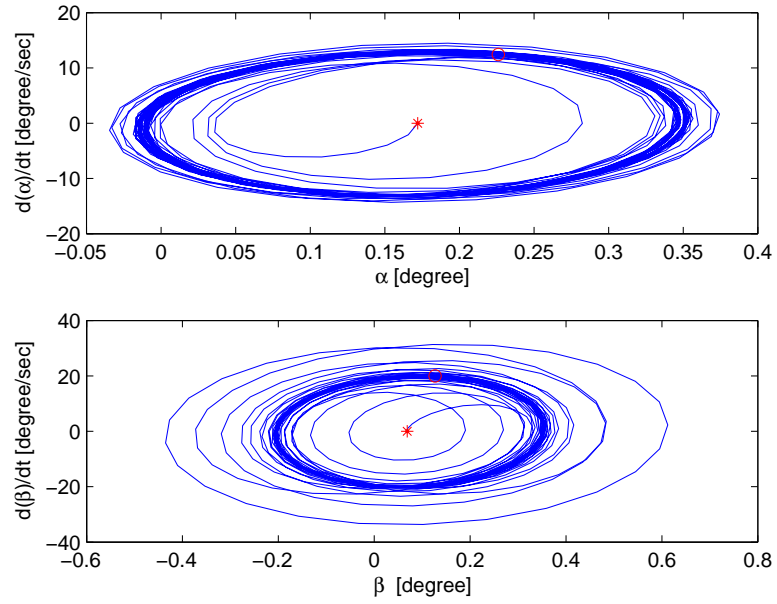


Figure 47: α vs $\dot{\alpha}$ and β vs $\dot{\beta}$ in phase plane

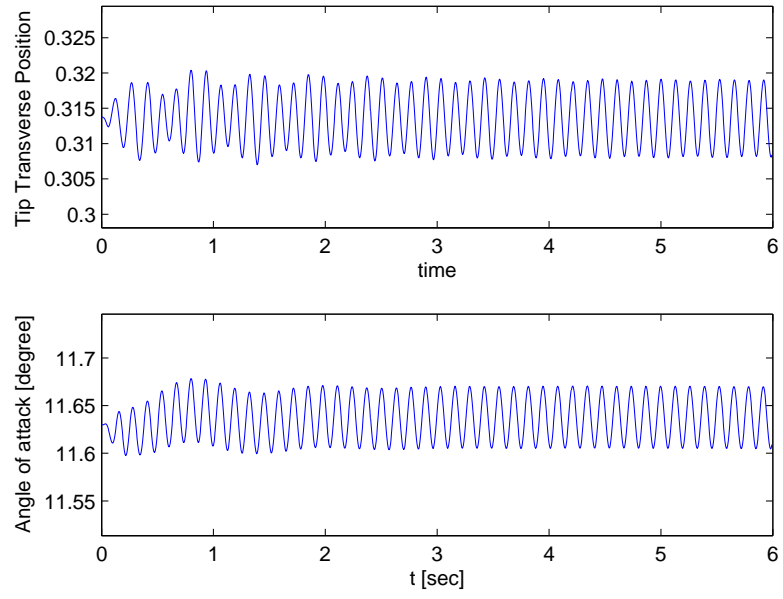


Figure 48: Time history of tip transverse position and angle of attack with less payload at mid-span

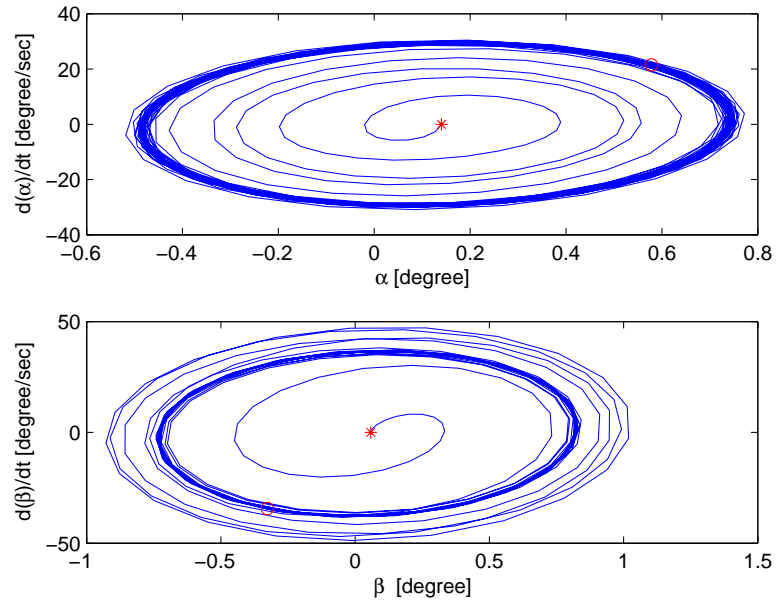


Figure 49: α vs $\dot{\alpha}$ and β vs $\dot{\beta}$ in phase plane with less payload at mid-span

4.9 Validations

4.9.1 Validations 1: Euler-Bernoulli Beam Theory

The analytic solution of beam attached to elastic spring at each end can be derived by the Euler-Bernoulli beam theory as

$$U_2 = \frac{m_1 g \ell_1^4}{24 I_{33}^c} \left(\eta^4 - 2\eta^3 + \eta + \frac{12 I_{33}^c}{k \ell^3} \right) \quad (116)$$

where m_1 is the mass per unit length of the beam, $I_{33}^c = \int_{\Omega} E_2 (x_2 - x_{2c})^2 d\Omega$, E_2 is the Young's modulus, x_c is the centroid of the beam cross-section and $0 \leq \eta \leq 1$ ($\eta = x_1/\ell_1$), and ℓ_1 is the total length of the beam.

Figure 50 shows the bending moment distribution along the span. The solution of NATASHA_{GVT} is quite close to the analytic solution of Euler Bernoulli beam theory. The norm of overall error in bending moment distribution ($\|\mathbf{r}\|_2 = M_{GVT}(x_s) - M_{EB}(x_s)$) is calculated and shown in Figure 51 with respect to the number of elements on a log scale. (M_{GVT} and M_{EB} are moment distribution of NATASHA_{GVT} and Euler-Bernoulli Beam theory. And 100 mid-points (x_s) of two solutions are chosen by linear interpolation at reference points.) The norm of overall error decreases monotonically as the number of elements increases.

4.9.2 Validations 2: RCAS

The trim conditions of NATASHA and RCAS (Rotorcraft Comprehensive Analysis System) [7] are compared to each other. Figure 52 shows the angle of attack in trim condition of NATASHA and RCAS with respect to various payloads at mid-span. Two results agree fairly well with each other. Note that modeling differences are inevitable due to the limitation on incorporating the control system. For NATASHA, the flap deflection and propeller angular speed are free variables to determine trim condition with given parameters. However, for RCAS, (which was developed for rotorcraft analysis), the angular speed is not available as free variable to determine trim condition. So the trim condition by RCAS is computed with fixed angular speed of NATASHA and the flap control is divided into interior and exterior one. Aerodynamic differences also exist. With respect to the flap deflection, NATASHA

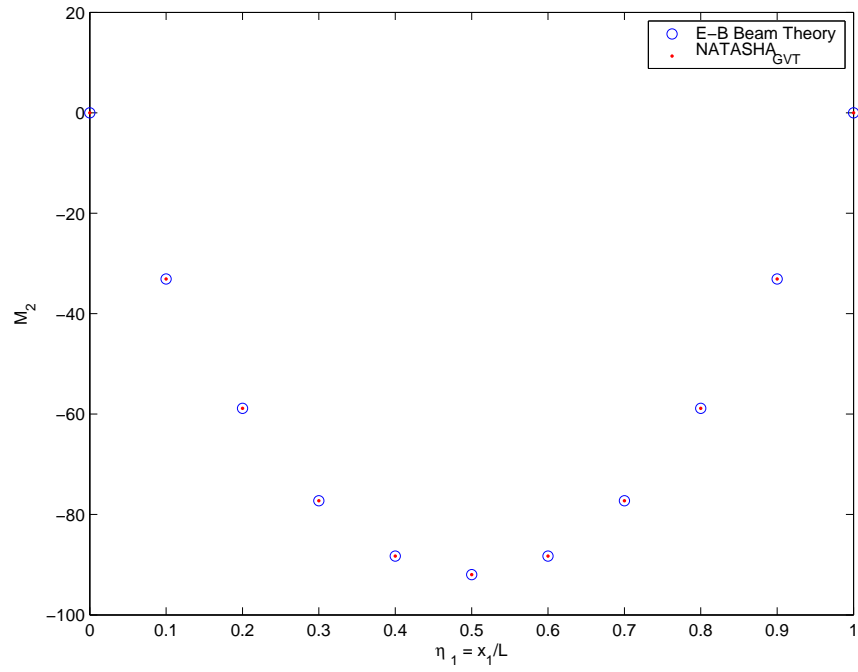


Figure 50: Bending moment distribution along the span from NATASHA_{GVT} and Euler-Bernoulli Beam Theory

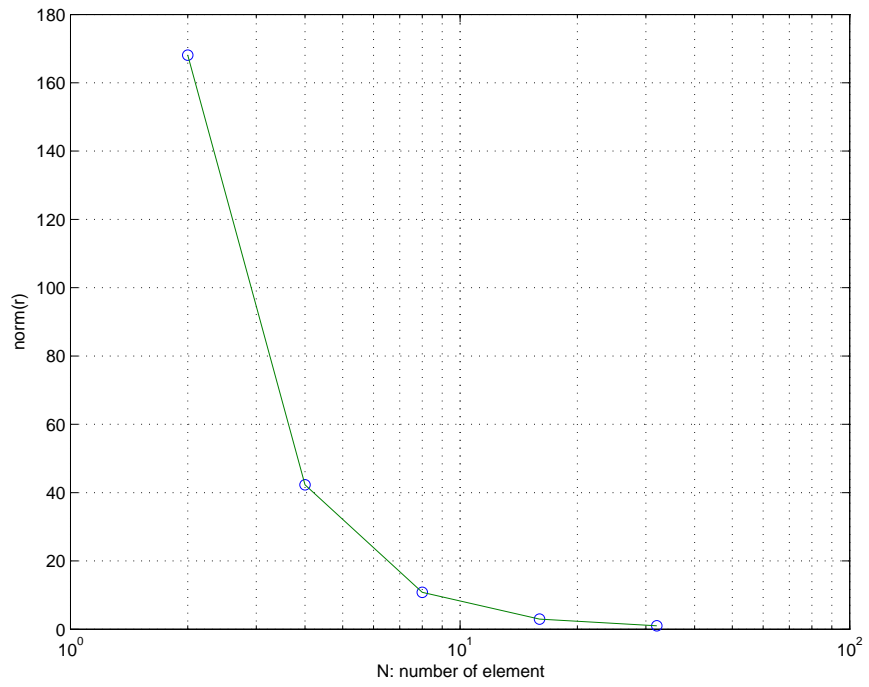


Figure 51: $\|\mathbf{r}\|_2$ with respect to the number of element on a log scale

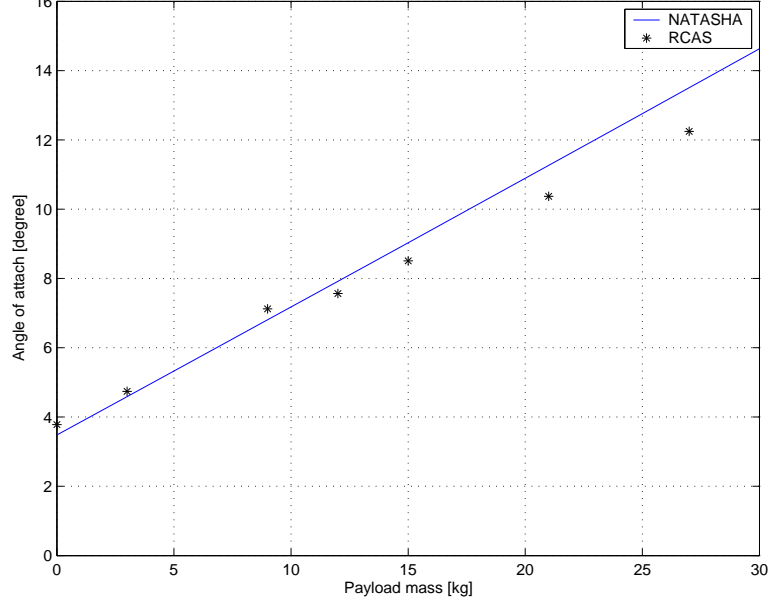


Figure 52: Angle of attack in trim condition by NATASHA and RCAS

uses the linear relation between the aerodynamic loads and flap deflection in terms of C_{ℓ_β} and C_{m_β} . On the other hand, RCAS uses the Theodorsen airfoil/elevon theory which evaluates the deficiency of lift and moment by elevon deflection. First, the deficiency coefficients in RCAS is chosen arbitrary so that the angle of attack without payload case matches closely to the result of NATASHA. Then, it is fixed for other payload cases to see if at least the results are consistent through the whole simulation. One of the simulation with payload (9 kg) is taken to compare the nodal force and moment resultants along the span shown in Figure 53.

Figure 54 shows propeller airloads from NATASHA and RCAS with respect to different tilting angles. A simple model is taken to evaluate this comparison. For NATASHA, a hub center of propeller is directly attached to inertial frame. For RCAS, a root of rigid bar is attached to a hinge in inertia frame with high value of rotational spring and the tip of the bar is attached to the hub center of propeller. Tip loss and inflow are included in the simple RCAS model. The tilting angle of propeller is defined by the angle between the freestream and the propeller disk. (0° tilting angle indicates that the propeller disk is perpendicular to the freestream.) The two approaches agree well with each other in Figure 54.

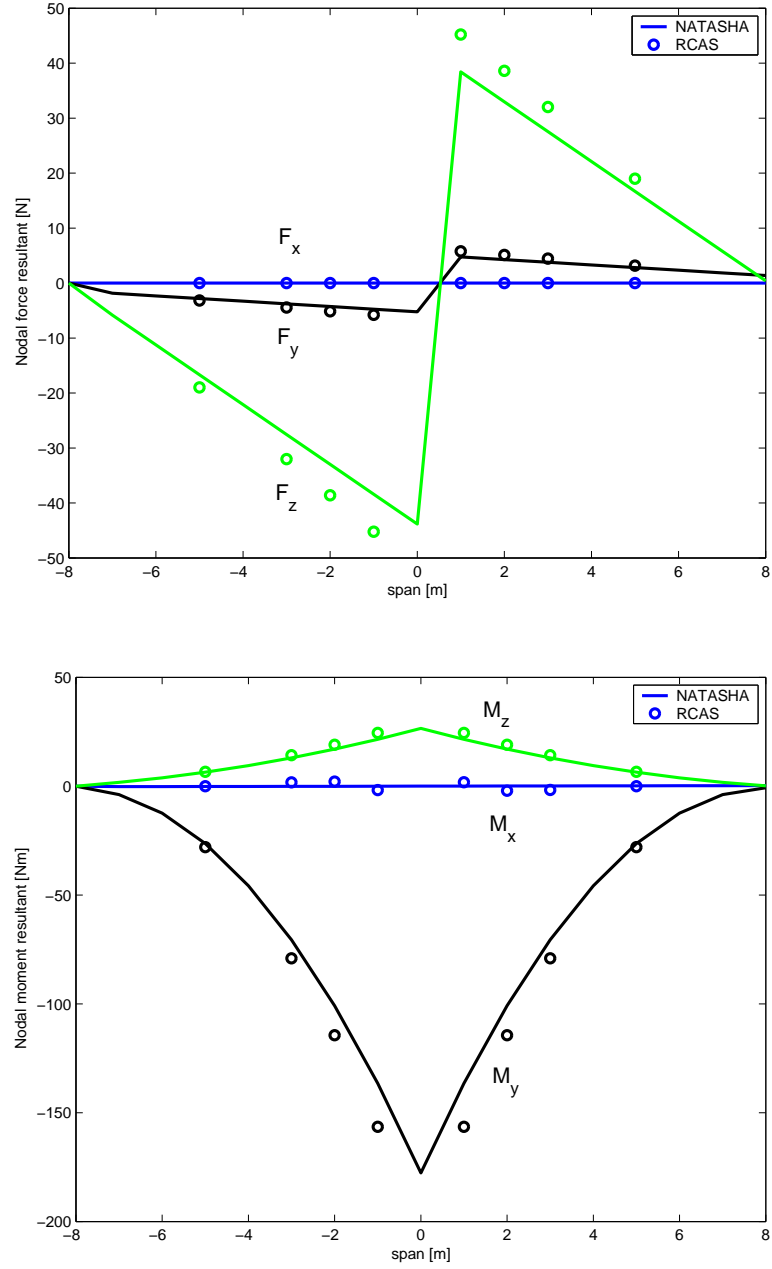


Figure 53: Nodal force and moment resultants from NATASHA and RCAS

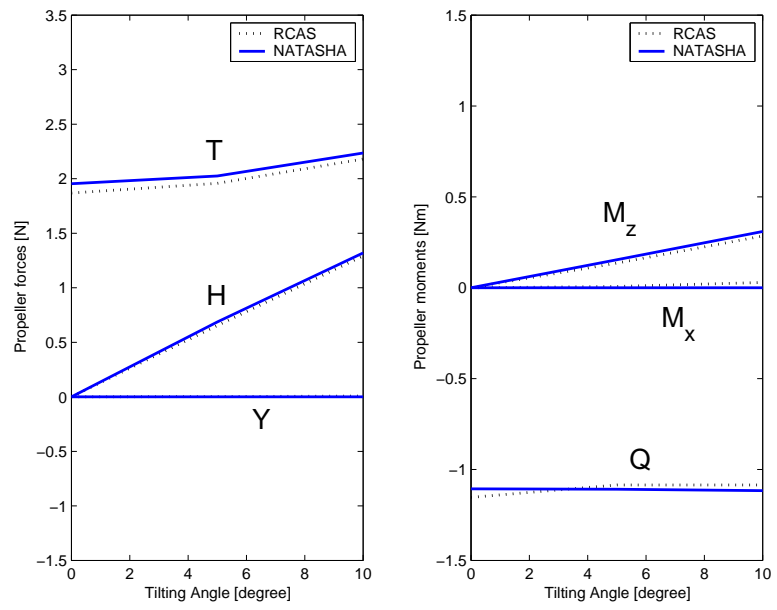


Figure 54: Comparison of the propeller airload evaluation between NATASHA and RCAS

CHAPTER V

CONCLUSION

The previously developed computer code (NATASHA) was limited in its application to the flight dynamics and aeroelastic analysis of HALE aircraft having a flying wing configuration. By completing the proposed three analysis upgrades, the current development has extended the HALE aircraft analysis methodology to treat other aircraft configurations and simulate the GVT environment by virtue of the multiple beam formulation, the bungee formulation, and Engine/Propeller modeling. The analysis methodology was coded to be applicable to different configurations as representative applications so that

- It includes the flight dynamics and aeroelastic analysis of HALE aircraft for either a flying wing or a conventional configuration. This was achieved by the multiple beam formulation which was reformulated from the original intrinsic beam formulation. This code is called NATASHA_{MB}.
- It now provides preliminary information about the modal characteristics of HALE aircraft from the GVT analysis. This was achieved by the multiple beam formulation and GVT formulation. First, it indicates possible coupling of GVT rigid-body modes with the lowest structural modes. This enables the GVT to be tailored so that structural modes are as close as possible to the free-free flight condition. When a modal description of the structural model is needed, it can assist user to choose target modes depending on its purpose. This code is called NATASHA_{GVT}.
- It now includes an Engine/Propeller model for propeller-driven HALE aircraft. This was achieved by the Engine/Propeller modeling. The whirling motion of Engine/Propeller model can now be coupled to the wing motion in the analysis. This code is called NATASHA_{WF}.

The parametric study shows how NATASHA can be utilized for the vibration and aeroelastic analysis of highly flexible HALE aircraft. The shape of the highly flexible wing affects the flight dynamic characteristic, showing that the U shape provides stable flight dynamics modes but it makes the system more prone to wing flutter as the wing becomes more flexible. Possible design improvements, such as by incorporating a horizontal tail like conventional configuration, can now be examined. Configurations with a horizontal tail can provide more stable flight dynamics characteristics.

The GVT parametric study provides an information about the modal characteristics of certain configurations. It also indicates that the GVT rigid-body modes of a highly flexible wing can be coupled to the structural modes as the flexibility increases, and the deformed shape of the wing may strongly affect modal characteristics. One specific modal description might not be applicable if the deformed configuration of a highly flexible wing is different from one flight condition to another. The changes in the modal characteristics need to be included to understand the dynamic behavior correctly.

The parametric study with Engine/Propeller model provides the boundary of certain HALE aircraft about when the periodic inertia effect of two blade Engine/Propeller model can be ignored and when it cannot. The equivalent three-bladed Engine/Propeller model can be used to obviate the need for Floquet theory, which is required for the stability analysis of periodic coefficient systems. Moreover, the validity of the constant approximation on the propeller aerodynamic loads is investigated. The trim condition determined by the constant approximation is checked to see whether the periodic propeller airload makes the states deviate from, or oscillate periodically around the original trim states.

Future Work

Even though it addresses new HALE aircraft methodologies, the current methodology needs further improvements in the following several aspects: other aircraft configurations, aerodynamics improvements, possible other experimental modeling of GVT analysis, GVT analytic model update, Floquet theory for two-bladed Engine/Propeller system and stability analysis, and control system design.

- *Other aircraft configurations:* The developed methodology has been applied to the flying wing and conventional configuration. The structural modeling is also capable of handling other aircraft configurations, such as joined-wing and flapping wing.
- *Aerodynamic Improvements:* Interference between propeller, wing, and fuselage has not yet been considered. Propeller aerodynamics is presently evaluated by a rather simple blade element theory using 2-D aerodynamics. More accurate aerodynamic modeling should be developed and integrated into current methodology.
- *Additional GVT modeling:* The bungee system, one of the possible types of GVT environment, is considered here. The zero-spring-suspension system is often used for an experimental GVT of large structures. A current multiple beam and bungee formulation can be extended to incorporate the zero-spring-suspension system into the analysis.
- *GVT analytic model update:* One of the possible improvements on GVT analysis is to compensate the analytic GVT analysis with the experimental counterpart. The analytical model will provide useful information for GVT experiments. And several methods using the experimental GVT data can be updated to the analytical model. (The literature survey in Chapter I covers the developed methods.) The result will be more credible information on the vibration characteristic of highly flexible HALE aircrafts .
- *Floquet Theory:* Floquet theory is needed when an equivalent three-bladed Engine/Propeller

system cannot approximate the two-bladed Engine/Propeller system of certain HALE aircraft. Moreover, the nonlinear dynamic simulation might makes the unstable mode appear to be stable one for finite time interval unless it simulates for a long period time when it determines the stability.

- *Control System Design:* More practical control systems such as linear state feedback, robust, and generalized predictive controls can be studied and designed to stabilize unusual flight dynamics modes, to suppress low frequency wing flutter and whirl flutter instability in a highly flexible HALE aircraft.

APPENDIX A

IDEAL MODELS

The natural frequencies of each mode for rigid body attached to bungee cords shown in Figure 55 can be calculated after it is simplified as an ideal model. For an ideal simple mass-spring system which is the 1st part of Figure 55, the plunging frequency is

$$\omega_p = \sqrt{\frac{k}{m}} \quad (117)$$

where k is a spring stiffness and m is the mass of rigid body.

For an ideal simple pendulum which is the 2nd part of Figure 55, the swing frequency is

$$\omega_s = \sqrt{\frac{g}{\ell_{\text{total}}}} = \sqrt{\frac{g}{\ell_{\text{natural}} + \delta + c/2}} \quad (118)$$

where δ is the spring deflection and c is the thickness of the rigid body.

For an ideal strut-supported wind tunnel model which is shown in the 3rd part of Figure 55, the self-oscillating frequency is

$$\omega_{so} = \sqrt{\frac{2k(a/2)^2}{\frac{m}{12}(a^2 + c^2)}} \quad (119)$$

For a slightly twisted trapeze which is the 4th part of Figure 55, the twisting frequency is

$$\omega_t = \sqrt{\frac{Wa^2}{4\ell_{\text{total}}I_{33}}} \quad (120)$$

where W is the total weight of rigid body and I_{33} is the moment of inertia with respect to the twisting axis.

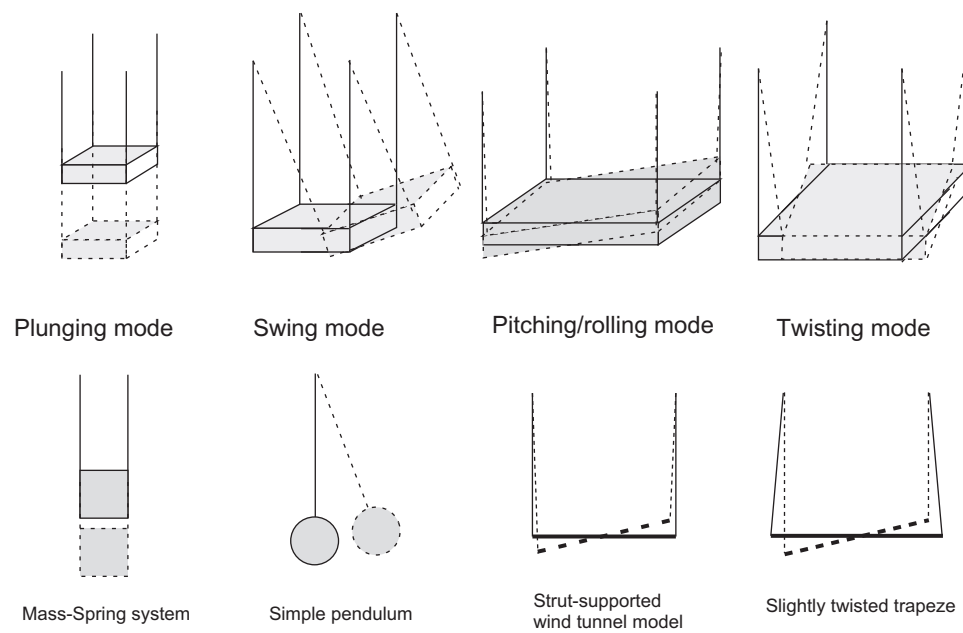


Figure 55: Schematic of GVT rigid-body modes and its ideal models

APPENDIX B

PRELIMINARY ENG/PROP MODELING

This preliminary analysis investigates two periodic effects which were already indicated by previous research [27, 54]. These are the periodic inertia effect of two-bladed propeller system and the periodic effect of side force and hub moment. The preliminary analysis is done before incorporating 2 dof flexible engine/store mount into NATASHA so that the analysis isolates dominant parameters in dynamic behavior by quantifying the periodic effects.

B.1 Dynamic Modeling

Figure 56 shows the idealized engine/propeller system for preliminary analysis. The point O is fixed in inertial frame. The point E is the center of mass of pylon, m_1 its mass, and h its length. The point P is the hub center of the propeller and the point B is an arbitrary point of a blade with distance r from the hub center P along the unit vector \mathbf{e}_3 .

B.1.1 Definition of Reference Frames

The unit vectors $\mathbf{i}_1, \mathbf{i}_2, \mathbf{i}_3$ are the base unit vectors of the inertial frame (\mathcal{F}_i). And the intermediate unit vectors $\mathbf{a}_1, \mathbf{a}_2, \mathbf{a}_3$ (\mathcal{F}_a), $\mathbf{b}_1, \mathbf{b}_2, \mathbf{b}_3$ (\mathcal{F}_b), and blade fixed reference frame unit vectors $\mathbf{e}_1, \mathbf{e}_2, \mathbf{e}_3$ (\mathcal{F}_e) are same in the ANALYSIS “3.3 Engine/Propeller Modeling”.

B.1.2 Evaluation of Potential and Kinetic Energies

The potential energy (P) of the system is

$$P = \frac{1}{2}k_\alpha\alpha^2 + \frac{1}{2}k_\beta\beta^2 + m_1g\frac{h}{2}\mathbf{i}_3 \cdot \mathbf{b}_2 + m_2gh\mathbf{i}_3 \cdot \mathbf{b}_2 \quad (121)$$

where k_α and k_β are the pitch and yaw stiffness, m_1 and m_2 are the mass of pylon and total blades, h and d are the length of pylon and diameter of blade, and g is the acceleration of gravity.

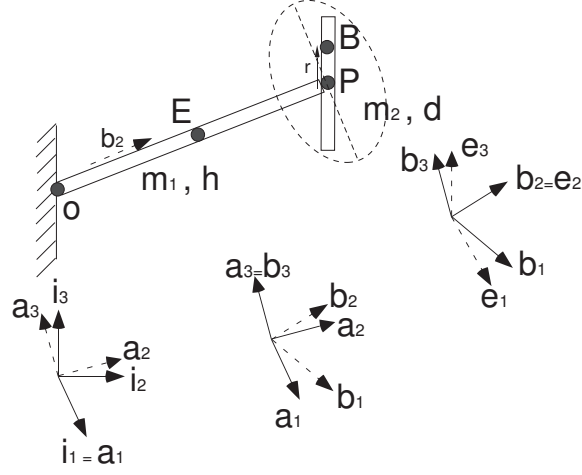


Figure 56: Schematic of simple engine/propeller system

The kinetic energy (K) of the system is

$$K = \frac{1}{2}m_1 \mathbf{V}_E \cdot \mathbf{V}_E + \frac{1}{2}\omega^{\mathbf{EI}} \cdot \mathbf{I}_E \cdot \omega^{\mathbf{EI}} + \frac{1}{2}m_2 \mathbf{V}_P \cdot \mathbf{V}_P + \frac{1}{2}\omega^{\mathbf{BI}} \cdot \mathbf{I}_P \cdot \omega^{\mathbf{BI}} \quad (122)$$

where \mathbf{V}_E and \mathbf{V}_P are the velocity vector of pylon center of mass and hub center of propeller, $\omega^{\mathbf{EI}}$ and $\omega^{\mathbf{BI}}$ are the angular velocity vector of pylon and propeller, and \mathbf{I}_E and \mathbf{I}_B are the inertia dyadic of pylon and total blades.

$$\mathbf{r}_E = \frac{h}{2} \mathbf{b}_2 = \frac{h}{2} (-s_\beta \mathbf{i}_1 + c_\alpha c_\beta \mathbf{i}_2 + s_\alpha c_\beta \mathbf{i}_3) \quad (123)$$

$$\mathbf{V}_E = \frac{h}{2} \left[-\dot{\beta} c_\beta \mathbf{i}_1 + (-\dot{\alpha} s_\alpha c_\beta - \dot{\beta} c_\alpha s_\beta) \mathbf{i}_2 + (\dot{\alpha} c_\alpha c_\beta - \dot{\beta} s_\alpha s_\beta) \mathbf{i}_3 \right]$$

$$\mathbf{V}_E \cdot \mathbf{V}_E = \left(\frac{h}{2} \right)^2 (\dot{\beta}^2 + \dot{\alpha}^2 c_\beta^2) \quad (124)$$

$$\mathbf{V}_P \cdot \mathbf{V}_P = h^2 (\dot{\beta}^2 + \dot{\alpha}^2 c_\beta^2) \quad (125)$$

The angular velocity vector of the pylon is

$$\omega^{\mathbf{EI}} = \dot{\alpha} \mathbf{a}_1 + \dot{\beta} \mathbf{b}_3 = \dot{\alpha} c_\beta \mathbf{b}_1 - \dot{\alpha} s_\beta \mathbf{b}_2 + \dot{\beta} \mathbf{b}_3 \quad (126)$$

The angular velocity vector of the blade is

$$\omega^{\mathbf{BI}} = \omega^{\mathbf{EI}} + \dot{\psi} \mathbf{b}_2 = \dot{\alpha} c_\beta \mathbf{b}_1 + (\dot{\psi} - \dot{\alpha} s_\beta) \mathbf{b}_2 + \dot{\beta} \mathbf{b}_3 \quad (127)$$

$$I_{[\mathcal{F}_e]} = \mathbf{e} \cdot \mathbf{I}_P \cdot \mathbf{e} = \begin{bmatrix} \frac{md^2}{12} & 0 & 0 \\ 0 & \frac{md^2}{12} & 0 \\ 0 & 0 & 0 \end{bmatrix}$$

$$I_{[\mathcal{F}_b]} = \mathbf{b} \cdot \mathbf{I}_P \cdot \mathbf{b} = R_2(\Psi) I_{[\mathcal{F}_e]} R_2(\Psi)^T \quad (128)$$

$$= \begin{bmatrix} c_\Psi & 0 & s_\Psi \\ 0 & 1 & 0 \\ -s_\Psi & 0 & c_\Psi \end{bmatrix} \begin{bmatrix} \frac{m_2 d^2}{12} & 0 & 0 \\ 0 & \frac{m_2 d^2}{12} & 0 \\ 0 & 0 & 0 \end{bmatrix} \begin{bmatrix} c_\Psi & 0 & s_\Psi \\ 0 & 1 & 0 \\ -s_\Psi & 0 & c_\Psi \end{bmatrix}^T$$

$$K = \left[\frac{1}{2} m_1 \left(\frac{h}{2} \right)^2 + \frac{1}{2} \frac{m_1 h^2}{12} + \frac{1}{2} m_2 h^2 \right] (\dot{\beta}^2 + \dot{\alpha}^2 c_\beta^2) \quad (129)$$

$$+ \frac{1}{2} \frac{m_2 d^2}{12} \left[\dot{\alpha}^2 c_\Psi^2 c_\beta^2 + (-\dot{\alpha} s_\beta + \dot{\Psi})^2 - 2\dot{\alpha} \dot{\beta} c_\Psi s_\Psi c_\beta + \dot{\beta}^2 s_\Psi^2 \right]$$

B.2 Aerodynamic Model

This aerodynamic model is the same as 3.3.2 Propeller Aerodynamics in III ANALYSIS.

B.3 Governing Equation

Hamilton's extended principle is

$$\int_{t_i}^{t_f} (\delta K - \delta P + \overline{\delta W}) dt = \overline{\delta A} \quad (130)$$

$$\delta P = k_\alpha \alpha \delta \alpha + k_\beta \beta \delta \beta + gh(c_\alpha c_\beta \delta \alpha - s_\alpha s_\beta \delta \beta) \left(\frac{m_1}{2} + m_2 \right)$$

$$\delta K = \left[\frac{m_1}{2} \left(\frac{h}{2} \right)^2 + \frac{1}{2} \frac{m_1 h^2}{12} + \frac{1}{2} m_2 h^2 \right] [2\dot{\beta} \delta \dot{\beta} + 2\dot{\alpha} c_\beta^2 \delta \dot{\alpha} - 2\dot{\alpha}^2 c_\beta s_\beta \delta \beta]$$

$$+ \frac{1}{2} \frac{m_2 d^2}{12} [2\dot{\alpha} c_\Psi^2 c_\beta^2 \delta \dot{\alpha} - 2\dot{\alpha}^2 c_\Psi s_\Psi c_\beta^2 \delta \Psi - 2\dot{\alpha}^2 c_\Psi^2 c_\beta s_\beta \delta \beta]$$

$$+ 2(-\dot{\alpha} s_\beta + \dot{\Psi})(-s_\beta \delta \dot{\alpha} - \dot{\alpha} c_\beta \delta \dot{\beta} + \delta \dot{\Psi}) \quad (131)$$

$$- 2\dot{\beta} c_\Psi s_\Psi c_\beta \delta \dot{\alpha} - 2\dot{\alpha} c_\Psi s_\Psi c_\beta \delta \dot{\beta} + 2\dot{\alpha} \dot{\beta} s_\Psi^2 c_\beta \delta \Psi - 2\dot{\alpha} \dot{\beta} c_\Psi^2 c_\beta \delta \Psi + 2\dot{\alpha} \dot{\beta} c_\Psi s_\Psi s_\beta \delta \beta$$

$$+ 2\dot{\beta} s_\Psi^2 \delta \dot{\beta} + 2\dot{\beta}^2 s_\Psi c_\Psi \delta \Psi]$$

$$\overline{\delta W} = -Y_o h c_\beta \delta \beta - T_o h (s_\alpha c_\beta \delta \alpha + c_\alpha s_\beta \delta \beta) + H_o h (c_\alpha c_\beta \delta \alpha - s_\alpha s_\beta \delta \beta)$$

$$+ M_x c_\beta \delta \alpha - Q s_\beta \delta \alpha + M_z \delta \beta$$

For $\delta\alpha$

$$\begin{aligned}
& \left[m_1 \left(\frac{h}{2} \right)^2 + m_2 h^2 + \frac{m_1 h^2}{12} \right] (\ddot{\alpha} c_\beta - 2\dot{\alpha} \dot{\beta} c_\beta s_\beta) \\
& + \frac{m_2 d^2}{12} [\ddot{\alpha} c_\Psi^2 c_\beta^2 - 2\dot{\alpha} \dot{\Psi} c_\Psi s_\Psi c_\beta^2 - 2\dot{\alpha} \dot{\beta} c_\Psi^2 c_\beta s_\beta - (-\ddot{\alpha} s_\beta - \dot{\alpha} \dot{\beta} c_\beta + \ddot{\Psi}) s_\beta - (-\dot{\alpha} s_\beta + \dot{\Psi}) \dot{\beta} c_\beta \\
& \quad - \ddot{\beta} c_\Psi s_\Psi c_\beta + \dot{\beta} \dot{\Psi} s_\Psi^2 c_\beta - \dot{\beta} \dot{\Psi} c_\Psi^2 c_\beta + \dot{\beta}^2 c_\Psi s_\Psi s_\beta] \\
& + k_\alpha \alpha + g h c_\alpha c_\beta \left(\frac{m_1}{2} + m_2 \right) \\
& = -T_o h s_\alpha c_\beta + H_o h c_\alpha c_\beta + M_x c_\beta
\end{aligned} \tag{132}$$

For $\delta\beta$

$$\begin{aligned}
& \left[m_1 \left(\frac{h}{2} \right)^2 + m_2 h^2 + \frac{m_1 h^2}{12} \right] (\ddot{\beta} + \dot{\alpha}^2 c_\beta s_\beta) \\
& + \frac{m_2 d^2}{12} \left[-\ddot{\alpha} c_\Psi s_\Psi c_\beta + \dot{\alpha} \dot{\Psi} s_\Psi^2 c_\beta - \dot{\alpha} \dot{\Psi} c_\Psi^2 c_\beta + \dot{\alpha} \dot{\beta} c_\Psi s_\Psi s_\beta + \ddot{\beta} s_\Psi^2 + 2\dot{\beta} \dot{\Psi} s_\Psi c_\Psi \right] \\
& - \frac{m_2 d^2}{12} \left[-\dot{\alpha}^2 c_\Psi^2 c_\beta s_\beta - (-\dot{\alpha} s_\beta + \dot{\Psi}) \dot{\alpha} c_\beta + \dot{\alpha} \dot{\beta} c_\Psi s_\Psi s_\beta \right] \\
& + k_\beta \beta - g h s_\alpha s_\beta \left(\frac{m_1}{2} + m_2 \right) \\
& = -Y_o h c_\beta - T_o h c_\beta s_\beta - H_o h s_\alpha s_\beta + M_z
\end{aligned} \tag{133}$$

For $\delta\Psi$

$$\ddot{\alpha} s_\beta + \dot{\alpha} \dot{\beta} c_\beta - \ddot{\Psi} - \dot{\alpha}^2 c_\Psi s_\Psi c_\beta^2 + \dot{\alpha} \dot{\beta} s_\Psi^2 c_\beta - \dot{\alpha} \dot{\beta} c_\Psi^2 c_\beta + \dot{\beta}^2 s_\Psi c_\Psi = Q + Q_o \tag{134}$$

where Q is the applied torque.

B.4 Nondimensionalization

Nondimensional quantities ($R_m = \frac{m_2}{m_1}$, $R_\ell = \frac{d}{h}$, $k_\alpha^* = \frac{k_\alpha}{m_1 h^2 \Omega_o^2}$, $g^* = \frac{g}{h \Omega_o^2}$, and $\tau = \Omega_o t$) are introduced. For $\delta\alpha$

$$\begin{aligned}
& \left(R_m + \frac{1}{3} \right) (\alpha'' c_\beta - 2\alpha' \beta' c_\beta s_\beta) + \frac{R_m R_\ell^2}{12} [\alpha'' c_\Psi^2 c_\beta^2 \\
& - 2\alpha' \Psi' c_\Psi s_\Psi c_\beta^2 - 2\alpha' \beta' c_\Psi^2 c_\beta s_\beta - (-\alpha'' s_\beta - \alpha' \beta' c_\beta + \Psi'') s_\beta - (-\alpha' s_\beta + \Psi') \beta' c_\beta \\
& - \beta'' c_\Psi s_\Psi c_\beta + \beta' \Psi' s_\Psi^2 c_\beta - \beta' \Psi' c_\Psi^2 c_\beta + \beta'^2 c_\Psi s_\Psi s_\beta] + k_\alpha^* \alpha + g^* c_\alpha c_\beta \left(\frac{1}{2} + R_m \right) \\
& = -H_o^* s_\alpha c_\beta + Y_o^* c_\alpha c_\beta + M_x^* c_\beta
\end{aligned} \tag{135}$$

For $\delta\beta$

$$\begin{aligned}
& \left(R_m R_\ell^2 + \frac{1}{3} \right) (\beta'' + \alpha'^2 c_\beta s_\beta) \\
& + \frac{R_m R_\ell^2}{12} (-\alpha'' c_\Psi s_\Psi c_\beta + \alpha' \Psi' s_\Psi^2 c_\beta - \alpha' \Psi' c_\Psi^2 c_\beta + \alpha' \beta' c_\Psi s_\Psi s_\beta + \beta'' s_\Psi^2 + 2\beta' \Psi' s_\Psi c_\Psi) \\
& - \frac{m_2 d^2}{12} [-\alpha'^2 c_\Psi^2 c_\beta s_\beta - (-\alpha' s_\beta + \Psi') \alpha' c_\beta + \alpha' \beta' c_\Psi s_\Psi s_\beta] + k_\beta^* \beta - g^* s_\alpha s_\beta \left(\frac{1}{2} + R_m \right) \\
& = -T_o^* c_\beta - H_o^* c_\beta s_\beta - Y_o^* s_\alpha s_\beta + M_z^*
\end{aligned} \tag{136}$$

For $\delta\Psi$

$$\alpha'' s_\beta + \alpha' \beta' c_\beta - \Psi'' - \alpha'^2 c_\Psi s_\Psi c_\beta^2 + \alpha' \beta' s_\Psi^2 c_\beta - \alpha' \beta' c_\Psi^2 c_\beta + \beta'^2 s_\Psi c_\Psi = Q^* + Q_o^* \tag{137}$$

REFERENCES

- [1] ALBUS, J., BOSTELMAN, R., and DAGALAKIS, N., “The nist spider, a robot crane,” *Journal of Research of the NIST*, vol. 97, pp. 373–385, 1992.
- [2] ALP, A. B. and AGRAWAL, S. K., “Cable suspended robots: Design, planning and control,” in *proceedings of the 2002 IEEE Int. Conf. on Robotics and Automation*, pp. 4275–4280, 2002.
- [3] ANAND, L., “On H. Hencky’s approximate strain-energy function for moderate deformations,” *Journal of Applied Mechanics*, vol. 46, pp. 78–82, March 1979.
- [4] ARRUDA, E. M. and C., B. M., “A three-dimensional constitutive model for the large stretch behavior of rubber elastic materials,” *Journal of the Mechanics and Physics of Solids*, vol. 41, pp. 389–412, Feb 1993.
- [5] BENNETT, R. M. and BLAND, S. R., “Experimental and analytical investigation of propeller whirl flutter of a power plant on a flexible wing,” Technical note TN D-2399, NASA, August 1964.
- [6] BEZVERKHII, A. I., KORNIENKO, V. F., and SHUL’GA, N. A., “Forced spatial vibrations of anchor cable systems,” *International Applied Mechanics*, vol. 37, pp. 1222–1228, Sep. 2001.
- [7] BIR, G. S., “Structural dynamics verification of rotorcraft comprehensive analysis system (rcas),” technical report, National Renewable Energy Laboratory (NREL), Feb. 2005.
- [8] BLAKELY, K., “Cross-orthogonality calculations for pre-test planning and model verification,” in *MSC World Users’ Conference*, 1993.
- [9] BLAKELY, K., “Matching frequency response test data with msc/nastran,” in *MSC World Users’ Conference*, 1994.
- [10] DEGENER, M., HODGES, D. H., and PETERSEN, D., “Analytical and experimental study of beam torsional stiffness with large axial elongation,” *Journal of Applied Mechanics*, vol. 110, pp. 171–178, 1988.
- [11] DENG, H., JIANG, Q. F., and KWAN, A., “Shape finding of incomplete cable-strut assemblies containing slack and prestressed elements,” *Computers and Structures*, vol. 83, no. 21-22, pp. 1767–1779, 2005.
- [12] DIAFERIO, M. and SEPE, V., “Smoothed slack cable models for large amplitude oscillations of suspension bridges,” *Mechanics Based Design of Structures and Machines*, vol. 32, no. 3, pp. 363–400, 2004.
- [13] DRELA, M., “Integrated simulation model for preliminary aerodynamic, structural, and control-law design of aircraft,” in *Proceedings of the 40th Structures, Structural*

- Dynamics and Materials Conference, Saint Louis, Missouri*, pp. 1644 – 1656, April 12 – 15, 1999.
- [14] DRISCOLL, R. and NAHON, M., “Modeling and simulation of a moored buoy system,” in *Proceedings of OCEANS '96 MTS/IEEE*, (New York), pp. 517–523, 1996.
 - [15] EDENBOROUGH, H. K., “Investigation of tilt-rotor vtol aircraft rotorpylon stability,” *Journal of Aircraft*, vol. 5, no. 2, pp. 97–105, 1968.
 - [16] GARCIA, J. A., “Numerical investigation of nonlinear aeroelastic effects on flexible high-aspect-ratio wings,” *Journal of Aircraft*, vol. 42, no. 4, pp. 1025–1036, 2005.
 - [17] GATTULLI, V., MARTINELLI, L., PEROTTI, F., and VESTRONI, F., “Nonlinear oscillations of cables under harmonic loading using analytical and finite element models,” *Computer Methods in Applied Mechanics and Engineering*, vol. 193, no. 2, pp. 69–85, 2004.
 - [18] GOELLER, J. E. and LAURA, P. A., “Analytical and experimental study of the dynamic response of segmented cable systems,” *Journal of Sound and Vibration*, vol. 18, no. 3, pp. 311–324, 1971.
 - [19] GOGÉ, D., “Automatic updating of large aircraft models using experimental data from ground vibration testing,” *Aerospace Science and Technology*, vol. 7, pp. 33–45, January 2003.
 - [20] GOGÉ, D., “Fast identification and characterisation of non-linearities in experimental modal analysis of large aircraft,” in *International Aviation and Space Salon MAKS*, (Moscow, Russia), August 16-21 2005.
 - [21] GOGÉ, D., FULLEKRUG, U., SINAPIUS, M., LINK, M., and GAUL, L., “Advanced test strategy for identification and characterization of nonlinearities of aerospace structures,” *AIAA Journal*, vol. 43, no. 5, pp. 974–986, 2005.
 - [22] HODGES, D. H., “A mixed variational formulation based on exact intrinsic equations for dynamics of moving beams,” *International Journal of Solids and Structures*, vol. 26, no. 11, pp. 1253 – 1273, 1990.
 - [23] HODGES, D. H., “Geometrically-exact, intrinsic theory for dynamics of curved and twisted anisotropic beams,” *AIAA Journal*, vol. 41, pp. 1131–1137, June 2003.
 - [24] HOUBOLT, J. C. and REED, W. H., I., “Propeller-nacelle whirl flutter,” *Journal of the Aerospace Sciences*, vol. 29, no. 3, pp. 333–346, 1962.
 - [25] JAMES, A. G., GREEN, A., and SIMPSON, G. M., “Strain energy functions of rubber. I. characterization of gum vulcanizates,” *Journal of Applied Polymer Science*, vol. 19, no. 7, pp. 2033 – 2058, 1975.
 - [26] JOHNSON, W., “Dynamics of tilting proprotor aircraft in cruise flight,” Tech. Rep. TN D-7677, NASA, May 1974.
 - [27] JOHNSON, W., “Analytical modeling requirements for tilting proprotor aircraft dynamics,” Technical Note TN D-8013, NASA, July 1975.

- [28] KAMMAN, J. W. and HUSTON, R. L., “Multibody dynamics modeling of variable length cable systems,” *Multibody System Dynamics*, vol. 5, pp. 211–221, 2001.
- [29] KERSCHEN, G., LENAERTS, V., and GOLINVAL, J. C., “VTT benchmark: application of the restoring force surface method,” *Mechanical Systems and Signal Processing*, vol. 17, pp. 189–193, January 2003.
- [30] KIENHOLZ, D. A., CRAWLEY, E. F., and HARVEY, T. J., “Very low frequency suspension systems for dynamic testing,” in *Proceedings of the 30th Structures, Structural Dynamics and Materials Conference*, (Mobile, AL), pp. 327–336, AIAA, April 3-5 1989.
- [31] KOVACS, I. and VOROS, G., “On the mathematical description of the tensile stress-strain curves of polycrystalline face centered cubic metals,” *International Journal of Plasticity*, vol. 12, no. 1, pp. 35–43, 1996.
- [32] KUNZ, D. L., “Analysis of proprotor whirl flutter: Review and update,” *Journal of Aircraft*, vol. 42, pp. 172–178, Feb. 2005.
- [33] KVATERNIK, R. G., JUANG, J.-N., and BENNETT, R. L., “Exploratory studies in generalized predictive control for active aeroelastic control of tiltrotor aircraft,” TM 2000-210552, NASA Langley Research Center, 2000.
- [34] LUBRINA, P. and DEGENER, M., “Modal identification of large aircraft,” in *First ONERA-DLR Aerospace Symposium*, (Paris), 21-24 June 1999.
- [35] MAYS, T. W., PLAUT, R. H., and LIAPIS, S. I., “Three-dimensional analysis of submerged, moored, horizontal, rigid cylinders used as breakwaters,” *Ocean Engineering*, vol. 26, pp. 1311–1333, 1999.
- [36] MEIROVITCH, L., “Hybrid state equations of motion for flexible bodies in terms of quasi-coordinates,” *Journal of Guidance, Control, and Dynamics*, vol. 14, no. 5, pp. 1008–1013, 1991.
- [37] MEIROVITCH, L. and TUZCU, I., “Time simulations of the response of maneuvering flexible aircraft,” *Journal of Guidance, Control, and Dynamics*, vol. 27, no. 5, pp. 814–828, 2004.
- [38] MEIROVITCH, L. and TUZCU, I., “Unified theory for the dynamics and control of maneuvering flexible aircraft,” *AIAA Journal*, vol. 42, no. 4, pp. 714–727, 2004.
- [39] OGDEN, R. W., “Large deformation isotropic elasticity – on the correlation of theory and experiment for incompressible rubberlike solids,” in *Proceedings of the Royal Society of London. Series A, Mathematical and Physical Sciences*, pp. 565–584, Feb 1972.
- [40] PARK, J., CHUNG, W.-K., and MOON, W., “Wire-suspended dynamical system: stability analysis by tension-closure,” *IEEE Transactions on Robotics*, vol. 21, no. 3, pp. 298–308, 2005.
- [41] PATIL, M. J. and HODGES, D. H., “Static output feedback control of nonlinear aeroelastic response of a slender wing,” *Journal of Guidance, Control and Dynamics*, vol. 25, pp. 302 – 308, Mar.-Apr. 2002.

- [42] PATIL, M. J., HODGES, D. H., and CESNIK, C. E. S., “Nonlinear aeroelasticity and flight dynamics of high-altitude long-endurance aircraft,” in *Proceedings of the 40th Structures, Structural Dynamics and Materials Conference, Saint Louis, Missouri*, pp. 2224 – 2232, April 12 – 15, 1999. AIAA Paper 99-1470.
- [43] PATIL, M. J., HODGES, D. H., and CESNIK, C. E. S., “Nonlinear aeroelastic analysis of complete aircraft in subsonic flow,” *Journal of Aircraft*, vol. 37, pp. 753 – 760, Sept.-Oct. 2000.
- [44] PATIL, M. J. and HODGES, D. H., “Flight dynamics of highly flexible flying wings,” in *CEAS/AIAA/DGLR International Forum on Aeroelasticity and Structural Dynamics, Munich, Germany*, June 28 – July 1, 2005. (to appear, *Journal of Aircraft*, 2007).
- [45] PETERS, D. A., KARUNAMOORTHY, S., and CAO, W.-M., “Finite state induced flow models; part I: two-dimensional thin airfoil,” *Journal of Aircraft*, vol. 32, pp. 313 – 322, Mar.-Apr. 1995.
- [46] RAND, O. and PEYRAN, R. J., “Experimental demonstration of the influence of wing couplings on whirlflutter instability,” *Journal of Aircraft*, vol. 37, no. 5, pp. 859–864, 2000.
- [47] REED, W. H., I. and BLAND, S. R., “An analytical treatment of aircraft propeller precession instability,” Technical note TN D-659, NASA, January 1961.
- [48] ROBERTS, R. G., GRAHAM, T., and LIPPITT, T., “On the inverse kinematics, statics, and fault tolerance of cable-suspended robots,” *Journal of Robotic Systems*, vol. 15, no. 10, pp. 581–597, 1998.
- [49] SCANLAN, R. H. and TRUMAN, J. C., “The gyroscopic effect of a rigid rotating propeller on engine and wing vibration modes,” *Journal of the Aeronautical Sciences*, vol. 17, no. 10, pp. 653–659, 666, 1950.
- [50] SCHMIDT, D. K. and RANEY, D. L., “Modeling and simulation of flexible flight vehicles,” *Journal of Guidance, Control, and Dynamics*, vol. 24, no. 3, pp. 539–546, 2001.
- [51] SHIANG, W.-J., CANNON, D., and GORMAN, J., “Dynamic analysis of the cable array robotic crane,” in *Proceedings of the 1999 IEEE Int. Conf. on Robotics and Automation*, pp. 2495–2500, 1999.
- [52] SHIANG, W.-J., CANNON, D., and GORMAN, J., “Optimal force distribution applied to a robotic crane with flexible cables,” in *Proceedings of the 2000 IEEE Int. Conf. on Robotics and Automation*, pp. 1948–1954, 2000.
- [53] SIMON, M. and TOMLINSON, G. R., “Use of the Hilbert transform in modal analysis of linear and non-linear structures,” *Journal of Sound and Vibration*, vol. 96, pp. 421–436, October 22, 1984.
- [54] SINGH, B. and CHOPRA, I., “Whirl flutter stability of two-bladed prop rotor/pylon systems in high speed flight,” in *43rd AIAA/ASME/ASCE/AHS/ASC Structures, Structural Dynamics, and Materials*, (Denver, Colorado), AIAA, Apr. 22-25 2002.

- [55] SINGH, R., GANDHI, F., and HATHAWAY, E., “Active tiltrotor whirl-flutter stability augmentation using wing-flaperon and swashplate actuation,” in *46th AIAA/ASME/ASCE/AHS/ASC Structures, Structural Dynamics and Materials*, (Austin, Texas), AIAA, Apr. 18-21 2005.
- [56] SNYDER, R. D., HUR, J. Y., STRONG, D. D., and BERAN, P. S., “Aeroelastic analysis of a high-altitude long-endurance joined-wing aircraft,” in *CEAS/AIAA/DGLR International Forum on Aeroelasticity and Structural Dynamics*, (Munich, Germany), June 28 – July 1 2005.
- [57] SRINIVAS, V. and CHOPRA, I., “Formulation of a comprehensive aeroelastic analysis for tilt-rotor aircraft,” *Journal of Aircraft*, vol. 35, no. 2, pp. 280–287, 1998.
- [58] TAYLOR, E. S. and BROWNE, K. A., “Vibration isolation of aircraft power plants,” *Journal of the Aeronautical Sciences*, vol. 6, no. 2, pp. 43–49, 1938.
- [59] TETER, J. E., J., “A discussion of zero spring rate mechanisms used for the active isolation mount experiment,” TM 1999-209723, NASA Langley Research Center, 1999.
- [60] TSUKROV, I., EROSHKIN, O., PAUL, W., and CELIKKOL, B., “Numerical modeling of nonlinear elastic components of mooring systems,” *IEEE Journal of Oceanic Engineering*, vol. 30, pp. 37–46, Jan 2005.
- [61] VAN SCHOOR, M. C. and VON FLOTOW, A. H., “Aeroelastic characteristics of a highly flexible aircraft,” *Journal of Aircraft*, vol. 27, pp. 901 – 908, Oct. 1990.
- [62] VASSALOS, D. and HUANG, S., “Non-linear dynamics of small-sagged taut-slack marine cables,” *Computers and Structures*, vol. 58, no. 3, pp. 557–562, 1996.
- [63] WANG, P.-H., LIN, H.-T., and TANG, T.-Y., “Study on nonlinear analysis of a highly redundant cable-stayed bridge,” *Computers and Structures*, vol. 80, pp. 165–182, January 2001.
- [64] WASZAK, M. R. and SCHMIDT, D. K., “Flight dynamics of aeroelastic vehicles,” *Journal of Aircraft*, vol. 25, pp. 563 – 571, June 1988.
- [65] WOODARD, S. E. and HOUSNER, J. M., “Nonlinear behavior of a passive zero-spring-rate suspension system,” *Journal of Guidance, Control, and Dynamics*, vol. 14, no. 1, pp. 84–89, 1991.
- [66] YANG, M. and BROWN, D., “An improved procedure for handling damping during finite element model updating,” *14th International Modal Analysis Conference (IMAC)*, Dearborn, Michigan, pp. 576–584, Feb 12-15 1996.
- [67] YANG, M. and BROWN, D., “Model updating techniques using perturbed boundary condition (pbc) testing data,” *14th International Modal Analysis Conference (IMAC)*, Dearborn, Michigan, pp. 776–782, Feb 12-15 1996.
- [68] ZERWECKH, S. H., VON FLOTOW, A. H., and MURRAY, J. E., “Flight testing a highly flexible aircraft – case study on the mit light eagle,” *Journal of Aircraft*, vol. 27, no. 4, pp. 342–349, 1990.

VITA

Chong-Seok Chang was born in Daegu, South Korea, in March 1976. He received his Bachelor's degree in aerospace engineering in February 2002 from Inha University in South Korea. After he was chosen as a 2002 overseas scholarship grantee in the field of aerospace engineering by National Institute for International Education Development in South Korea, he started his Master of science in August 2002, obtained it in August 2004 and he kept pursuing his Ph. D., completed it in December 2006, both in School of Aerospace Engineering from Georgia Institute of Technology.